Thesis on

Fine-Scale Magnetic Features in the Solar Atmosphere

Submitted by

Lakshmi Pradeep Chitta

Thesis Supervisor

Prof. R. Kariyappa

Indian Institute of Astrophysics

Bangalore

Registered for Ph.D. Degree in the

Department of Physics, Pondicherry University

Puducherry

June 2014

Declaration

I hereby declare that the material presented in this thesis, submitted to the Department of Physics, Pondicherry University, for the award of Ph.D. degree, is the result of investigations carried out by me, at Indian Institute of Astrophysics, Bangalore under the supervision of Prof. R. Kariyappa. The results reported in this thesis are new, and original, to the best of my knowledge, and have not been submitted in whole or part for a degree in any University. Whenever the work described is based on the findings of other investigators, due acknowledgment has been given. Any unintentional omission is sincerely regretted.

Lakshmi Pradeep Chitta
(Ph.D. candidate)
Solar Physics Group
Indian Institute of Astrophysics
Bangalore - 560 034
June 2014

Certificate

This is to certify that the work embodied in this thesis entitled “Fine-Scale Magnetic Features in the Solar Atmosphere”, has been carried out by Mr. Lakshmi Pradeep Chitta, under my supervision and the same has not been submitted in whole or part for Degree, Diploma, Associateship Fellowship or other similar title to any University.

Prof. R. Kariyappa
(Thesis Supervisor)
Solar Physics Group
Indian Institute of Astrophysics
Bangalore - 560 034
June 2014

ॐ पूर्णमदः पूर्णमिदं पूर्णात्पूर्णमुदच्यते
पूर्णस्य पूर्णमादाय पूर्णमेवावशिष्यते॥
ॐ शान्तिः शान्तिः शान्तिः॥

To my family and teachers

Acknowledgments

It is really a pleasant–unworldly feeling to have come to this stage of writing about those, whose undivided support and encouragement made me realize this thesis work smoothly. I must admit that their role over the past five years is invaluable and a simple *thanks* cannot match the gratitude I have felt. This note here is merely a way of remembering them in the final phases of my Ph.D. journey.

The journey began in the year 2009 when I joined Ph.D. program at Indian Institute of Astrophysics (IIA). Prof. R. Kariyappa kindly agreed to guide me through the problems on the quiet Sun magnetic field, a body of work, I was fascinated to build that time. Besides being a great mentor, he positively influenced my research career thereafter, by showing the right path and allowing me to traverse it. He showed faith in me and encouraged me to be independent from the beginning. His openness welcomed me to discuss anything with ease. For all these and many more, I am grateful to him.

I thank the Directors, IIA, the Dean, and the Board of Graduate studies, IIA, for giving me an opportunity to pursue my Ph.D. at IIA. I sincerely acknowledge their timely help in kindly forwarding all the necessary documents to Pondicherry University during registration, synopsis and thesis submission. I sincerely thank my Doctoral Committee members, Profs. S. P. Bagare, R. Ramesh, and N. Satyanarayana for their valuable suggestions and comments on the half-yearly reports, and monitoring the progress of my thesis work.

During my Ph.D. I have had the opportunity to interact with some of the eminent solar physicists. I am grateful to Dr. Craig DeForest, whom I met in 2008 at IIA. His lively discussions encouraged me to broaden my understanding in solar physics. I also thank him for giving me an opportunity to visit Southwest Research Institute, Boulder, during August 2010. The discussions I had with Prof. Stuart M. Jefferies have been very insightful. I am indebted to Prof. Siraj Hasan, past Director, IIA, for many fruitful discussions and suggestions related to my thesis work.

I am grateful to Prof. Arnold Hanslmeier, University of Graz, for kindly giving me an opportunity to visit their institute under the Indo-Austria joint research project. I thank Dr. Dominik Utz for many scientific discussions and friendly conversations. Funding from the Indo-Austria exchange program (INT/AUA/BMWF/P-11/2011) is acknowledged.

Thanks are due to Drs. Han Uitenbroek and Alexandra Tritschler for giving me an opportunity to conduct solar observations at the Dunn Solar Telescope (DST), National Solar Observatory, Sacramento Peak. I sincerely thank the observing staff at the DST for providing valuable information and guidance in planning and organizing the observational runs. I sincerely acknowledge the financial support provided by the Indo-US Science and Technology Forum under the Indo-US Visitation Program in Physics for my visit to the DST.

The time I spent as a Predoctoral fellow at the Harvard-Smithsonian Center for Astrophysics (CfA) under the guidance of Drs. Adriaan van Ballegooijen, and Edward DeLuca had a profound impact on my perception of scientific research. They shaped my thinking abilities to conduct forefront research in solar physics. I am honored that I could be a part of the High Energy Astrophysics Division during my stay at CfA. I thank Drs. Leon Golub, Vinay Kashyap, Steve Saar, Mark Weber, and other members of the Division for many fruitful discussions. I thank Ms. Christine Crowley, Ms. Donna Wyatt, and the administrative staff of the Division for providing me with a workplace and necessary facilities, and for looking after the paper work during my stay at CfA. Funding by NASA contract NNM07AB07C is sincerely acknowledged. I thank Dr. Adriaan van Ballegooijen, and his wife Chris for their kind hospitality during my stay at their house.

I thank my Supervisor, the Chairman BGS, the Dean, and the Directors, IIA, for permitting and approving my national and international professional visits for conferences, meetings, and collaborations.

My time as a Ph.D. student has been possible due to the support from various departments at IIA. I thank administrative staff at IIA for their help at various stages in my Ph.D. I would like to thank Dr. Baba Varghese, Data Center, and Computer Support staff for all their help in computing related needs. I thank the librarian, Dr. Christina Birdie, and the library staff at IIA for their help in acquiring books, journals, and publication related issues. I thank the seminar and colloquium organizers at IIA for inviting scientific talks from all branches of astrophysics. I thank IIA journal-club team for their efforts in maintaining a vibrant science environment. I truly enjoyed the time I spent in IIA auditorium attending various lectures and seminars.

I sincerely thank the Dean of the School of Physical, Chemical and Applied Sciences, Pondicherry University (PU), the Head, Department of Physics, and the administrative staff at PU for their help in processing the Ph.D. registration application, synopsis, and thesis submissions.

I thank my friendly seniors at IIA, Drs. Blesson, Tapan, Nagaraju, Vigeesh, Veeresh, Girjesh, Ramya, Ananta Charan Pradhan, Bharat Kumar, Amit, Chandrashekhar, Krishna Prasad for their support and encouragement over the years. The time I spent with them is always cherished. I would also like to thank all the students of IIA for mak-

ing this journey very pleasurable. Special thanks are due to Bala Sudhakara for being a quiet and sensible roommate. I thank Bhaskara Guest House staff for making my stay comfortable. My friends, Dr. Kushal Mehta, and Ms. Shraddha Mody were very supportive and understanding, and made my stay in Cambridge very memorable. They fueled my habit turned passion of photography by driving to several picturesque landscapes, near and far from Cambridge. Their friendship clearly removed any boredom and spread joy when I was feeling low. I remember and cherish all the nature hikes and walks with them and other friends. I would like to thank all my relatives and friends who stood by me all the times and helped me reach this stage.

I dedicate this thesis to my parents, grandparents, sister, Smitha, and my teachers.

Data Usage

Various data sets used in this thesis are obtained from the space-borne and ground-based observatories. I duly acknowledge the usage of data products from these facilities as mentioned below.

Hinode is a Japanese mission developed and launched by ISAS/JAXA, collaborating with NAOJ as a domestic partner, NASA and STFC (UK) as international partners. Scientific operation of the Hinode mission is conducted by the Hinode science team organized at ISAS/JAXA. This team mainly consists of scientists from institutes in the partner countries. Support for the post-launch operation is provided by JAXA and NAOJ (Japan), STFC (U.K.), NASA (U.S.A.), ESA, and NSC (Norway).

I thank NASA's ***Solar Dynamics Observatory*** (***SDO***) and the Atmospheric Imaging Assembly (AIA), EUV Variability Experiment (EVE), and Helioseismic and Magnetic Imager (HMI) science teams for making high quality data available to the community.

Solar and Heliospheric Observatory (***SOHO***) is a project of international cooperation between ESA and NASA.

The **Swedish 1-m Solar Telescope** is operated on the island of La Palma by the Institute for Solar Physics of Stockholm University in the Spanish Observatorio del Roque de los Muchachos of the Instituto de Astrofísica de Canarias.

The German contribution to **Sunrise** is funded by the Bundesministerium für Wirtschaft und Technologie through Deutsches Zentrum für Luft- und Raumfahrt e.V. (DLR), Grant No. 50 OU 0401, and by the Innovationsfond of the President of the Max Planck Society (MPG). The Spanish contribution has been funded by the Spanish MICINN under projects ESP2006-13030-C06 and AYA2009-14105-C06 (including European FEDER funds). The HAO contribution was partly funded through NASA grant number NNX08AH38G.

Contents

List of Publications

Publications:

- *Observations of the Interaction of Acoustic Waves and Small-scale Magnetic Fields in a Quiet Sun,* **Chitta, L. P**., Jain, R., Kariyappa, R., Jefferies, S. M., 2012, ApJ, 744, 98 — **Chapter 2**

- *Dynamics of the Solar Magnetic Bright Points Derived from Their Horizontal Motions,* **Chitta, L. P**., van Ballegooijen, A. A., Rouppe van der Voort, L., DeLuca, E. E., Kariyappa, R., 2012, ApJ, 752, 48 — **Chapter 3**

- *Observations and modeling of the emerging EUV loops in the quiet Sun as seen with the Solar Dynamics Observatory,* **Chitta, L. P**., Kariyappa, R., van Ballegooijen, A. A., DeLuca, E. E., Hasan, S. S., Hanslmeier, A., 2013, ApJ, 768, 32 — **Chapter 4**

- *Nonlinear Force-Free Field Modeling of the Solar Magnetic Carpet and Comparison with SDO/*HMI *and Sunrise/*IMaX *Observations*, **Chitta, L. P**., Kariyappa, R., van Ballegooijen, A. A., DeLuca, E. E., Solanki, S. K., 2014, ApJ, 793, 112 — **Chapter 5**

Proceedings

- *Dynamics of the Photospheric Bright Points Observed With SST and Hinode*, **Chitta, L. P**., van Ballegooijen, A., Rouppe van der Voort, L., DeLuca, E., Kariyappa, R., AAS Meeting 220, 206.14

- *Bright Points in G-Band and Ca* II *H Images from Hinode*, **Pradeep, C. L**., Kariyappa, R., ASSP, ISSN 1570-6591, 424

Co-author

- *Segmentation of the Photospheric Magnetic Elements Corresponding to Coronal Features to Understand the EUV and UV Irradiance Variability*, Giono, G., Kariyappa, R., Zender, J. J., **Chitta, L .P**., Kumara, S. T., Damé, L., (in prep)

- *Segmentation of coronal features to understand the solar EUV and UV irradiance variability*, Kumara, S. T., Kariyappa, R., Zender, J. J., Giono, G., Delouille, V., **Chitta, L. P**., Dame, L., Hochedez, J. F., Verbeeck, C., Mampaey, B., Doddamani, V. H., 2014, A&A, 561, A9

- *Preliminary Results on Irradiance Measurements from Lyra and Swap*, Kumara, S. T., Kariyappa, R., Dominique, M., Berghmans, D., Damé, L., Hochedez, J. F., Doddamani, V. H., **Chitta, L. P**., 2012, AdAst, id 623709

ABSTRACT

The surface of the Sun and solar-type stars is permeated by magnetic fields with a variety of spatial and temporal scales. The spatial scales range from sub-arcsec tangled fields that are yet to be observed (inaccessible to the current instruments) to tens and hundreds of megameters large active regions. The time scales have equally broad spectrum ranging from less than a minute (for small-scale activities) to months (large active regions). These magnetic fields and their activity play a dominant role in the solar atmosphere and govern the space weather. Furthermore, understanding the solar magnetism, its generation, and its interactions act as templates to such phenomena in the large scales. It is generally thought that a solar dynamo process at the base of the convective zone is responsible for the generation of active regions in the Sun. There exists a magnetic cycle, with the global field of the Sun, oscillating between a predominantly poloidal to toroidal field with a period of ≈ 11 years.

Rooted in the convective zone below the photosphere, the magnetic field buoyantly rises through the solar atmosphere. The granular motions continually jostle the magnetic field which lead to magnetic stress and magnetic waves. This interplay between the convective motions and magnetic field holds the key to understand the dynamical solar atmosphere, and coronal heating. High spatio-temporal resolution observations of the Sun reveal a facet of the solar magnetism that is highly intermittent and dynamic. This magnetic field extends well beyond the active regions and covers the entire surface of the Sun. Mainly observed at the boundaries of supergranular cells and in the intergranular lanes, these magnetic fields are known to be responsible for the myriad of structures and phenomena that are observed in the solar atmosphere. The typical length scale of this magnetic field, at the photosphere, range from less than a hundred kilometers to a few megameters. With a magnetic flux of $10^{16} - 10^{20}$ Mx, these are seen as thin bright flux tubes and dark pores in the intensity images.

In this dissertation I study the dynamics of magnetic field, particularly, in the quiet Sun, from photosphere to corona. This work can be broadly divided into two parts. (i) Studying the dynamics of magnetic field at the photosphere. This aspect deals with the interactions between convective motions and magnetic field using high resolution observations: (a) acoustic waves and magnetic field interactions, (b) horizontal motions and dynamics of the solar magnetic bright points. (ii) Magnetic coupling and the heating

of solar atmosphere. Topics of flux emergence and magnetic carpet are explored in this part: (a) hydrodynamic modeling of the coronal response to ephemeral regions in terms of temperature fluctuations and differential emission measure are studied in detail, (b) using the time sequence of high resolution line-of-sight (LOS) magnetograms as lower boundary conditions, three-dimensional (3D) magnetic modeling is performed to understand the role of the magnetic carpet in the heating of solar corona.

Chapter 1

INTRODUCTION

1.1 SUN* – A HISTORICAL OVERVIEW

Of all the billions of stars in our Galaxy (Milky Way) we owe our existence to a mere and an insignificant star orbiting the Galactic center at ≈27000 lightyears—but which possess all the necessary and favorable conditions to support the life on a planet called the Earth. For its power and strength, the Sun held an important role in the ancient mythologies of many cultures across the world. To date, the mankind intricately depends on the Sun. This fiery gas ball in the sky has drawn the attraction of man for many centuries now.

The oldest recorded observation of solar eclipse dates back to 1223 BC[2]. Nearly after 2300 years, John of Worcester, an English monk, made the first drawing of the dark features on the Sun known as the sunspots in the year 1128. His translated notes on the drawing reads

> `...from morning to evening, appeared something like two black circles within the disk of the Sun, the one in the upper part being bigger, the other in the lower part smaller. As shown on the drawing...`

In the year 1543, Nicholas Copernicus, challenged Ptolemy's long-standing notions of planetary astronomy by proposing a new heliocentric model of the solar system. A systematic study of the Sun and solar features, however, started after the invention of the telescope in the 17th century. Galileo Galilei was among the first to document and record the solar features known as sunspots using a telescope, and confirming their solar origin.

*(255°.781,0°.317) are the Hourangle and Declination of the Sun as viewed from Earth (12° 58′ N, 77° 34′ E) at 12:00 on 21 March 2014.

[2] `http://www.hao.ucar.edu/education/TimelineA.php`, and references therein

The next big breakthrough in the solar observations – particularly for sunspots – was witnessed in the year 1843. Samuel Heinrich Schwabe, the German amateur astronomer, discovered a periodic increase and decrease in the sunspot number (Schwabe, 1844). Henceforth the studies of the *sunspot cycle* have begun. Almost 16 years later, Carrington (1859) recorded a spectacular event on the Sun, that was never observed by him before. He explained in his paper

> While engaged in the forenoon of Thursday, Sept, 1 [1859], in taking my customary observation of the forms and positions of the solar spots, an appearance was witnessed which I believe to be exceedingly rare... My first impression was that by some chance a ray of light had penetrated a hole in the screen attached to the object-glass, by which the general image is thrown into shade, for the brilliancy was fully equal to that of direct sunlight; but, by at once interrupting the current observation, and causing the image to move by turning the R.A. handle, I saw I was an unprepared witness of a very different affair.

Reason and source for the already known sunspot cycle, and the events such as the one recorded by Richard C. Carrington were to be understood in the twentieth century. George E. Hale invented spectroheliograph to take monochromatic observations of the Sun. In his seminal work, Hale (1908) described

> While our investigations have thus furnished a plausible explanation of some of the characteristic phenomena of sun-spot spectra, the widening of lines and the presence of doublets are among the remaining peculiarities that demanded consideration. As we have seen, however, these very peculiarities are precisely what would be expected if a magnetic field were present.

This was the first direct evidence for the existence of the extra-terrestrial magnetic field. Subsequently Hale et al. (1919) had discovered many general properties of sunspots. The latter part of the twentieth century saw many developments in both observational and theoretical aspects of the Sun and its magnetic field.

A remarkable discovery awaited another twenty years when Grotian (1939), Edlén (1942) identified strong emission lines of Fe superimposed on the continuum spectrum

Table 1.1: Coronal emission lines identified by Edlén (1942) (also see Billings, 1966; Stix, 2004). χ is the ionization potential of the preceding ion.

	λ [Å]	Ion	Transition	χ [eV]
"Green line"	5302.9	Fe XIV	$3s^2\ 3p\ ^2P_{3/2} - {}^2P_{1/2}$	355
"Yellow line"	5694.5	Ca XV	$2s^2\ 2p^2\ ^3P_1 - {}^3P_0$	820
"Red line"	6374.5	Fe X	$3s^2\ 3p^5\ ^2P_{1/2} - {}^2P_{3/2}$	235

of solar corona. Table 1.1 (adapted from Stix, 2004) shows the coronal emission lines identified by Edlén (1942). These observations established that the corona is hotter than the photosphere and its average temperature is at least two orders of magnitude more than that of the photosphere.

To explain the existence of 1–2 million-degree kelvin corona, several mechanisms were proposed. In his famous work, Alfvén (1947) put forward the idea of magneto hydrodynamic (MHD) waves as sources for coronal heating. Biermann (1948) and Schwarzschild (1948) suggested that the mechanical energy carried outwards by the acoustic waves (which are generated by convective motions in the photosphere) can maintain the high temperature of the corona. In the introduction to his paper, Schwarzschild (1948) wrote

> Until recently the main problem of the chromosphere and the corona was the question of their support... Recently, however, it was found that the temperature of the chromosphere is of the order of 35,000 degree [kelvin] and that of the corona of the order of 1,00,000 degree [kelvin]... Now, therefore, the main problem of the chromosphere and the corona (here considered as a unit and called ''corona'') has become the question of how the high temperature of the corona is maintained.

Until then the observations of the Sun were obtained from the ground-based facilities at moderate spatial and temporal resolution. However, solar studies took a giant leap forward with the advent of spaceborne observatories in the early 1960s and 70s. The early X-ray observations of the Sun produced by the *Skylab* revealed a highly structured corona. Bright regions, and extended and dark coronal holes were observed (Figure 1.1). Reidy et al. (1968) suggested a magnetic confinement of the X-ray emitting plasma. Later, Vaiana et al. (1973) conducted a morphological analysis of the X-ray photographs. They identified six distinct types of quiescent coronal structures (active regions, active region interconnections, large-scale quiet coronal structures, coronal holes, bright points, and the coronal structures enclosing filament cavities).

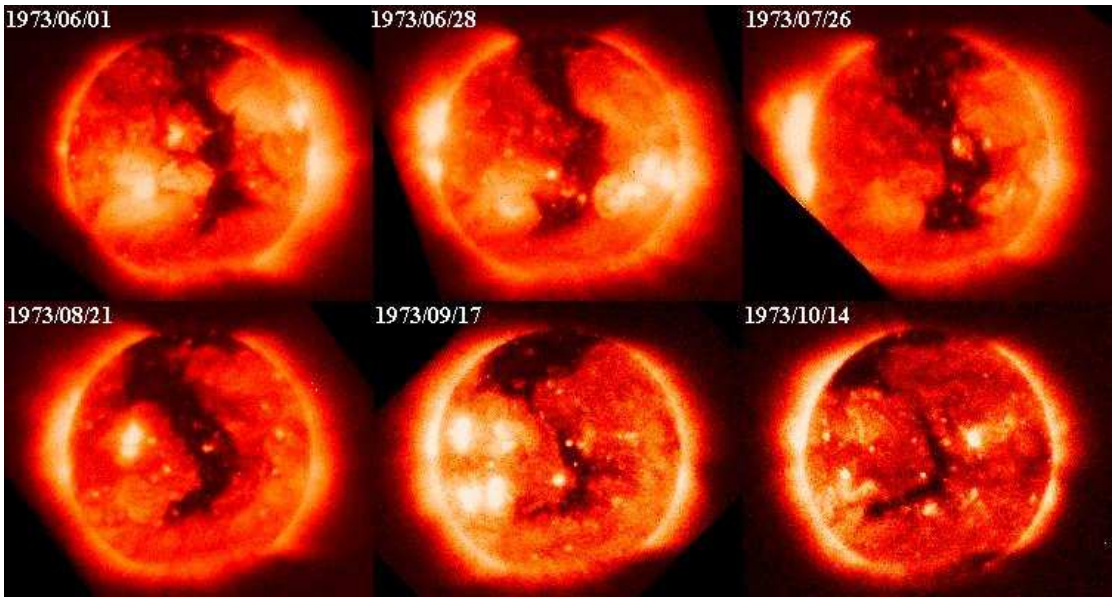

Figure 1.1: Solar images produced by *Skylab* in X-ray wavelengths in the range 6–49 Å. Image courtesy `http://solarscience.msfc.nasa.gov/Skylab.shtml`.

Understanding of the Sun, and its magnetic nature has improved drastically over the last few decades. With the availability of high quality observations from both ground-based and spaceborne facilities, we can now probe the Sun at scales smaller than 100 km. In this Section, I presented a very quick historical overview of some of the important discoveries related to the Sun that are directly relevant to the research work compiled in this thesis. This overview has covered topics related to the solar observations that spanned over a few millennia, and I have skipped many other great advances in the study of solar physics. As a concluding remark to this overview, and to illustrate the need for studying the Sun, I highlight a news article[3] that appeared in Science*Daily* on February 18, 2011, titled, *"Solar Flare: Space Weather Disrupts Communications, Threatens Other Technologies"*. In that article, Professor Daniel Baker said, "`Human dependence on technology makes society more susceptible to the effects of space weather`" — a profound statement emphasizing the place of our planet Earth, its life, and the *technology*, in the realms of the Sun. A century ago, humans would have considered the Sun as a supporter of life on the Earth. But with the increasing human dependence on technological advancements over the past few decades (many of those reaching beyond Earth), the role of the Sun —*regulator of space weather*—is much more than *just* a supporter of life. In the next Section, I briefly introduce the topic of solar magnetic field with an emphasis on the magnetic field at small-scales, which forms the basis for the rest of the thesis.

[3] `http://www.sciencedaily.com/releases/2011/02/110218142451.htm`

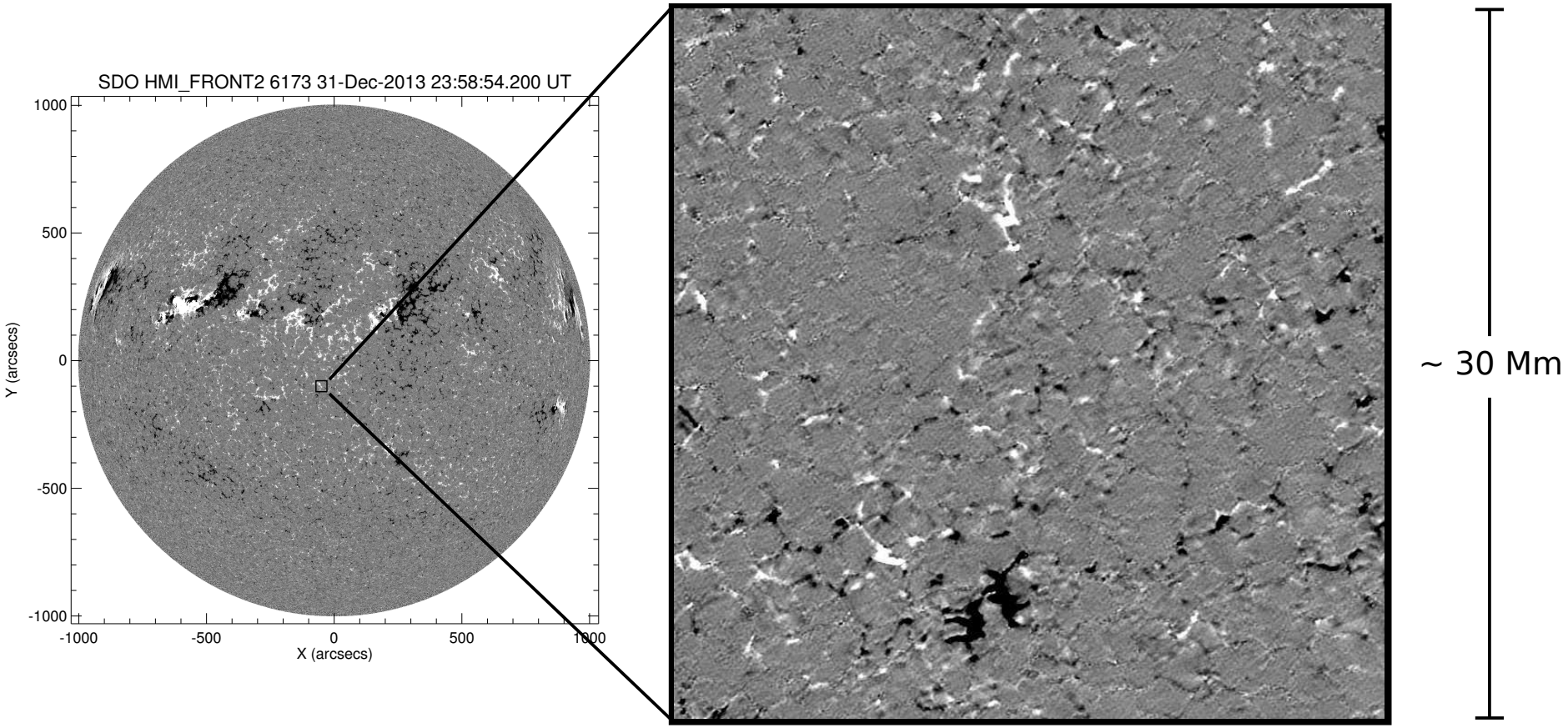

Figure 1.2: Illustration of the solar magnetic field maps. The left panel shows a full-disk magnetogram. The white and black areas are the regions of positive and negative polarities, respectively. The large-scale magnetic structures such as the sunspots and active regions can be seen in the northern hemisphere. The x- and y-axis are in arcsec ($1'' \approx 720$ km on the Sun). A small square region (covering ≈ 30 Mm) near the disk center is shown at much higher resolution (only as a representation, the magnetograms shown in both the left and right panels are obtained from different instruments, and from different days) in the right panel. The discrete and fragmented nature of the network and internetwork magnetic fields are seen.

1.2 SOLAR MAGNETIC FIELD

After a plausible but inconclusive interpretation of the spectrum of sunspots (Hale, 1908), researchers started probing the nature of the solar magnetic field. Hale (1913) attempted to detect the general magnetic field of the Sun. His arguments were based on the hypothesis that the magnetic field on the Sun is due to its axial rotation. He quoted a value of 50 Gauss as the radial field strength at the poles. Cowling (1945) and others have suggested several mechanisms to explain the Sun's magnetic field.

Babcock (1953) developed a new magnetograph to detect weak fields ($\approx$1 G or more) on the Sun (the instrument was installed at the Hale Solar Laboratory). Babcock & Babcock (1955a) and Babcock & Babcock (1955b) analyzed more than 450 magnetograms recorded during the period 1952–1954. They identified a general magnetic field of 1 G, which is limited to heliographic latitudes $> \pm 55°$. They also observed bipolar magnetic regions at lower latitudes. They noted the presence of Ca II plages when the magnetic field intensity is $>$2 G. They observed extended magnetic areas of dominant unipolarity. Some of these unipolar regions had durations of several months. They indicated that these structures were related to 27 day recurrent terrestrial magnetic storms. Leighton (1959) (also see Bumba & Howard, 1965; Sheeley, 1966) described a new method to map the magnetic field on the Sun. He observed 100–200 G extended magnetic regions, which spatially coincide with the Ca II emission in the plages.

At the same time, advances towards understanding of the generation of large-scale solar magnetic fields were underway. Parker (1955b) showed that a horizontal flux tube (from the Sun's toroidal field) buoyantly rises in the electrically conducting atmosphere, forming sunspots at the photosphere. Parker (1955a) (also see Elsasser, 1956) developed general hydromagnetic dynamo models and applied to the case of the Sun. He argued that a dipolar magnetic field can be regenerated from a toroidal field in a rotating sphere of conducting fluid. This bipolar-field$\rightleftharpoons$toroidal-field oscillation was necessary to explain the already (observationally) established solar cycle (Charbonneau, 2010, reviewed the topics of Sun's large-scale magnetic field generation, and solar cycle). It was observed that (Hale et al., 1919; Hale & Nicholson, 1925) the solar magnetic activity (a measure of the number of sunspots on the visible disk of the Sun) has a cyclic behavior. At the start of a new cycle, sunspots first appear within $\pm 30°$of the equator. Due to the solar rotation and other surface flows, in timescales of weeks to months, sunspots progressively move towards the equator (Maunder, 1922). As the cycle advances, sunspots emerge closer to the equator, eventually *disappearing* at the solar minimum. This evolution of the solar cycle gives rise to the famous *butterfly diagram* (c.f. Figure 4 in Maunder, 1922). It is now widely believed that strong toroidal magnetic fields are stored in a layer at the bottom of the convective zone called tachocline layer (see Fan, 2009, and references therein).

Visually, sunspots are extended (covering areas of tens and hundreds of megameters) patches of organized magnetic field on the Sun. They can be identified in both magnetic field maps, and intensity maps of the Sun. In the left panel of Figure 1.2, a line-of-sight (LOS) magnetic map of the Sun is shown (at $0''.5$ pixel^{-1}; $1'' \approx 720$ km on the Sun). The white and black regions are the positive and negative polarity fields, respectively. Sunspots and other large-scale active regions are clearly seen in the northern hemisphere. In the intensity images (e.g. G-band) sunspot has a dark (relative to the surrounding granular brightness) core called umbra. The umbral region is due to a strong radial magnetic field (that inhibits convective motions and thus the energy transfer to the surface). As we go from the center of the umbra to its periphery, we see more fibril like structures due to the inclined field. In Figure 1.3 a representative sunspot observed in G-band (4305 Å) is marked within a long-dashed circle (typically, sunspots extend upto several tens of arcsec).

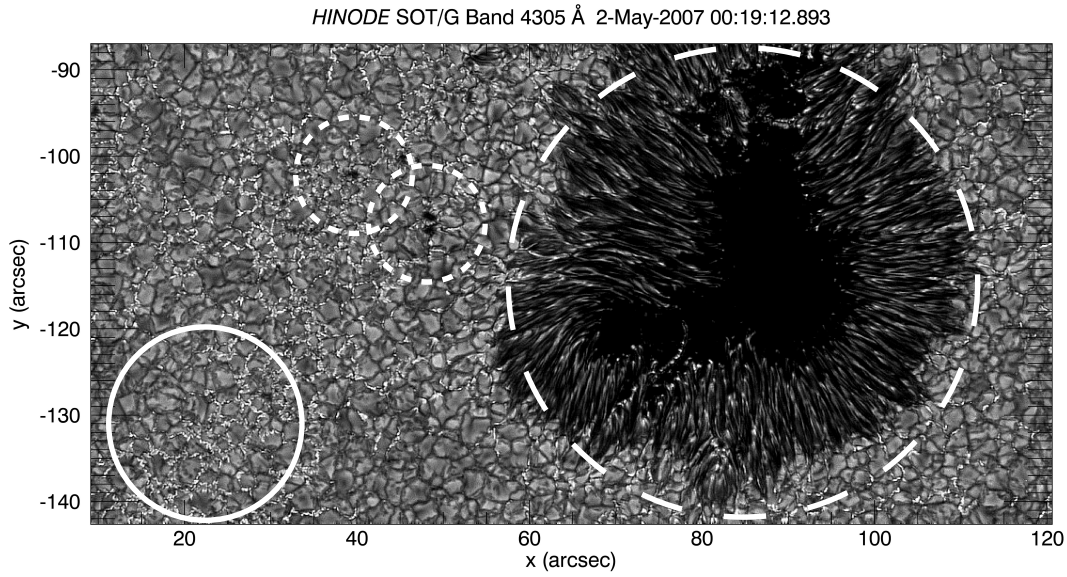

Figure 1.3: G-band (4305 Å) observations of the Sun showing a sunspot (marked in long-dashed circle) and other photospheric features (pores (smaller dashed circles), networks (solid circle), granules).

1.2.1 Solar magnetic field at small-scales

Going back to the magnetic field distribution on the Sun, in the left panel of Figure 1.2 the southern hemisphere is *less active* with a discrete spread of mixed polarity fields (both positive and negative polarities). A small area near the center of the left panel ($\approx$30 Mm^2) is shown at a higher resolution ($0''.16$ pixel^{-1}) in the right panel. Interestingly, even at higher resolution (i.e. at smaller spatial scales), the magnetic field prevails on the Sun. Often referred to as small-scale magnetic field, this subarcsec to arcsec scale

field is randomly distributed on the surface of the Sun near and away from large-scale magnetic structures. Irrespective of the cyclic behavior of large-scale magnetic activity, small-scale fields continue to exist over the entire cycle. However, whether their flux density remains the same is yet to be answered. In Figure 1.3 two smaller dashed circle mark features called *pores* which are intense but compact magnetic structures. The solid circle marks a region of granules (prominent convective signatures of the *non-active* solar photosphere). The intergranular lanes are filled with bright plasma *trapped* in discrete magnetic field (similar to that seen in the right panel of Figure 1.2) forming magnetic network. The availability of magnetic field observations at high sensitivity and rapid cadence allowed researchers to segregate the magnetic features in the *less active* quiet Sun.

Sheeley (1967) observed small-scale magnetic fields with sizes less than 500 km, and field strengths several hundred Gauss devoid of any solar activity. Chapman & Sheeley (1968) used bright photospheric network observed in the spectroheliograms of Fraunhofer lines as a proxy for the magnetic field. Stenflo (1973) (also see Frazier & Stenflo, 1972) used observations of Fe I 5250 and 5247 Å lines to study the structure of photospheric magnetic network. He noted that the network comprises of kilo-Gauss flux tubes with a characteristic size of 100–300 km. By early 1980s, it was well established to consider the bright (facular) points, in the photospheric intensity images, as proxy to the underlying magnetic field (for e.g. Muller, 1983; Muller & Keil, 1983; Stenflo & Harvey, 1985; Muller, 1985; Berger et al., 1995). Some early works on the dynamical behavior of the magnetic bright points include measuring their horizontal motion and associated velocities as they are passively advected by solar granulation. The magnetic elements are buffeted by the granular motions launching MHD waves into the solar atmosphere. The proper motions of bright points are studied in great detail to explain chromospheric and coronal heating (for e.g. van Ballegooijen, 1986; Choudhuri et al., 1993; Muller et al., 1994; Schrijver et al., 1998). The observational and theoretical developments in connection with the small-scale magnetic fields in the solar atmosphere can be traced by extensive reviews on the subject (Solanki, 1993; de Wijn et al., 2009; Wedemeyer-Böhm et al., 2009, and references therein).

The Figure 1.4 is a chart showing various kinds of fields currently known to exist on the Sun (in the quiet regions). A vast literature over the last three decades is devoted to the properties of network and internetwork fields. The internetwork field in the interiors of supergranules (cells) are advected by the convective flows towards the cell boundaries fueling the network fields (for e.g. Orozco Suárez et al., 2012). However, the nature and relation between the other components of the quiet Sun magnetic field are not completely clear.

The difference between the regions filled with the sunspots (and large-scale magnetic activity) and small-scale magnetic field are quite evident in the photosphere (Fig-

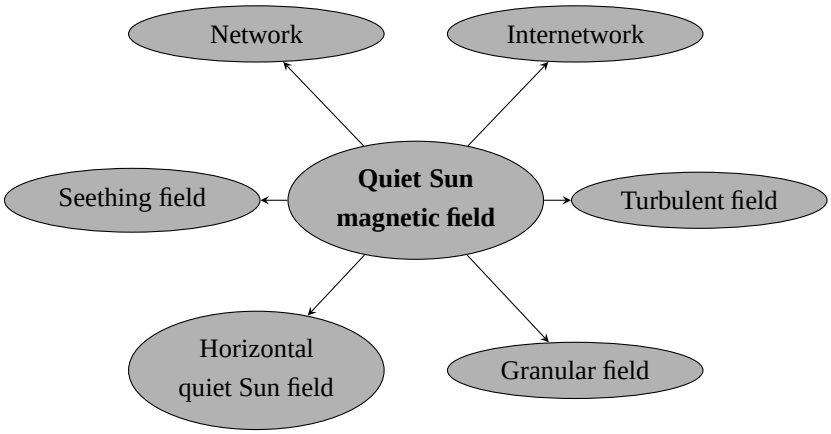

Figure 1.4: Nomenclature of the quiet Sun magnetic field in the literature.

ures 1.2 and 1.3). At this level the plasma motions confine the magnetic field dynamics. As we go higher into the atmosphere, the gas pressure is taken over by the magnetic pressure. Thus we see thin strands of magnetic field lines filled with hot plasma. In Figure 1.5 a sunspot (grey image as the bottom later) and the corresponding atmosphere at various wavelengths are shown. The Extreme-Ultraviolet (EUV) observations (171, 211 and 94 Å) with formation temperatures close to 1 MK or higher show magnetic loops connecting the underlying bipolar region. The electron temperatures above a sunspot exceed more than a few MK. On the other hand, the quiet Sun atmosphere (Figure 1.6) is weak and diffuse with many magnetic loops closing down at lower heights itself. Figures 1.5 and 1.6 are shown for a comparison between the active and quiet solar atmospheres. However, 1D plots of the average temperature in the quiet solar atmosphere reaches 1 MK or more and still requires significant non-thermal energy to balance the radiative and conductive losses (c.f. Figure 3 Withbroe & Noyes, 1977).

To this end, researchers have studied the intensity and velocity oscillations of the network bright points both in photosphere and chromosphere to probe the details of the atmospheric heating (for e.g. Sivaraman & Livingston, 1982; Cram & Dame, 1983; Kalkofen, 1989; Kariyappa et al., 1994; Kariyappa, 1994, and references therein). Magnetic flux tubes transfer the energy to the solar atmosphere by means of these kind of oscillations. Several 2D and 3D numerical simulations and modeling efforts have been attempted to see whether the random footpoint motions of the magnetic field lines in the photosphere carry enough energy to heat the solar chromosphere and corona (for e.g. Hasan & Kalkofen, 1999; Hasan et al., 2005; Hasan & van Ballegooijen, 2008; van Ballegooijen et al., 2011). Kariyappa & Sivaraman (1994) (also Kariyappa & Pap, 1996) studied the variability of chromospheric network over the solar cycle, and its contribution to UV irradiance variability. They found that the chromospheric network elements contribute quite significantly to UV irradiance variability whereas the area of the network elements is anti-correlated with the solar activity.

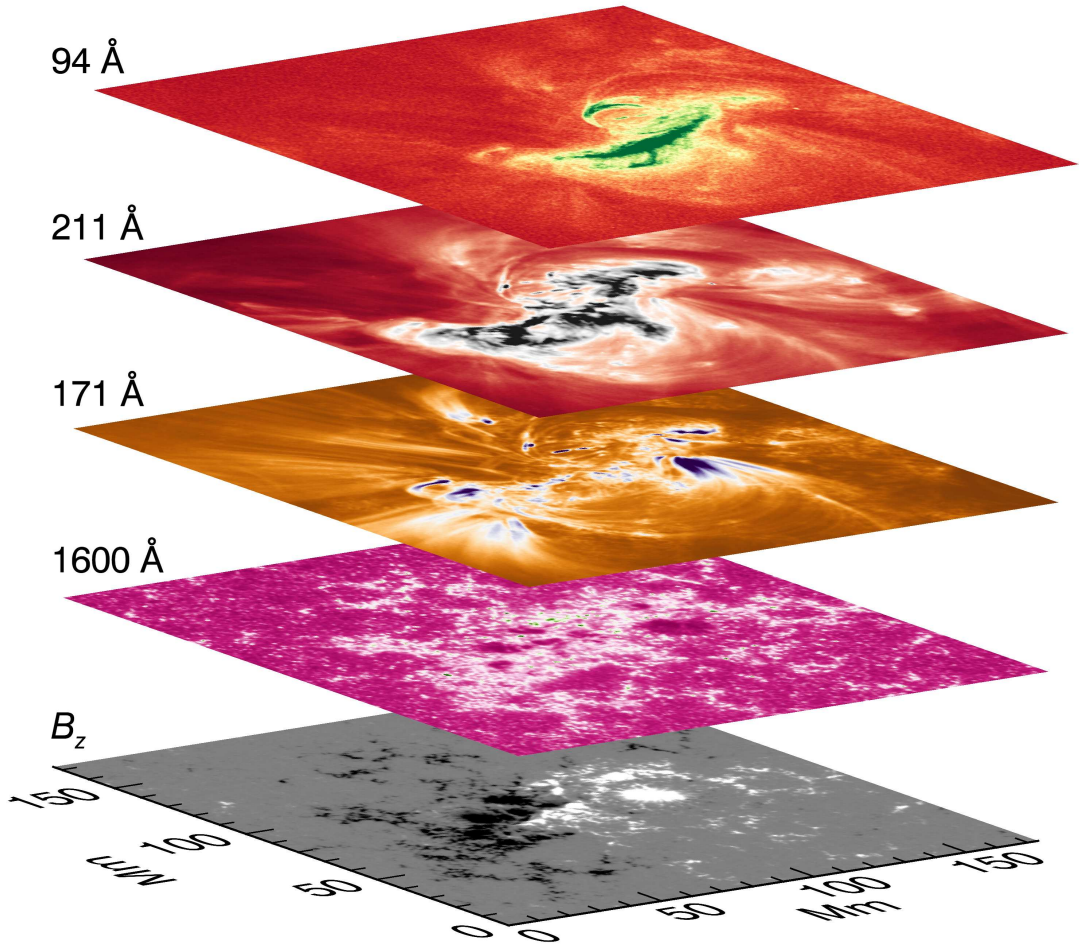

Figure 1.5: Contextual figure showing the atmosphere above a sunspot (plotted as a grey rendering with the photospheric line-of-sight magnetic field). The colored plots show the solar atmosphere at different wavelengths.

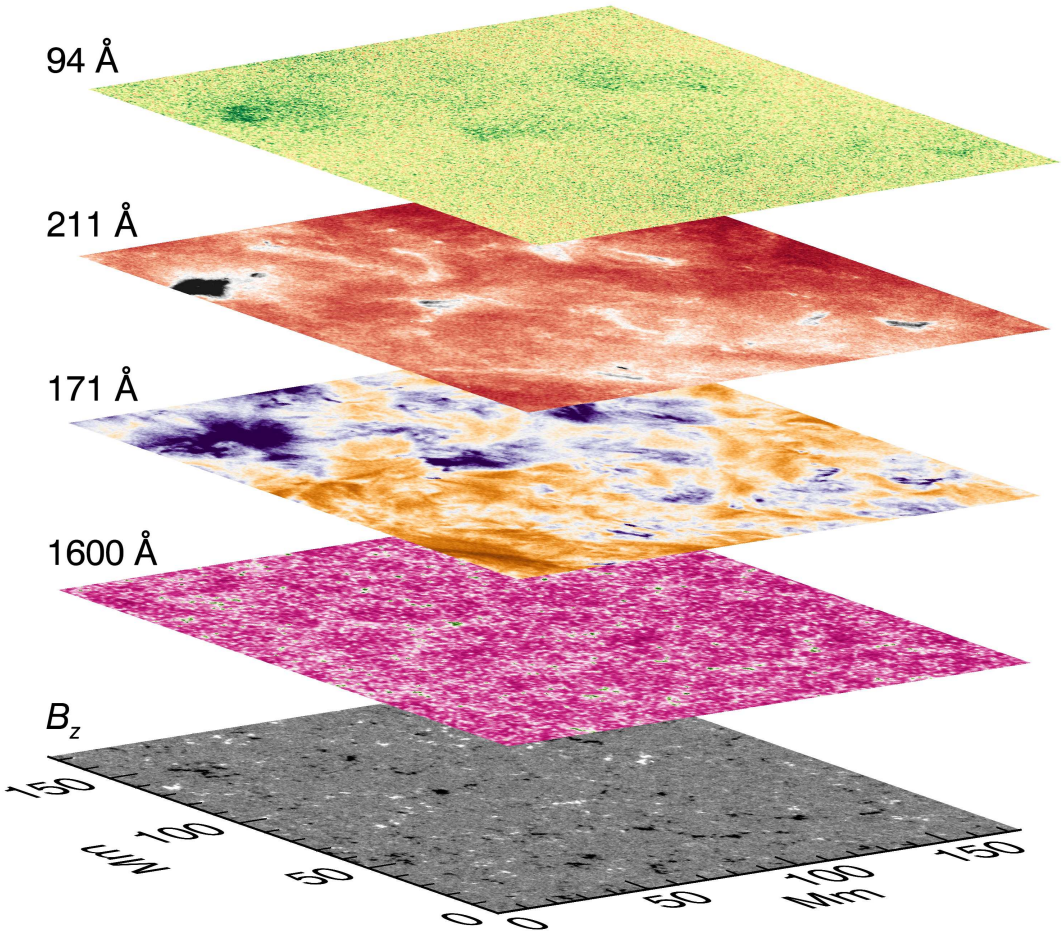

Figure 1.6: Same as Figure 1.5 but for a quiet Sun region.

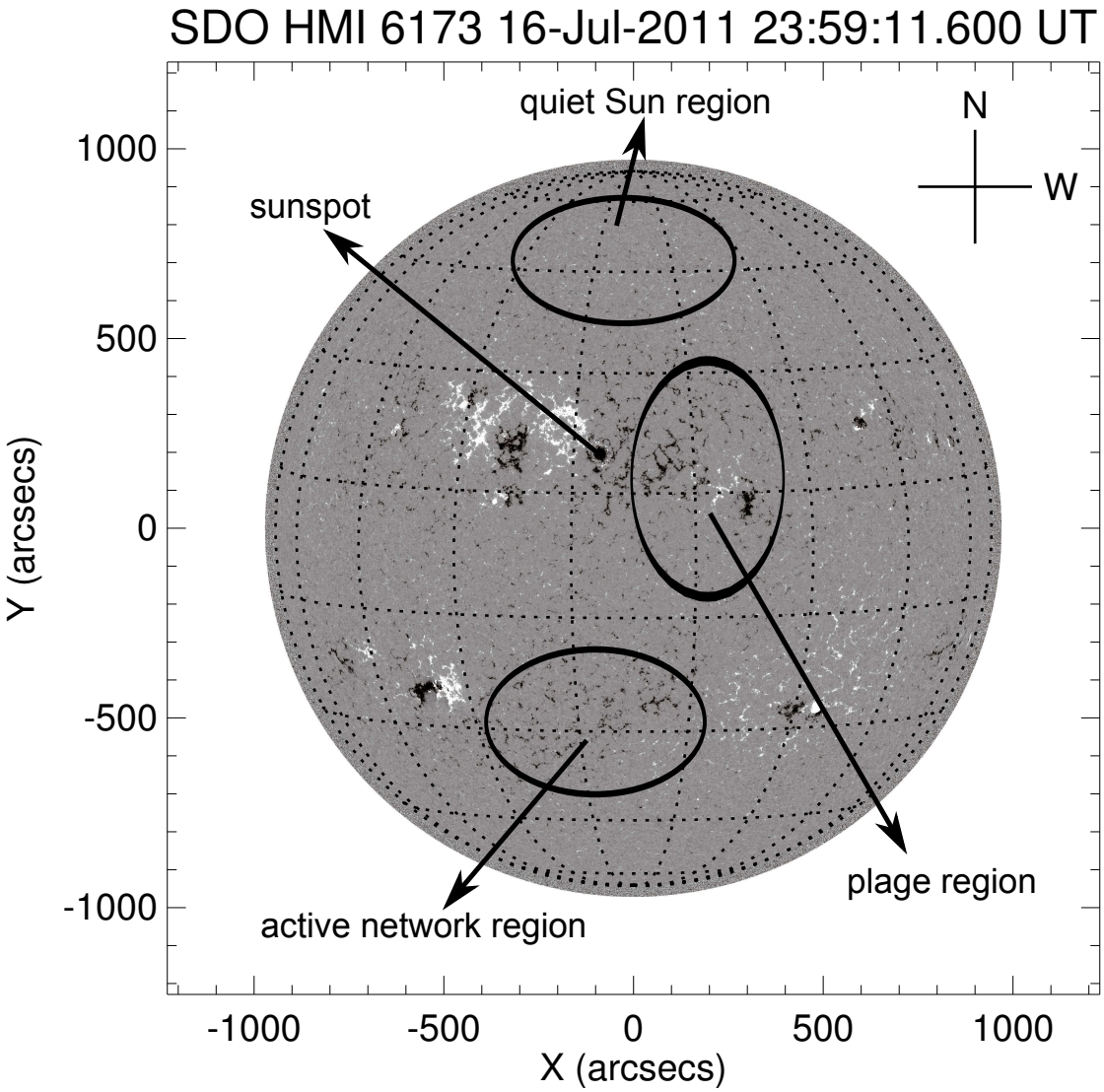

Figure 1.7: Contextual full-disk image showing the line-of-sight magnetic field at the photosphere. Various photospheric magnetic structures are marked.

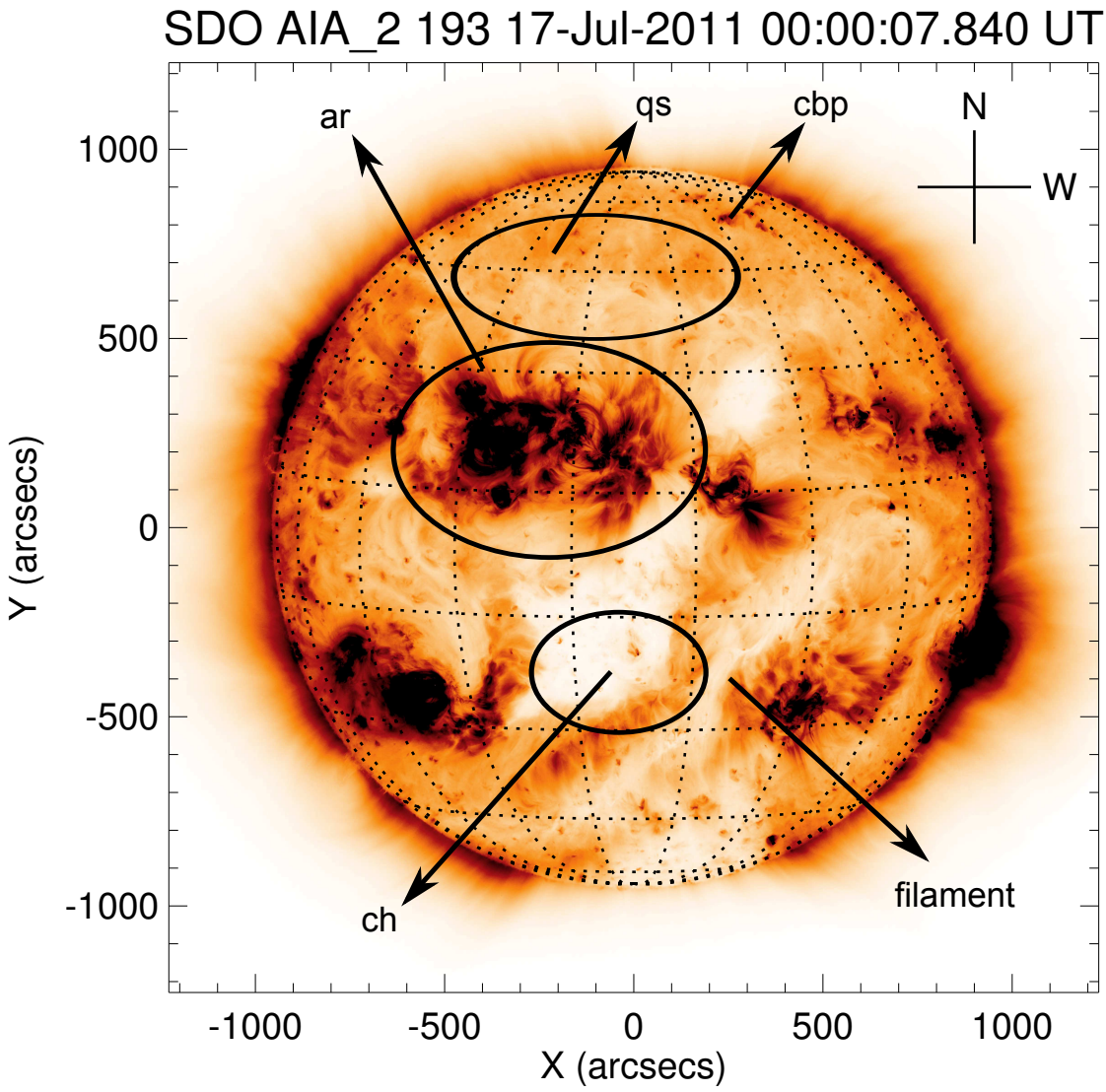

Figure 1.8: Near simultaneous observation of the Solar corona as compared to Figure 1.7. Shown here is a negative image of the solar corona with various structures marked (ar: active region and active region interconnections, qs: quiet Sun, cbp: coronal bright point, filament, ch: coronal hole).

1.3 MOTIVATION

The convective motions in the photosphere passively advect magnetic elements. At the same time, contiguous magnetic elements interact with the acoustic disturbances caused by the convection. This dynamical interplay between the magnetic field and relentless convection is responsible for the structuring of solar atmosphere (Figures 1.7 and 1.8). A schematic of the quiet Sun atmosphere is shown in the Figure 1.9 (courtesy of Wedemeyer-Böhm et al., 2009). Probing the magnetized solar atmosphere at small-scales and high temporal cadence can provide clues about the physics governing the complex atmospheric layers. This forms the motivation for the present thesis work. In the summer of 2008, as a visiting student at Indian Institute of Astrophysics, I was working on the intensity oscillations of G-band and Ca II H bright points, for a two month long project. The results were presented at an international meeting held at IIA. I had the opportunity to interact with many senior solar scientists. My first encounter with the unprecedented *Hinode* data and those interactions inspired me to pursue the work in the field of solar magnetism. Further, the small-scale fields interested me with their curious details and evolution. As a realization of my motivation, this thesis is a study of various properties and dynamics of the small-scale magnetic features in the quiet solar atmosphere—from photosphere to corona.

1.4 THESIS OUTLINE

The main research in this thesis is divided into two parts. The Part-I consists of two chapters. In these chapters, I discuss the results pertaining to the dynamical interactions of convective motions and small-scale magnetic field. In particular, Chapter 2 presents how acoustic waves in the photosphere are influenced by the presence of small-scale magnetic field. In Chapter 3, I discuss the results based on tracking isolated magnetic bright points (that are passively advected by granular flows) and derive important quantities such as the power spectrum of the horizontal motions of the bright points, and photospheric turbulent diffusion. Part-II consists of two chapters geared towards a quantitative understanding of the energy balance in the solar atmosphere over the quiet Sun regions. In Chapter 4, I consider cases of emerging bipoles and study in detail their evolution. Modeling of the EUV emission and possible scenarios explaining the nature of heating in these bipoles are presented. In Chapter 5, I study the role of the solar magnetic carpet evolution in balancing the radiative and conductive losses in the solar corona. The results from a 3D nonlinear force-free magnetic field modeling are discussed in detail. Chapters 2–5 are self consistent with respective introductions, results and discussions. I discuss the major results in this thesis and provide possible future directions in Chapter 6.

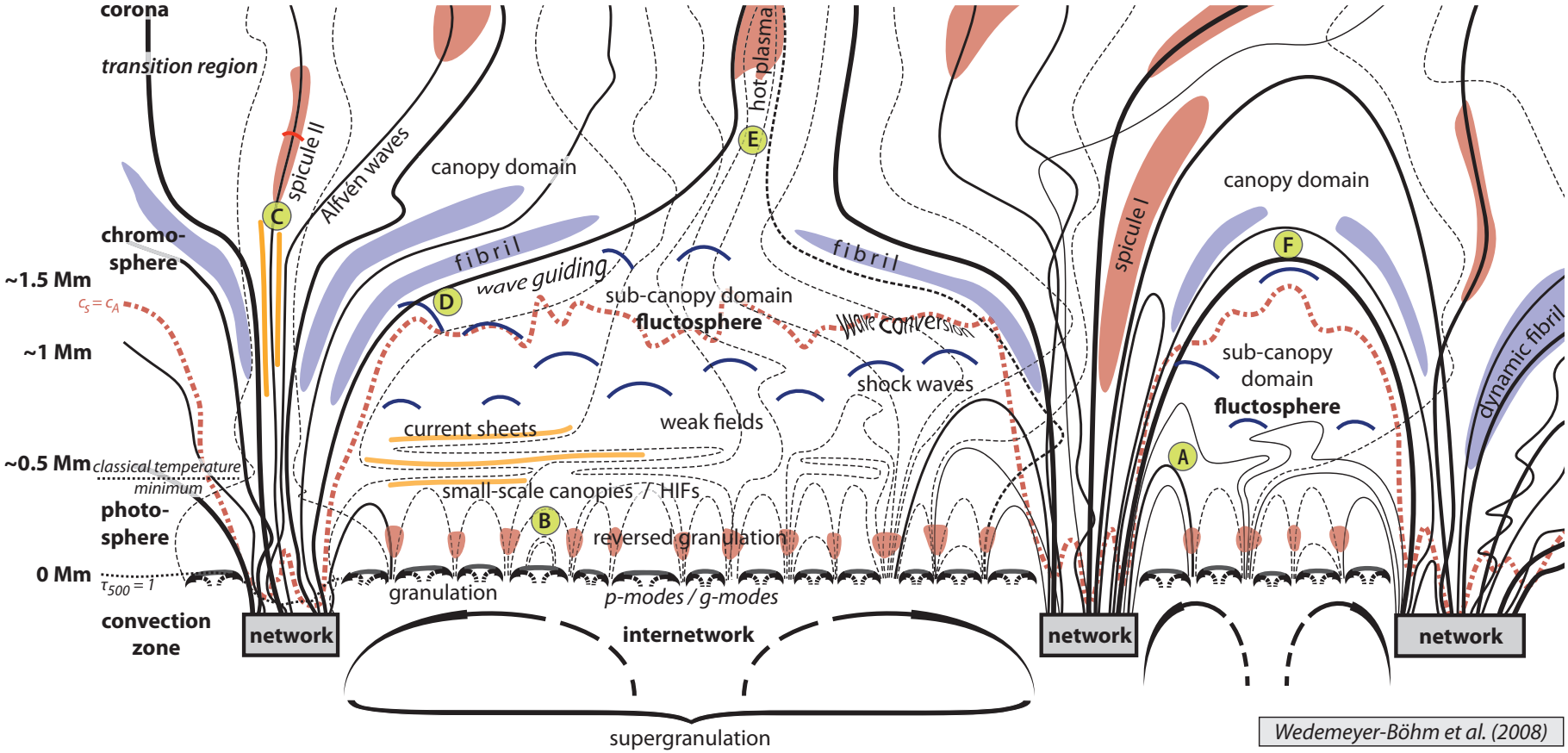

Figure 1.9: A schematic of the lower quiet Solar atmosphere Wedemeyer-Böhm et al. (2009). The network magnetic field extends into the lower atmosphere forming "canopy" like structures (solid lines). The internetwork field in the interiors of supergranular cells is marked with thin dashed lines. Various magnetic domains and processes resulting from the interaction of granular flows and magnetic field are labelled. This schematic illustrates the current understanding of the lower solar atmosphere in a quiet Sun region. I gratefully acknowledge the permission granted by Dr. Sven Wedemeyer-Böhm to use this figure in this thesis.

PART–I

Dynamics in the Photosphere

Chapter 2

INTERACTION OF ACOUSTIC WAVES AND SMALL-SCALE MAGNETIC FIELDS IN A QUIET SUN*

2.1 INTRODUCTION

The magnetic field plays an important role in the evolution of the Sun. Rooted in the convection zone below the solar surface, the magnetic flux tubes extend up into the solar atmosphere and show up as sunspots, plages, networks, small bright points, etc., with very wide scales ranging from a few hundreds of an arcsecond to a subarcsecond. At the solar surface, the magnetic field offers a variety of physical phenomena by directly interacting with waves and oscillations. For example, the magnetic field interacts with the trapped acoustic waves below the acoustic cutoff (p-modes with $\sim$5 minutes period) and the running waves (high-ν waves with periods $<$3 minutes) in different ways (suppression of p-modes and enhancement of high-ν waves over strong magnetic field regions). Concrete results from a wealth of literature over the past two decades show the absorption and scattering of p-modes by sunspots and other active regions. Also, the surface amplitudes of solar oscillations are strongly modified by the presence of the magnetic field (Leighton et al., 1962; Woods & Cram, 1981; Lites et al., 1982; Braun et al., 1987, 1990; Braun & Duvall, 1990; Braun et al., 1992a; Brown et al., 1992; Braun, 1995; Hindman & Brown, 1998; Jain & Haber, 2002; Gizon et al., 2009; Schunker & Braun, 2011). Thomas & Stanchfield (2000) discussed in detail the effects of fine-scale magnetic fields on p-modes and higher frequency acoustic waves in a solar active region. Possible mechanisms have been proposed to explain these kinds of phe-

*The contents of this chapter are published in Chitta et al. (2012a)

nomena (Jain et al., 1996, and references therein). Many interesting questions were also raised by Brown et al. (1992). For example: How is high-frequency power distributed in quiet regions where the large-scale magnetic field is weak? What is the relationship between the excess high-frequency emission and the magnetic field? How does the high-frequency excess depend on height in the solar atmosphere?

Thus, earlier works have firmly established the relation between velocity/intensity oscillations and larger magnetic structures in the active regions of the Sun. In our present work, we focus on the opposite end of the spectrum both in terms of the size of magnetic structures and the activity. We also include G-band intensity and Fe I 6173.3 Å velocity data, which sample different heights above the photosphere compared to the data sets used in the earlier studies of this kind. We discuss the influence of the quiet Sun magnetic field on the intensity and velocity oscillations. We consider "quiet Sun" small-scale magnetic fields (SMFs) in both surroundings, with and without any large-scale and strong magnetic activity such as sunspots or plages. This work is important in the context of the prevailing magnetic field in small scales throughout the solar disk.

In the photosphere, the SMFs are manifested as bright regions when observed using the *G*-band filter at a high resolution (Berger & Title, 2001). We use the filtergram (FG) data obtained from the Solar Optical Telescope (SOT) on board *Hinode* (Kosugi et al., 2007; Tsuneta et al., 2008; Suematsu et al., 2008) for the G-band observations. Magnetic field strength for these bright regions seen in the G-band is derived from the quasi-co-temporal observations obtained from the Michelson Doppler Imager (MDI; Scherrer et al., 1995) on board the *Solar and Heliospheric Observatory* (*SOHO*) and *Hinode* SOT/spectropolarimeter (SP). For a detailed analysis of the nature of the velocity field at the sites of SMFs, we combine observations from the *SOHO*/MDI and Helioseismic and Magnetic Imager (HMI; Scherrer et al., 2012) on the *Solar Dynamics Observatory* (*SDO*; Pesnell et al., 2012).

Such a unique combination of observations from different instruments is desired to exclude any spurious outcome. In this chapter, we study the interaction of SMFs with velocity/intensity oscillations at different frequencies and how the intensity and acoustic power varies as a function of magnetic field strength across the solar disk for particular frequency ranges.

The findings and results reported in this chapter are based on the analysis carried out on a number of data sets taken from different days. The Chapter is organized as follows. Section 2.2 deals with the details of various observations used for the analysis. In Section 2.3, we examine the relation between the magnetic-field–velocity oscillations and magnetic-field–intensity oscillations. In Section 2.4, we discuss these results with concluding remarks.

Table 2.1: Details of the Data Sets Used

Instrument	Date and Time of Observation	Duration (hr)	Cadence (minutes)	Pixel Area
G-band	2007-04-13T19:00–21:00 (set 1)	2	0.5	$0''.108 \times 0''.108$
	2007-06-24T17:08–18:13 (set 2)	~ 1	1	$0''.108 \times 0''.108$
Hinode SOT/SP	2007-06-24T17:08–18:13	~ 1	$\cdots$	$\sim 0''.3 \times 0''.32$
	2001-12-21T00:00–05:00	5		
	2004-05-23T15:00–20:00	5		
SOHO/MDI	2007-04-13T19:00–21:00 (set 1)	2	1	$0''.6 \times 0''.6$
	2007-06-24T17:00–19:11 (set 2)	2.2		
	2009-04-18T15:00–20:00	5		
	2010-09-12T00:00–03:00 (type a)			
SDO/HMI	2010-10-17T00:00–03:00 (type a)	3	0.75	$0''.5 \times 0''.5$
	2010-10-30T00:00–03:00 (type a)			
	2010-10-20–21T17:19–22:07 (type b)	28.8	0.75	$0°.04 \times 0°.04$

2.2 DATASETS

We consider different data sets of *G*-band FGs, magnetograms, Dopplerograms, and high-resolution FGs for this analysis. Table 2.1 gives a summary of the data sets used for the analysis. The details of these data sets are as follows.

2.2.1 Disk Center

G-band data from Hinode SOT/FG: Set 1—Time series with a resolution of $0''.108$ pixel^{-1} and a $111'' \times 55''$ field of view (FOV), with a 30 s time cadence obtained near the disk center ($17''.30, -24''.35$), on 2007 April 13 at $19:00-21:00$ UT. Set 2—Time series with a resolution of $0''.108$ pixel^{-1} and a $111'' \times 111''$ FOV, with a 1 minute time cadence obtained near the disk center ($-9''.88, 32''.53$) in a quiet region on 2007 June 24 at $17:08-18:13$ UT. From these G-band data cubes, we extract and use only the regions for which magnetic field information is available. *Magnetograms, Dopplerograms, and high-resolution FGs*: high-resolution observations from *SOHO*/MDI with a resolution of $0''.6$ pixel^{-1} and about a $600'' \times 300''$ FOV with a 1 minute time cadence, obtained quasi-simultaneously with Set 1 of the G-band data. Also, data sets obtained on 2001 December 21, 2004 May 23, 2007 June 24, and 2009 April 18 and co-temporal level-1d Hinode SOT/SP data corresponding to Set 2 of the G-band data are considered for the analysis.

Hinode/SOTs FOV is completely contained within the *SOHO*/MDIs FOV. G-band FGs are processed to level-1 data using standard procedures provided in the *solarsoft* library (Freeland & Handy, 1998). MDI data are processed to level 1.8. *Hinode* SOT/SP inversions were conducted at NCAR under the framework of the Community Spectro-Polarimetric Analysis Center[2]. We invariably mention the longitudinal apparent magnetic flux density (derived from *SOHO*/MDI, *Hinode* SOT/SP, and *SDO*/HMI) as the magnetic field strength in the rest of this chapter.

For this analysis, we have identified a network region from Set 1 and small networks and bright points from Set 2 of the G-band time series. The selected regions show enhanced brightness compared to the surrounding granules. We plot the map of the region of interest from Set 1 (see Figure 2.1). The selected bright feature has a counterpart in the magnetograms, for which the magnetic field strength has a range of values from -457 to 228 G in a 2 hr time-averaged magnetic map obtained from the time series. We also have corresponding Doppler images (Figure 2.2) and high-resolution FGs from MDI.

High-resolution G-band images are resized and aligned to match MDI FGs. A portion corresponding to the G-band FOV is extracted from the velocity, intensity, and

[2] `http://www.csac.hao.ucar.edu/`

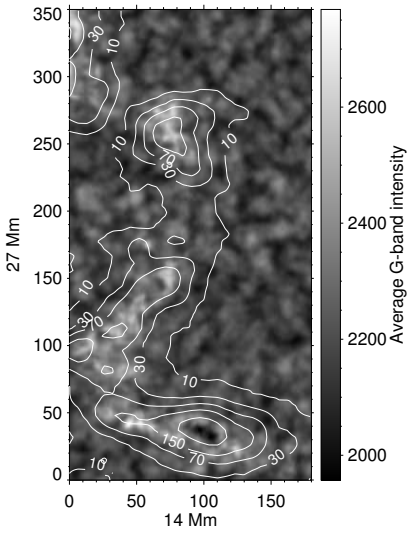

Figure 2.1: Contours for various values of mean magnetic field strength (in Gauss) obtained from *SOHO*/MDI are overplotted on the time averaged G-band (Set 1) intensity map (in Digital Number (DN) units). Note that this map corresponds to the central region (marked within the black rectangle) of Figure 2.2.

magnetic field data sets for the analysis. An average magnetic field map is formed using the extracted magnetograms. The contours of magnetic field strength are shown in Figure 2.1. Note, for the analysis of magnetic field dependence on the velocity oscillatory power, we use a much larger FOV (a sample region is shown in Figure 2.2), keeping the image resolution to $0''.6$ pixel^{-1}, i.e., the original image resolution of MDI. The above mentioned intensity (both G-band and high-resolution FGs) and Doppler velocity data sets are Fourier transformed in time at each pixel to obtain the power spectra of intensity and velocity fluctuations for each pixel.

2.2.2 Center to Limb

Since we are dealing with small-scale features on the Sun, to carry out the longitudinal variation of the magnetic-field–Doppler-velocity relation, we need simultaneous and precise observations of velocity oscillations and magnetic field across the solar disk. *SDO*/HMI is capable of providing high quality rapid and simultaneous full-disk observations with virtually no data gaps. *SDO*/HMI uses the Fe I 6173.3 Å line for both Doppler velocity and line-of-sight (LOS) magnetic field measurements. To avoid any ambiguity, we consider five data sets for which observations are made on September 12 and October 17, 20, 21, and 30 of 2010 using *SDO*/HMI. In the above mentioned observations, there are two data types: (a) Doppler velocity and magnetograms of September 12, October 17, and October 30 and (b) Doppler velocity and magnetograms of October 20 and 21 that are tracked and re-mapped into heliographic coordinates (using Postels

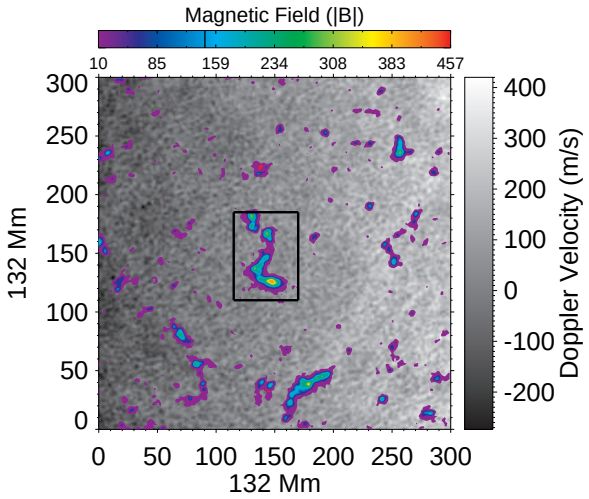

Figure 2.2: Shown in the gray scale is a sample of the 2 hr time-averaged Doppler image obtained from *SOHO*/MDI on 2007 April 13. Colored contours indicate the location of the mean magnetic field (absolute value) obtained from MDI magnetograms. Note that the central region marked in the black rectangle is the location of G-band (Set 1) observations (see Figure 2.1).

projection) corresponding to Carrington rotation 2102. The image resolution is set to $0''.504$ pixel^{-1} and 0°.04 pixel^{-1} for data types (a) and (b), respectively.

Data type (a) is a set of Doppler velocity and LOS magnetic field observations of a 3 hr duration for each day. Using hg_patch mode[3], we select cuts of $1800'' \times 300'' \times 3$ hr data cubes (read as width×height×time). Since our desire is to study the strength of the interaction from the center to the limb, we make smaller data cubes of $200'' \times 300'' \times 3$ hr from the above-mentioned sets. For representation, in Figure 2.3, we show a map of Doppler velocity from the time series of 2010 October 17. The black rectangles represent three regions of analysis centered at $(-400'', 0'')$, $(0'', 0'')$ and $(400'', 0'')$, respectively, and the overlapping dashed white rectangles are also regions of analysis centered at $(-300'', 0'')$ and $(300'', 0'')$. In total, we extract 17 smaller cubes from each full data cube, and the smaller cubes have an overlap of $100''$ in the x-direction of the image plane as shown in Figure 2.3 with their adjacent regions. Data type (b) is composed of Doppler velocity cubes of 15°× 15°× 28.8 hr observed at five positions on the solar disk, i.e., corresponding to five solar longitudes. For better comparison, we extract two 3 hr duration subsets from each data cube (along with the magnetograms), the *first* set at the beginning and the *second* close to the middle of the observations with a 12 hr time gap between two extracted subsets. Hereafter, we call the $first$ subset $b1$ and the $second$ subset $b2$. We feel that the time gap we consider is long enough compared

[3] `http://jsoc.stanford.edu/ajax/exportdata.html`

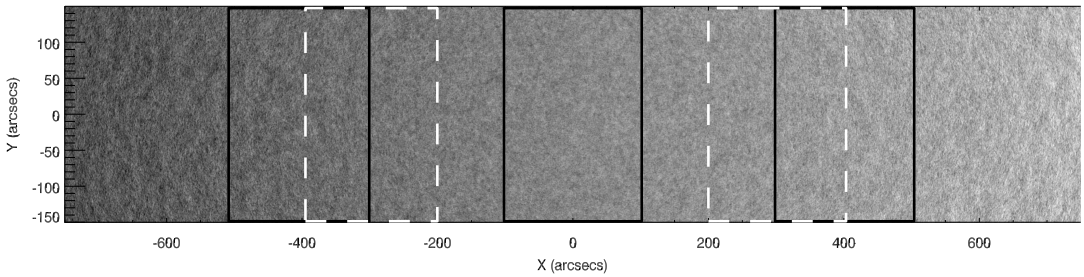

Figure 2.3: Sample image of Doppler velocity taken from data of 2010 October 17 (type (a)). The image is centered at $(0'', 0'')$. For representation, three black rectangles of $200'' \times 300''$ are shown corresponding to three extracted regions used for the analysis, centered at $(-400'', 0'')$, $(0'', 0'')$ and $(400'', 0'')$, respectively. To demonstrate the overlapping, dashed white rectangles are drawn centered at $(-300'', 0'')$ and $(300'', 0'')$ which are also used for the analysis.

to the timescales of rapidly evolving SMFs, which ensures a different morphology and configuration of the magnetic field in the former and latter subsets at any particular longitude.

All the velocity cubes (data types (a) and (b)) are Fourier transformed in time at each spatial point and the acoustic power is determined with a frequency resolution of 93 μHz up to the Nyquist frequency of 11.11 mHz. The resultant cubes are then integrated over the frequency ranges $2.5 - 3.9$ mHz and $5.5 - 7$ mHz to construct p-mode and high-ν power maps, respectively.

2.3 RESULTS

2.3.1 Influence of the Magnetic Field on Velocity Oscillations

Power maps of trapped p-mode and high-ν oscillations are obtained from the power spectra by integrating the power over all frequencies at each pixel within the ν-range $2.5 \leq \nu \leq 3.9$ mHz and $5.5 \leq \nu \leq 7$ mHz, respectively. We plot the velocity power (VP) as a function of magnetic field strength. A gradual decrease in the VP in the frequency band $2.5 \leq \nu \leq 3.9$ mHz is observed with increasing field strength. In the left panel of Figure 2.4, we plot the VP as a function of frequency. An enhancement in the VP is clearly seen for frequencies above 5.5 mHz (dashed line) compared to their profile over weak magnetized regions (solid line), differing from the nature of p-mode behavior. Furthermore, to determine the strength of the interaction of velocity oscillations and magnetic field in the quiet Sun regime, we calculate a ratio from the average p-mode powers in the regions corresponding to $10 < |B| < 40$ G and $|B| > 40$ G. We chose these field strength ranges because we identified that the regions with

$10 < |B| < 40$ G form a boundary surrounding the SMFs whereas the regions with $|B| > 40$ G form the interior regions of these magnetic elements. We find that there is a drop of $\approx 20 - 30\%$ in the p-mode power in the interior regions. This drop in power is consistent from our analysis of many data sets. To compare this ratio with the values over active regions, we calculate the ratio in the case of large magnetic structures, such as plages and sunspots, for other data sets (not shown here) and find that there is more than a $30\% - 40\%$ drop in the p-mode power in such large active regions for high magnetic field strengths.

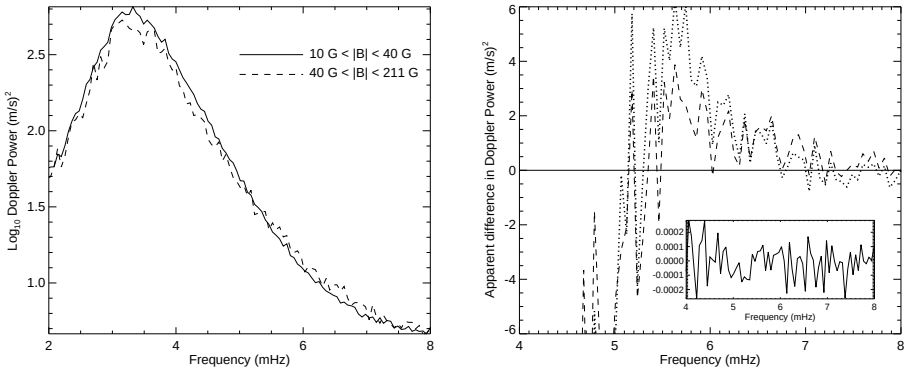

Figure 2.4: Left panel: $\log_{10}$ of the observed Doppler VP observed (for the 2009 April 18 data) for two ranges of magnetic field strengths $10 < |B| < 40$ G (solid line) and $40 < |B| < 211$ G (dashed line). Note that the enhancement is seen in high-ν waves (above 5.5 mHz) in the strong field case whereas the p-modes are suppressed. Right panel: apparent difference in the Doppler VP observed for the original data (dashed line) and modeled noise data (solid line). The inset shows the variations in the solid line (i.e., NP) in the $4 - 8$ mHz band. The dotted line shows the Doppler power increment over strongly magnetized regions in comparison with power over very weakly magnetized ($0 - 5$ G) regions

It is worthwhile to analyze the contribution of random noise (for example, ± 20 m s^{-1} noise per pixel in the *SOHO*/MDI Doppler velocity data; Scherrer et al., 1995) to the power spectrum as a function of frequency. For this, we have generated a random noise data cube of the same dimensions (both in space and time) as that of analyzed Doppler velocity data. A red noise power (NP) spectrum (power decreases with the increase in frequency) has been obtained from the Fourier transformation of noise data in the time domain. The NP integrated over weak and strong magnetic field strengths has been compared with the MDI VP. It is also essential to compare the enhancement seen in high-ν over strong magnetized regions with the power over very weakly magnetized (over $0-5$ G) regions ($P_{0-5\ \mathrm{G}}$). The results are shown in the right panel of Figure 2.4, for which the description of contents is as follows. Solid line: derived from noise data $\rightarrow$ $\mathrm{NP_{strong}}-\mathrm{NP_{weak}}$ (also shown in the inset); dashed line: derived from the MDI signal $\rightarrow$ $\mathrm{VP_{strong}}-\mathrm{VP_{weak}}$; dotted line: derived from the MDI signal $\rightarrow$ $\mathrm{VP_{strong}}-\mathrm{P}_{0-5\ \mathrm{G}}$; strong

and weak in the above description denote the magnetic field strengths. $\mathrm{NP_{strong}} - \mathrm{NP_{weak}}$ is read as $\mathrm{NP_{strong}}$ minus $\mathrm{NP_{weak}}$. These results suggest that a noise of ± 20 m s^{-1} may contribute a negligible amount of power to the original signal. We implemented this comparison using white noise (power is constant as a function of frequency), and we do not see any substantial changes in the result. This confirms that the noise in the pixel counts will not possess a well-defined power profile with respect to the magnetic field. The power increment seen above 5.5 mHz in the strong field regions as compared to that of very weakly magnetized ($0 - 5$ G) regions (dotted line) is consistent with the earlier works on active regions (e.g. Figure 5 in Brown et al., 1992).

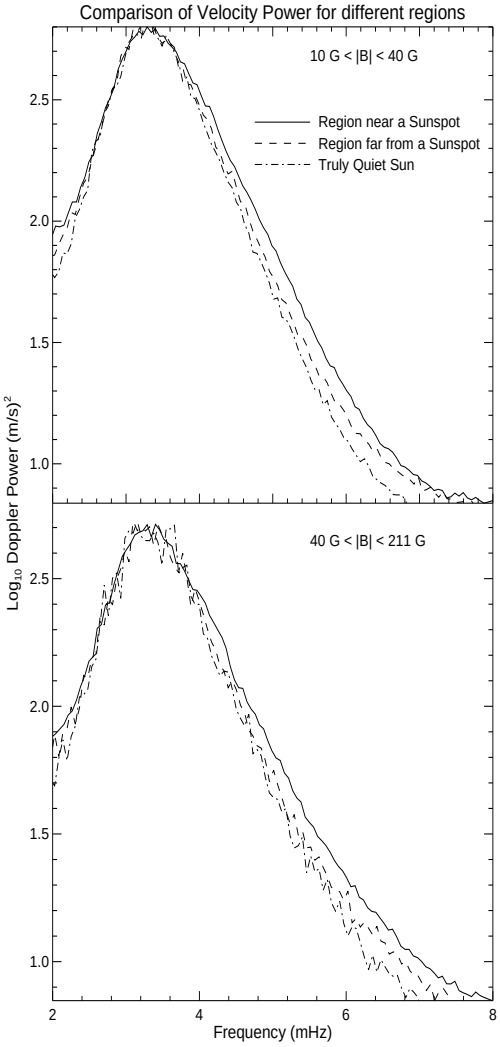

Figure 2.5: Comparison between the Doppler VPs for three different regions with different surroundings. Top panel: VP for magnetic field strengths $10 < |B| < 40$ G in a relatively quiet region close to a sunspot (solid line), far from a sunspot group (dashed line), and in a truly quiet Sun (dash-dot line). Bottom panel: same as the top panel, but for field strength ranging in $40 < |B| < 211$ G. Difference in the three regions is seen in both weak and strong field cases above 4 mHz.

2.3.2 True Quiet Sun

Even the "quiet" regions far away from magnetically active regions consist of SMFs with a mean lifetime of a few minutes. The solar surface is filled with such a ubiquitous, turbulent magnetic field with short lifetimes, which may govern the dynamics of the solar atmosphere. Such a turbulent magnetic field is generated and sustained by a local dynamo phenomenon that is believed to occur at granular scales. For a recent review on different possible generation mechanisms of SMFs, see de Wijn et al. (2009). By investigating the influence of these small-scale fields on observed Doppler velocities, we can in turn start unraveling the influence of the source(s) of these kinds of magnetic fields on the oscillatory behavior at the solar surface. It is therefore interesting to quantify the contribution toward suppression/enhancement of oscillatory power from such quiet Sun regions alone.

One direct way to do this is by quantitatively comparing the results from the regions with different surroundings. This will enable us to see the possible influence (if any) of the surroundings on the region of interest. Thus, we analyze three different regions: (1) a relatively quiet Sun near a big sunspot, (2) a region far from a sunspot group, and (3) a true quiet Sun. We carefully choose the true quiet Sun regions such that there are no large-scale activity and sunspots in the observable part of the solar disk up to at least 10 days before observation. For better and easier comparison, it is useful to keep the spatial dimensions and time span of observations fixed in all three cases. For this, we choose a region of $240'' \times 240'' \times 5$ hr from each data set (2001 December, 2004 May, and 2009 April). These three periods correspond to different phases of solar activity. To compare the oscillatory behavior over similar field strengths, we set the field strength ranges with respect to the quiet Sun magnetic field as discussed earlier. We plot the Doppler VP as a function of frequency for all three cases (Figure 2.5). Top and bottom panels are for weak ($10 < |B| < 40$ G) and strong ($40 < |B| < 211$ G) field ranges, respectively. In both panels, solid, dashed, and dash-dot lines represent 2001, 2004, and 2009 data, respectively. We see that for the same field strength ranges (in both weak and strong field cases), the distinction becomes evident between the three regions above 4 mHz. The VP signal is generally found to be more suppressed in the "true quiet region" compared to the quiet regions nearer or farther away from the sunspots, for both magnetic field ranges. However, the power ratio (strong to weak magnetic field strengths) within the FOV as a function of frequency is found to be the same for all three data sets, suggesting that the relative difference in the Doppler VP between non-magnetized and magnetized regions is independent of the proximity of the small-scale magnetic features to the large magnetic active regions. This similarity in the qualitative behavior of all three data sets would suggest that the same physical mechanism (for power suppression (enhancement) below (above) 5.5 mHz) is at play

regardless of whether the quiet region is closer to an active region or not. However, one of the concerns is that a change in the modulation transfer function of the MDI instrument over time could also lead to a slight change in the magnitude of the observed Doppler velocities in the surroundings, so some caution is necessary when interpreting these results.

2.3.3 Center-to-Limb Variation (CLV) of the Interaction

The nature of the p-mode power enhancement (sometimes referred to as the "acoustic halos") above 5 mHz is not very clear to date. Braun et al. (1992b) and Brown et al. (1992) interpret this phenomenon describing high-ν halos as the regions with increased acoustic emissivity or scattering. Hindman & Brown (1998) suggested that the magnetic field, which is primarily vertical at the photosphere, ducts the acoustic oscillations into field-aligned motions and, therefore, observations at the disk center would register an increased LOS velocity signal.

One would ideally expect to examine the same magnetic feature and its interaction with its surroundings at different positions as it traverses across the solar disk, but since we are limited by the rapid evolution of small-scale magnetic features and these features reconfigure very fast (having a smaller lifetime compared to the solar rotation), the results may not be actually driven by the configuration of the field alone but may depend on the position. We try to qualitatively show that this assumption is indeed not far from the true behavior of these features. To this end, we sort the p-mode and high-ν VP maps with the magnetic field. Now, we consider two ranges of magnetic fields: $10 < |B| < 40$ G (weak field) and $|B| > 40$ G (strong field), then take the average powers within the respective magnetized regions and take the ratio of the average VP in the strong field to the weak field (for both frequency bands). In Figure 2.6, we show the ratios calculated in the manner described above and plot for various positions across the solar disk. The left panel of Figure 2.6 shows the results obtained from data type (a),[4] where the open symbols denote the p-mode ratio and solid symbols are for the high-ν power, and the x-axis is the distance measured in arcseconds on either side of the disk center. While the ratio of p-mode power is constant around a value of 0.8 (this value is consistent with the disk center results obtained from *SOHO*/MDI) across the solar disk, the high-ν power ratio decreases from center to limb. The right panel of Figure 2.6 is the same as the left panel but plotted for the power maps of data type (b); the x-axis denotes the central meridian (Stonyhurst units) of the tracked region at the mid-time of tracking. Power ratios corresponding to $+70°$ have some deviation from the regular trend; this is largely due to the fact that the limbward data are affected in the course of

[4]Plot is for the mean value of ratios derived from the three sets and the error bars showing 1σ deviation from the mean.

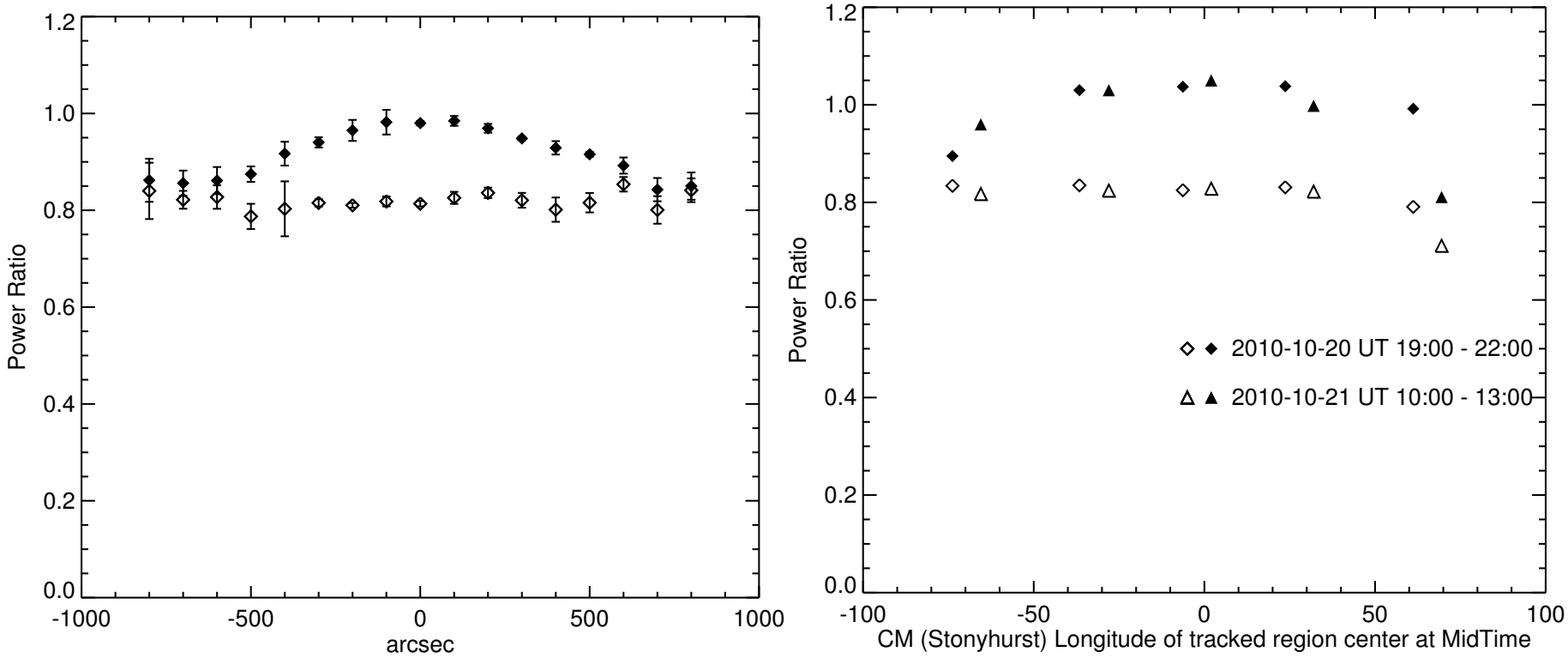

Figure 2.6: $P_{\rm I}$ is the average VP over regions with a weak magnetic field ($10 < |B| < 40$ G) and $P_{\rm II}$ is the average VP over regions with a strong magnetic field ($|B| > 40$ G). We plot the ratio $P_{\rm II}/P_{\rm I}$ for both p-modes (open symbols) and high-ν (solid symbols) oscillations across the solar disk for data type (a) (left panel, tracked data sets) and data type (b) (right panel, data sets tracked and remapped using Postel projections).

tracking and remapping, as the disk moves away from the line-of-sight.

We must admit that selecting the field ranges arbitrarily could be misleading and hence a further scrutiny is required. A careful analysis of the VP and the connection with the magnetic field gives us more insight into the connection between the two quantities, which is not obvious from Figure 2.6. We calculate the average power of the regions over the magnetic field ranges (b): $0-10, 10-20, 20-40, 40-60, >60$ G in both power maps at each longitude position of data type (b) and normalize it with the maximum average power at that position:

$$r = \frac{\langle p(\nu, L_p, b_i)\rangle}{\max(\langle p(\nu, L_p, b_i)\rangle)}; \quad i = 1, 2, \tag{2.1}$$

where $\langle p(\nu, L_p, b_i)\rangle$ represents the average power at a given L_p (central meridian of the tracked region at the mid-time of tracking) in the frequency band ν (p-mode or high-ν) and r is the normalized power ratio. Here, $i = 1$ corresponds to the data cubes taken from the beginning of data type (b), while $i = 2$ is for data sets taken from the mid-time of tracking data type (b).

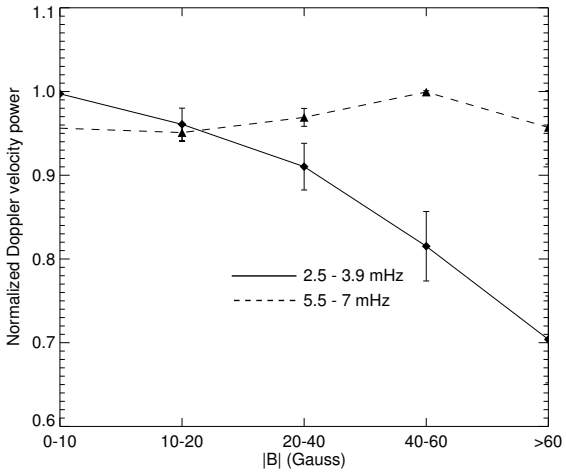

Figure 2.7: Mean of normalized Doppler VP (see the text) as a function of magnetic field ranges shown in the x-axis for various data sets from data type (b). Note the difference in behaviors of the acoustic p-mode (solid line) and high-ν powers (dashed line) with respect to the magnetic field.

In this manner, we can relatively compare the behavior of p-mode and high-ν power at various positions as a function of the magnetic field. We plot this normalized power with respect to various increasing field strength ranges in Figure 2.7. Solid and dashed lines are for p-mode and high-ν mean normalized powers, respectively, for all longitudes. Interestingly, on a relative scale, the way p-modes interact with the magnetic field seems to be the same over a wide range of longitudes. There is a clear drop in the power when we go from weak to strong magnetic field regions. On the other hand, high-ν waves have a different route to follow. The normalized power gradually

increases with an increase in the magnetic field, peaks in the range of $40-60$ G, and decreases in regions of stronger field strength. This is consistent with the earlier findings reported by Jain & Haber (2002).

2.3.4 Influence of the Magnetic Field on Intensity Oscillations

Like velocity oscillations, intensity oscillations exhibit a coupling with the magnetic field. Similar to the VP maps, we integrate the power spectra of *G*-band intensity images in frequency ranges of $2.5 \leq \nu \leq 3.9$ mHz and $5.5 \leq \nu \leq 7$ mHz for respective intensity power maps. Figure 2.8 shows integrated and averaged G-band intensity power for the above-mentioned ν-bands as a function of the magnetic field. The solid line marked in the two panels shows the trend of intensity power at various field strengths (vertical error bars show 1σ standard deviation from the trend). Although there is an intrinsic suppression of G-band power at higher frequencies, for a given frequency band there is a further suppression observed over the strong magnetic regions. To see the power accumulation in the region of interest, we extract the G-band (Set 1) intensity power map at 3.3 mHz (where the velocity signal peaks) using a Gaussian filter with 0.5 mHz FWHM.

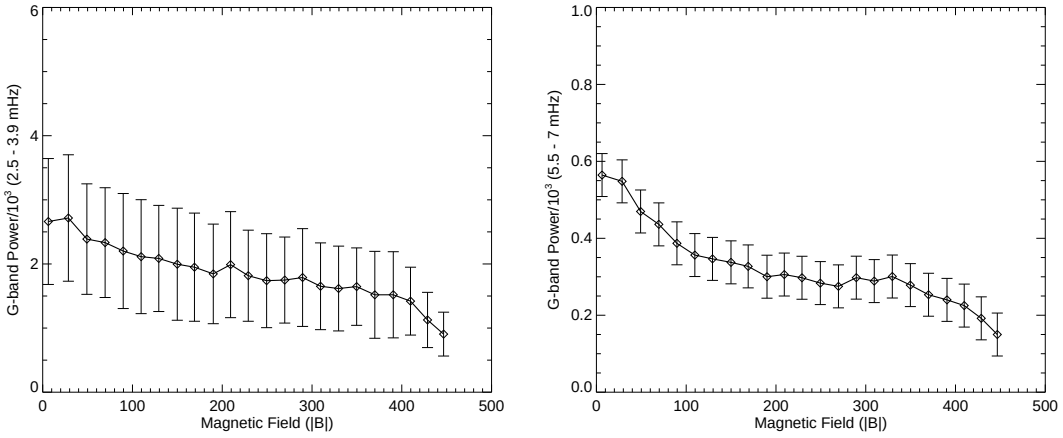

Figure 2.8: G-band (Set 1) intensity power in the units $(\mathrm{DN/s})^2$, integrated over the frequency ranges (left) $2.5 \leq \nu \leq 3.9$ mHz and (*right*) $5.5 \leq \nu \leq 7$ mHz at each pixel for the region shown in Figure 2.1 as a function of magnetic field strength. Mean power for respective -bands is plotted as a function of mean field strength.

In Figure 2.9, we show the contours (in blue) of regions with power $\geq 30\%$ of maximum power on a time averaged intensity map. The suppression of intensity power is observed at the sites of magnetic fields seen as a bright patch in the G-band (also see Figure 2.1). Unlike VP, intensity oscillations (both G-band and high-resolution continuum intensity) do not show power enhancement in the ν-band $5.5-7$ mHz. The power decreases for all frequencies with an increase in the magnetic field strength (see

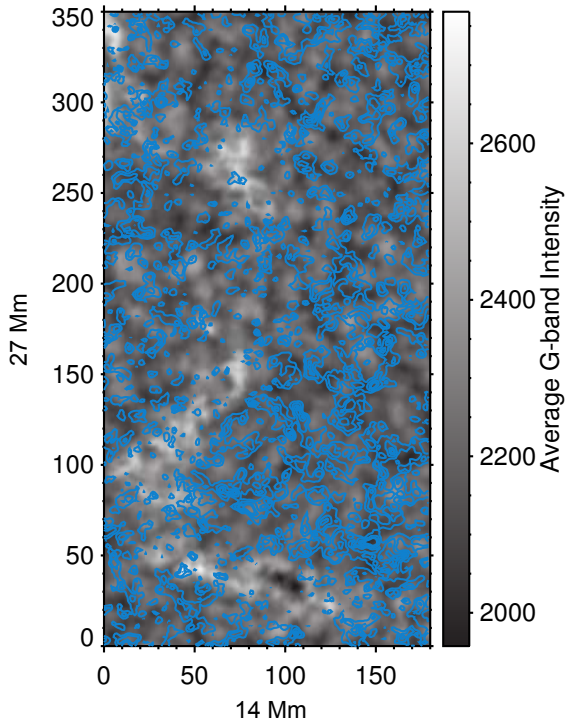

Figure 2.9: 3.3 mHz component of G-band intensity power (in blue contour) is plotted over a 2 hr average G-band (Set 1) intensity map. The contours are drawn for the regions between $0.3-1.0\times$ maximum G-band power at 3.3 mHz. Note that the G-band intensity power is suppressed in the regions of magnetic fields (also see Figure 2.1).

the left panel of Figure 2.10). We plot $\log_{10}$ of the intensity power as a function of frequency for magnetic field[5] ranges (1) $10 < |B| < 100$ G (solid line), (2) $100 < |B| < 200$ G (* * * * line), and (3) $200 < |B| < 457$ G (dashed line). It is clear from the plot that for a given frequency, suppression increases with an increase in the magnetic field strength. The right panel of Figure 2.10 is a plot of $\log_{10}$ of fractional G-band intensity power, which is the ratio of intensity power at each frequency over the total intensity power plotted as a function of frequency for magnetic field ranges (1) $10 < |B| < 40$ G (solid line) and (2) $40 < |B| < 457$ G (dashed line).

The left panel of Figure 2.11 is the same as the right panel of Figure 2.10, except that the plot is for magnetic field[6] ranges (1) $10 < |B| < 40$ G (solid line) and (2) $40 < |B| < 521$ G (dashed line) of the 2007 June 24 data. The main difference in the two data sets is the configuration of the magnetic field. While Set 1 data cover a network region, Set 2 data are more of a scattered field of smaller units in size.

It is clear that both the intensity and velocity oscillations show power suppression with the increase in the magnetic field strength in the p band. It is interesting to see how this oscillatory power (say at 3.3 mHz, where VP is maximum) varies as a function of

[5]Magnetic field values are obtained from *SOHO*/MDI observations.
[6]Magnetic field values are obtained from *Hinode* SOT/SP observations.

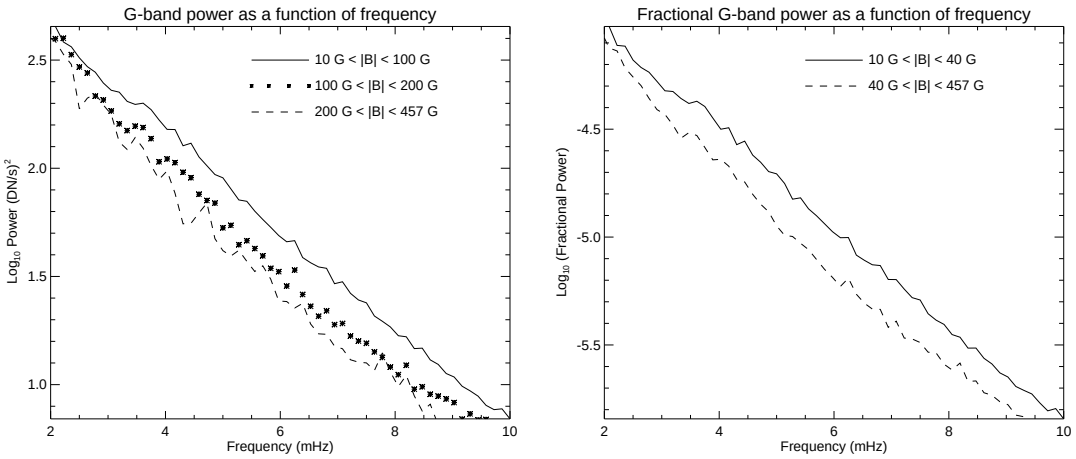

Figure 2.10: G-band (Set 1) power and fractional G-band power as a function of frequency for different ranges of magnetic field strengths for the region shown in Figure 2.1. Note that both power and fractional power of G-band intensity oscillations show suppression above 2 mHz with an increase in the magnetic field.

magnetic field strength. To examine this, the power spectra are filtered using a Gaussian filter of 0.5 mHz FWHM peaking at 3.3 mHz. From the resulting power maps, we calculate the average power for velocity and intensity fluctuations as a function of field strength. The spatial pixels of power maps are sorted with respect to the magnetic field. We then use a 30 G bin to segment the power maps. The average values of power and magnetic field are obtained from each segment. In the right panel of Figure 2.11, we plot the average powers of both velocity ($\diamondsuit$) and G-band, Set 1 ($\triangle$) for 3.3 mHz as a function of mean magnetic field strength with a bin size of 30 G. The slopes of least-squares fit for velocity (solid line) and *G*-band (dashed line) powers indicate a similar nature of reduction in velocity and intensity oscillatory powers with increase in the magnetic field strength. The important result from these observations is that the "acoustic halos," which are ring-like regions of enhanced acoustic power in the high-ν band surrounding the magnetically active regions as described by Braun et al. (1992a) and Brown et al. (1992) are also seen surrounding very small localized fields. These "halos" can be seen as an enhancement in VP in the $5.5 < \nu < 7$ mHz band in Figure 2.4. The power spectrum of intensity fluctuations does not show the presence of such power enhancements or "halos" (see Figure 2.10).

2.4 DISCUSSION

We used G-band intensity data to search for correlations between the small-scale *G*-band bright points and the corresponding underlying photospheric magnetic field and Doppler velocities. The main conclusion we draw is that the G-band intensity, contin-

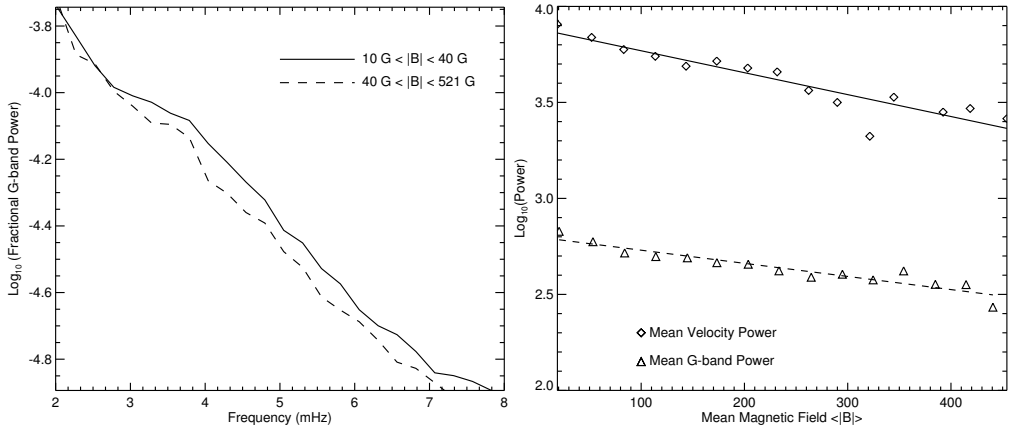

Figure 2.11: Left panel: same as the right panel of Figure 2.10 plotted for Set 2 of G-band data. Suppression is seen in intensity oscillations above 2 mHz. Right panel: $\log_{10}$ of mean VP ($\diamondsuit$, (m/s)^2) and mean G-band (Set 1) intensity power ($\triangle$, (DN/s)^2) at 3.3 mHz for the regions shown in Figures 2.1 and 2.2, respectively, as a function of mean magnetic field strength obtained from binning the time averaged magnetic field strength with a 30 G bin. Solid and dashed lines show the least-squares fit for respective powers.

uum intensity, and Doppler VP are all influenced by magnetic fields and show power suppression in the p band ($\nu < 5$ mHz). The G-band and continuum intensity power also show suppression at high frequencies ($\nu > 5.5$ mHz) whereas the Doppler VP shows enhancements. Also, the small-scale magnetic features show this behavior everywhere, irrespective of their surroundings (i.e., nearer or farther away from a large-scale magnetic region).

What causes the power suppression in *G*-band bright points? The current analysis on MDI and G-band intensity data sets suggests that the suppression seen in high frequency is independent of the height, at least for the spatial resolution used in this study. This implies that the physical mechanism responsible for the power suppression in intensity data does not occur in the upper atmosphere. Also, the small-scale bright points in the G-band and their association with the magnetic field at the photospheric height may mean that this physical mechanism is linked to magnetism. There could be changes in the radiative transfer properties or changes in wave excitation due to magnetic fields, which could lead to such variations in the power spectra. It has been reported by Bogdan et al. (1996) that the buffeting of solar acoustic waves (p-modes) by thin magnetic flux tubes excites magnetohydrodynamic (MHD) tube waves such as *sausage* and *kink* tube waves (see also Spruit, 1984). These tube waves propagate up and down the flux tubes carrying energy away from the p-modes, causing damping and absorption in p-mode power (see Hindman & Jain, 2008; Jain et al., 2009). Jain et al. (2009) theoretically calculated the energy loss in the acoustic waves due to their interaction with thin magnetic flux tubes and compared their acoustic wave absorption results

with helioseismic measurements of plages. However, the thin magnetic flux tubes are present everywhere on the Sun and, although the current observational resolution limits our capability to see deeper into slender flux tubes in detail, in this study we have shown that small-scale magnetic features that may be comprised of many slender flux tubes show acoustic power suppression inside the magnetic features compared to their surroundings. The power suppression must be linked to the excitation of MHD waves.

As for the power enhancement above 5 mHz, there have been some recent investigations. A numerical investigation by Kitiashvili et al. (2011) for low angular degree modes shows interesting results. They suggest that the power suppression for resonant modes is more for vertical magnetic fields compared to inclined fields. They also found that the power is shifted toward higher frequencies when magnetic fields are inclined. This could qualitatively explain the existence of power enhancement seen around magnetic features, but further detailed quantitative investigations are necessary before this argument can be accepted.

Why the Doppler VP shows enhancement at high frequencies is also addressed by Khomenko & Collados (2009) on the basis of a sunspot simulation. They suggest that the acoustic halos are a result of the refraction of high-frequency fast waves from the regions above the equipartition layer. Since the frequencies of trapped p-modes below the cut-off frequency do not reach the equipartition layer, these trapped modes do not contribute to the refraction process. Also, the halos are not seen in the umbral parts of the sunspot because the spectral line (and hence the height of observation) is above the height where refraction occurs (see also Jain & Haber, 2002, regarding the argument on the spectral line formation in magnetic and nonmagnetic regions). Thus, in their simulations, significant halos are seen where the magnetic field is inclined by about $30°-40°$. The power enhancement ratio analyzed in this work shows a slight decrease from center to limb and in the absence of any information on the geometry of the field lines, it is not clear whether the small-scale magnetic features have such a large angle of inclination at photospheric heights. Also, any theory that explains the Doppler power enhancement requires addressing the simultaneous suppression seen in the intensity data at and above the photospheric heights.

The absence of power enhancement in intensity data leads one to believe that the enhancement may be due to the excitation of incompressible kink tube waves at the edges of magnetic tubes (see, for example, Hindman & Brown, 1998). A quantitative analysis for this mechanism is still awaited.

Another relevant point is that small-scale magnetic features such as the ones studied in this work may also act as a local inhomogeneity, which scatters acoustic waves that are incident on them at various angles. Gordovskyy et al. (2009) and Hanasoge (2009) had suggested on the basis of the simulation of trapped p-modes that power is channeled from high mode-mass to low mode-mass p-modes resulting in a power increase for the

high wavenumber part of the p-mode spectrum. Thus they suggested mode mixing as the mechanism for power enhancement seen in high frequencies. Further investigations into this issue are required as the power enhancement is generally seen for frequencies way beyond the cut-off frequencies of p-modes. Also, the amount of scattering will depend on the inclination of field lines, and hence on the height in the solar atmosphere, in addition to other factors such as magnetic field strength and frequencies. In fact, more extended halos are seen around the chromospheric active regions (Brown et al., 1992; Braun et al., 1992b). A complete theory of acoustic wave scattering by an inclined field should give a better quantitative understanding of how scattering influences the suppression/enhancement as a function of height.

We have shown qualitatively that even small-scale magnetic features show a trend in acoustic power suppression similar to large-scale magnetic structures, but a quantitative investigation would require better understanding of the formation heights of the spectral lines. The response functions of the CH molecular line and Ni (also Fe) spectral line, which are used to measure the intensity and Doppler velocity signals, respectively, are expected to be different at different heights in the solar atmosphere. It is also possible that they have relative shifts between the magnetic and non-magnetic plasmas. Thus, it is possible that there will be some systematic error in the fractional power ratios. We have investigated other data sets and our preliminary results suggest that the suppression in acoustic power at small scales, just like large-scale fields, is independent of the spectral line and instrument. However, caution is needed at this stage as observations at a very high spatial resolution can always open possibilities to deal with many of the questions we are trying to address in this work, in a much more effective way.

The similarity between the behavior of acoustic waves at the sites of large- (generated by a global dynamo mechanism) and small-scale features (considered in the present study, which could possibly originate from a local dynamo mechanism) is very interesting to note (e.g., plots like Figure 2.4 obtained from the results of earlier works correspond to the acoustic power in sunspots and plages). All the magnetic elements, irrespective of their size, appear to be subjected to and dominated by the surface effects and interact in a similar way with their surroundings.

Further, the fact that different lines (e.g. ground-based observations of the Fe I 557.6 nm line used by Thomas & Stanchfield (2000), the Ni I 676.8 nm line used in the present study and also for many earlier studies of active regions, and the first results obtained from SDO/HMI, which used the Fe I 617.3 nm line) with different magnetic sensitivities and heights of formation show ring-like regions with enhanced acoustic power in the high-ν band for both large and small magnetic structures should rule out the argument that it could be the sole property of the line that is used for this study. For example, Tripathy et al. (2007) used data from three different spectral lines (Ni I 676.8 nm from the Global Oscillation Network Group, K I 769.9 nm from the Magneto-Optical Filters at

Two Heights (MOTH), and Na I 589.0 nm from MOTH and the Mount Wilson Observatory. Note that the Ni and K lines are formed in the photosphere while the Na line is formed in the lower chromosphere) at different heights in the solar atmosphere to analyze the variation of the acoustic power with height.

Thomas & Stanchfield (2000) discuss the suppression of intensity oscillations seen in Ca II K (which form in the lower to middle chromosphere). Since all Ca II K features have photospheric counterparts when observed in high-resolution G-band imaging, it remains to be seen if the intensity power suppression seen in the chromospheric Ca II line is a result of already suppressed G-band intensity oscillations in the lower atmosphere. From this study we conclude that, irrespective of size and generation mechanism, the presence of any magnetic element (from large to small in spatial size) and its respective interaction with the trapped p-modes and running waves are the same. However, the strength of the interaction varies with respect to the magnetic field strength and also depends on the size of the structure. In other words, the same physical mechanisms are responsible and cause the power suppression (below 5.5 mHz) seen over strong magnetic field regions and the enhancement of "acoustic halos" (above 5.5 mHz) seen in the boundaries of magnetic elements both in magnetically active regions and the quiet Sun magnetic field. A detailed study of the CLV of the above-mentioned interactions will provide an important link toward understanding the nature and source(s) of the "acoustic halos", which has been debated for a long time.

Chapter 3

DYNAMICS OF THE SOLAR MAGNETIC BRIGHT POINTS*

3.1 INTRODUCTION

The discrete and small-scale component of the solar magnetic field is revealed in the high spatial resolution observations of the Sun. Ground-based observations (Muller, 1983, 1985; Berger et al., 1995) show clusters or a network of many bright points (hereafter BPs) in the intergranular lanes, with each individual BP having a typical size of 100–150 km. These BPs are known to be kilogauss flux tubes in the small-scale magnetic field (SMF), and are extensively used as proxies for such flux tubes (Chapman & Sheeley, 1968; Stenflo, 1973; Stenflo & Harvey, 1985; Title et al., 1987, see de Wijn et al. (2009) for a review on the SMF). High-cadence observations and studies show that magnetic BPs are highly dynamic and intermittent in nature, randomly moving in the dark intergranular lanes. These motions are mainly due to the buffeting of granules. The SMF is passively advected to the boundaries of supergranules creating the magnetic network in the photosphere.

Earlier works by several authors have reported mean rms velocities of magnetic elements in the order of a few km s^{-1}. With the ground-based observations of the granules at 5750 Å (white light), Muller et al. (1994) have identified many network BPs with turbulent proper motion and a mean speed of 1.4 km s^{-1}. Berger & Title (1996) have used $G-$band observations of the photosphere and found that the G-band BPs move in the intergranular lanes at speeds from 0.5 to 5 km s^{-1}. Berger et al. (1998) observed the flowfield properties of the photosphere by comparing the magnetic network and nonmagnetic quiet Sun. They show that the convective flow structures are smaller and much more chaotic in the magnetic region, with a mean speed of 1.47 km s^{-1} for the tracked magnetic BPs. With the G-band and continuum filtergrams, van Ballegooijen

*The contents of this chapter are published in Chitta et al. (2012b)

et al. (1998) used an object tracking technique and determined the autocorrelation function describing the temporal variation of the bright point velocity, with a correlation time of about 100 s. Correcting for measurements errors, Nisenson et al. (2003) measured a 0.89 km s^{-1} rms velocity for BPs. Advances in ground-based observations like rapid high-cadence sequences with improved adaptive optics (AO) to minimize seeing effects, and also space-based observations at high resolutions, continued to attract many authors to pursue BP motion studies. For example, Utz et al. (2010) used space-based Hinode G-band images to measure BP velocities and their lifetimes. The BP motions can be used to measure dynamic properties of magnetic flux tubes and their interaction with granular plasma. Photospheric turbulent diffusion is one such dynamical aspect that can be derived consequently from the BP random walk. Manso Sainz et al. (2011) measured a diffusion constant of 195 km^2 s^{-1} from the BP random walk and their dispersion. Abramenko et al. (2011) studied photospheric diffusion at a cadence of 10 s with high-resolution TiO observations of a quiet-Sun area. They found a super-diffusion regime, satisfying a power law of diffusion with an index $\gamma = 1.53$, which is pronounced in the time intervals 10–300 s.

The implications of these magnetic random walk motions have recently been found to be very fruitful. Such motions are capable of launching magnetohydrodynamic (MHD) waves (Spruit, 1981), which are potential candidates for explaining the high temperatures observed in the solar chromosphere and corona. For example, a three-dimensional MHD model developed by van Ballegooijen et al. (2011) suggests that random motions inside BPs (see Figure 1 in their paper) can create Alfvén wave turbulence, which dissipates the waves in a coronal loop (also see Asgari-Targhi & van Ballegooijen, 2012). Observations by De Pontieu et al. (2007b), Jess et al. (2009), and McIntosh et al. (2011) provide strong evidence that the Alfvénic waves (which are probably generated by the BP motions) have sufficient energy to heat the quiet solar corona. To test theories of chromospheric and coronal heating, more precise measurements of the velocities and power spectra of BP motions are needed.

Nisenson et al. (2003) worked on the precise measurements of BP positions, taking into account the measurement errors. The autocorrelations derived by them for the x- and y-components of BP velocity using high spatial resolution and moderate cadence of 30 s observations gave a correlation time of about 60 s, which is twice the cadence of the observations. This suggests an overestimation of correlation time and an underestimation of the rms velocity power, with significant hidden power in timescales less than 30 s, and thus warranting observations at even higher cadence. This is important because the measured power profile, which is the Fourier transform of the autocorrelation function, gives us an estimate of the velocity amplitudes and energy flux carried by the waves that are generated by the BP motions in various, and especially at, higher frequencies.

In this study, we use 5 s cadence wideband Hα observations from the Swedish 1 m Solar Telescope (SST) to track the BPs and measure their rms velocities. For comparison, we also use a 30 s cadence G-band observational sequence from the Solar Optical Telescope (SOT) on board *Hinode*. These independent and complementary results take us closer to what could be the true rms velocity and power profile of the lateral motions of the BPs. The details of the data sets used, analysis procedure, results, and their implications are discussed in the following sections.

3.2 OBSERVATIONS

In this study, we have analyzed time sequences of intensity filtergrams with 5 and 30 s cadence. A brief description of the observations is given below.

5 s data. These high resolution observations were obtained on 2006 June 18, with the SST (Scharmer et al., 2003a) on La Palma, using the AO system (Scharmer et al., 2003b) in combination with the Multi-Object Multi-Frame Blind Deconvolution (MOMFBD; van Noort et al., 2005) image restoration method under excellent seeing conditions. The target area is a quiet-Sun region away from disk center at (x, y)=($-307''$,$-54''$) and $\mu = 0.94$ (see Figure 3.1). The time sequence is of one hour duration starting at 13:10 UT. Here we analyze images from the wideband channel of the Solar Optical Universal Polarimeter (SOUP; Title & Rosenberg, 1981) which received 10% of the light before the SOUP tunable filter but placed after the SOUP prefilter (see De Pontieu et al., 2007a, for the optical setup of the instrument). The prefilter was an FWHM=8 Å wide interference filter centered on the Hα line. The SOUP filter was tuned to the blue wing of Hα at -450 mÅ but those data are not considered here. On the wideband channel, there were two cameras (running at 37 frames per second with an effective exposure time of 15 ms) positioned as a phase-diversity pair with one camera placed at focus and the other placed at 13.5 mm out of focus. The data from the two cameras have been processed with the MOMFBD restoration method in sets of 5 s[2], creating a 5 s cadence time sequence with a total of 720 images. After MOMFBD processing, the restored images were de-rotated to account for the field rotation due to the altazimuth mount of the telescope. Furthermore, the images were aligned using cross-correlation on a large area of the field of view (FOV). The images were then clipped to 833$\times$821 pixels (with $0''.065$ pixel^{-1}), to keep the common FOV (the CCDs have 1024$\times$1024 pixels, some pixels are lost after alignment between focus and defocus cameras).

[2]Between 141 and 176 exposures per camera were used by the MOMFBD restoration method. The cameras were running at 37 frames per second so 5 seconds should amount to 185 exposures. About 10% of the exposures were randomly dropped allowing the system to cope with the high data rate. More details on the MOMFBD restoration method are given in van Noort et al. (2005), van Noort & Rouppe van der Voort (2006), and De Pontieu et al. (2007a).

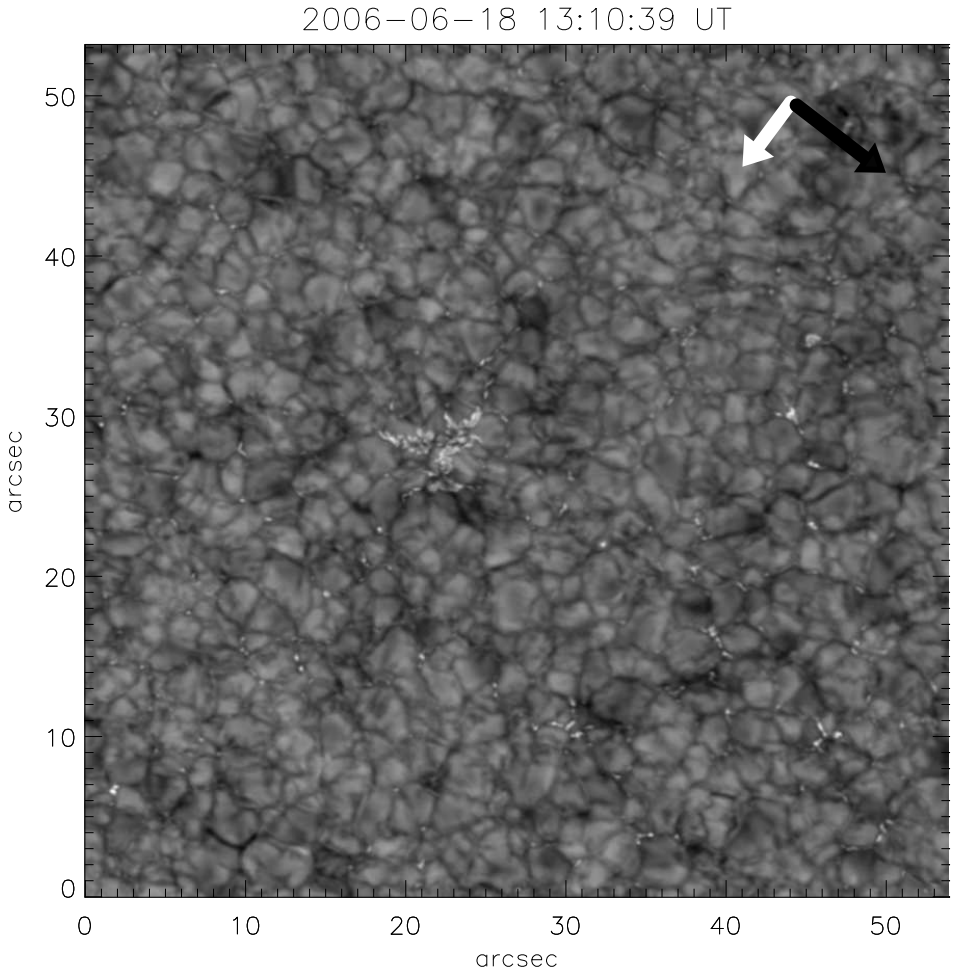

Figure 3.1: First image from the time sequence of SST wideband Hα observations at 13:10 UT on 2006 June 18. The black arrow is pointing toward solar north, subtending an angle of 45° to the vertical axis of the image. The white arrow is toward disk center.

For a reference direction, the solar north in the SST time sequence is found by aligning an earlier SST observation of that day of an active region (AR) magnetogram to a full disk *Solar and Heliospheric Observatory*/MDI magnetogram (the AR was just outside the MDI high-resolution region). From that comparison, we fix the direction of the solar north and disk center (black and white arrows, respectively, in Figure 3.1). Though we do not rotate the images to match the solar north during our analysis, the angles are taken into account at a later stage to correct for projection effects in the velocity measurements.

30 s data. We use G-band filtergrams observed with the SOT on board *Hinode* (Kosugi et al., 2007; Tsuneta et al., 2008) on 2007 April 14. The observations were made for a duration of 4 hr, with a 30 s cadence ($\approx$ 50 ms exposure per frame) in an FOV of $55'' \times 55''$ ($0''.05$ pixel^{-1}; 1024 pixels in both the x- and y-directions), near disk center. The images were processed using standard procedures available in the *solarsoft* library.

3.3 PROCEDURE

In this section, we briefly describe the method of determining the BP positions, and the velocity measurements through the correlation tracking.

3.3.1 Bright Point Positions

We manually select the BPs to estimate their position to a sub-pixel accuracy. We consider the coordinates of maximum intensity of a given BP to be the position of that BP, and the method for measuring these positions involves two steps. In the first step, we visually identify a BP and it is selected for analysis for a period during which it is clearly distinguishable from the surrounding granules. On average, we follow a BP for about 3–5 minutes. The BPs with elongated shapes are not considered for analysis. Also, we stop following a BP if it is substantially distorted or elongated from its initial shape. Though time consuming, manual selection gives a handle on the validity of the positional accuracy of a BP from frame to frame.At each time step, using a cursor, an approximate location (x'_{app}, y'_{app}) of a particular BP is fed to an automated procedure to get its accurate position, which is step two in our method.

Step two is completely an automated procedure. Here, we use a surface interpolation technique to get a precise position of that BP (to a sub-pixel accuracy). The approximate position from the previous step is used to construct a grid of $5\times$ 5 pixels covering the full BP (with (x'_{app}, y'_{app}) as the center of that grid). Now, our procedure fits a two-dimensional, fourth-degree surface polynomial to that grid (using SFIT, an IDL procedure); interpolates the fit to one-hundredth of a pixel; returns the fine location of its peak $(\delta x', \delta y')$ within that grid; and finally stores the accurate position (x'_{BP}, y'_{BP}) of that BP (which is the sum of its approximate and fine positions $(x'_{app} + \delta x', y'_{app} + \delta y')$), for further analysis. Therefore, the position of a BP with index j in a frame i is given by

$$(x'_{BP}, y'_{BP})^j_i = (x'_{app} + \delta x', y'_{app} + \delta y')^j_i, \tag{3.1}$$

and all the coordinates until this point are relative to the lower left corner of the image.

3.3.2 Reference Frame

Though the positional measurements of BPs as described in Section 3.3.1 are accurate, they cannot be directly used to measure the velocities as there are artificial velocity sources, viz., instrumental drifts, seeing variations, jittery motions, and also solar rotation, which vectorially add to BP velocities and thus are required to be removed from the analysis. While *Hinode* (space-based) data are not subjected to seeing variations, SST (ground-based) data have been corrected for seeing as described in Section 3.2. Further,

we need to correct for instrumental drifts, jitters, and solar rotation. Calculating the offsets between successive images is necessary to remove these artificial velocities. In this section, we describe the method of our cross-correlation analysis used to co-align the images.

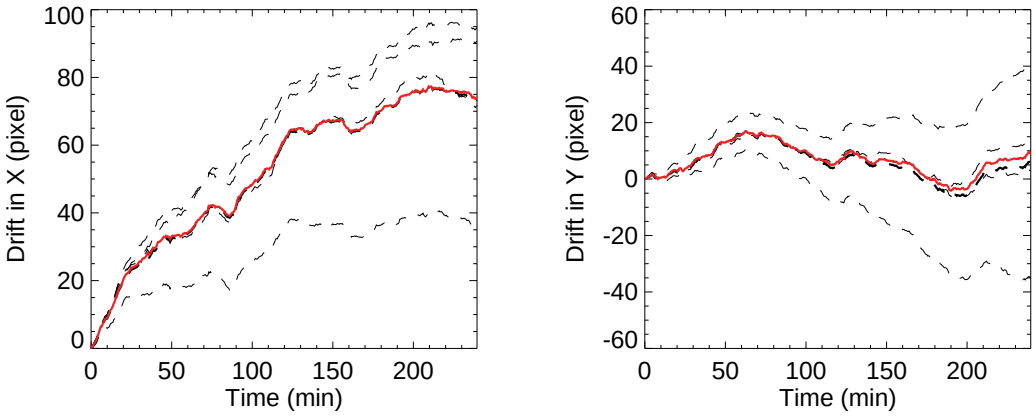

Figure 3.2: Illustration of different offsets seen in the full and partial FOV of *Hinode* data. Dashed curves in the left (right) panel show the drifts in the x- (y-) direction of the four selected quadrants. Thick dashed profile is the average of four dashed curves. Thick red profile is the drift of the full FOV (see the text for details).

Cross correlation (C) of two images $f(x, y)$ and $g(x, y)$ is defined as

$$C = \frac{1}{k-1} \sum_{x,y} \frac{(f(x,y) - \overline{f})(g(x,y) - \overline{g})}{\sigma_f \sigma_g}, \tag{3.2}$$

where, $\overline{f}$ [$\overline{g}$] and σ_f [σ_g] are mean value and standard deviation of $f(x, y)$ [$g(x, y)$], respectively, k is the number of pixels in each image, for normalization. With the above definition of cross-correlation, to get the offsets between two images, we need to shift one image with respect to the other (in both the x- and y-directions) and find at what offsets (independent in x and y) the correlation function attains the maximum value. In general, for shifts of $-l$ to $+\,l$, the cross-correlation is a two dimensional function with $2l + 1$ rows and columns. Let l_x and l_y be the coarse offsets between the two images in the x- and y-directions, respectively, such that the cross-correlation reaches its maximum value: $\max(C) = C(l_x, l_y)$, where $-l < l_x, l_y < l$. To get the sub-pixel offsets, the fine offsets ($\delta l_x, \delta l_y$) are calculated. The method is similar to finding the fine position of BP by using a 5$\times$ 5 pixel grid but now about the (l_x, l_y) of C.

Instead of cross-correlating every successive image with its previous one, we keep a reference image for about 200 s, i.e., a frame i taken at time t (i_t) is used as a reference for the subsequent frames until $t+$ 200 s (i_{t+200}) for cross-correlation. Therefore, the 5 s (SST) and the 30 s (Hinode) data have about 40 and 7 images, respectively, in each set.

By keeping the last image of a set equal to the first image in its next set, we can co-align different sets. In this way, the accumulation of errors in the offsets can be minimized.

Using the above background on co-aligning images to find various drifts, we present the results of drifts found in *Hinode* data. As an illustration, we divide the full (i.e., $55'' \times 55'' \times 4$ hr) Hinode time sequence into four quadrants with $27.5'' \times 27.5'' \times 4$ hr each. Further, we perform correlation tracking (as described above by keeping seven frames per set) on each quadrant separately and plot the results in Figure 3.2. The four dashed lines in the left and the right panels are the offsets in the x- and y-directions, respectively, the thick dashed line in each panel is the average of the offsets (i.e., average of four dashed lines), and the solid red curve is the offset obtained by considering the full FOV. Clearly, in each quadrant, the offsets have a trend similar to that of the full FOV (solid red curve) and an additional component of their own. This additional component is probably the real velocity on the Sun due to flows with varying length scales (for example, supergranular, meso-granular, and granular) and with flow directions changing over areas of a few tens of arcsec^2 on the Sun.

In this work we are mainly interested in the dynamics of the BPs relative to their local surroundings, as granulation flows will have a dominant effect on the BP velocities and their variations on short timescales. Hence, we consider a $5'' \times 5''$ area about the BP as a reference frame for that BP (i.e., keeping the BP in the center of the local area). The cross-correlation is performed on this $5'' \times 5''$ area instead of on the full FOV to get the offsets, which are subtracted from $(x'_{BP}, y'_{BP})_i^j$. The BP positions corrected for offsets are now given by

$$(x'_{BPC}, y'_{BPC})_i^j = (x'_{BP}, y'_{BP})_i^j - (l_x + \delta l_x, l_y + \delta l_y)_i^{j_{local}}, \tag{3.3}$$

where j_{local} represents the $local$ area of BP^j.

In the case of SST data, the observations are off disk center at $(-307'', -54'')$, which corresponds to a heliocentric angle of arccos(0.94). This will introduce a projection effect on the measured horizontal velocities in both the x'- and $y'-$-directions and needs to be corrected. To do this, the coordinate system (x', y') defined by the original SST observations is rotated by 45° in the anticlockwise direction. Now the image plane is oriented in the E–W (parallel to equator, new x-) and N–S (new y-) directions. Further, the E–W coordinate is multiplied by a factor of 0.94^{-1}. Hence, the new coordinate system (x, y) is given by

$$\begin{aligned} x &= (x' \cos 45° + y' \sin 45°) \times \frac{1}{0.94}, \\ y &= (-x' \sin 45° + y' \cos 45°). \end{aligned} \tag{3.4}$$

The SST BP positions $(x'_{BPC}, y'_{BPC})_i^j$, as measured from Equation (3.3), are remapped

to $(x_{BPC}, y_{BPC})_i^j$, using the above coordinate transformations[3].

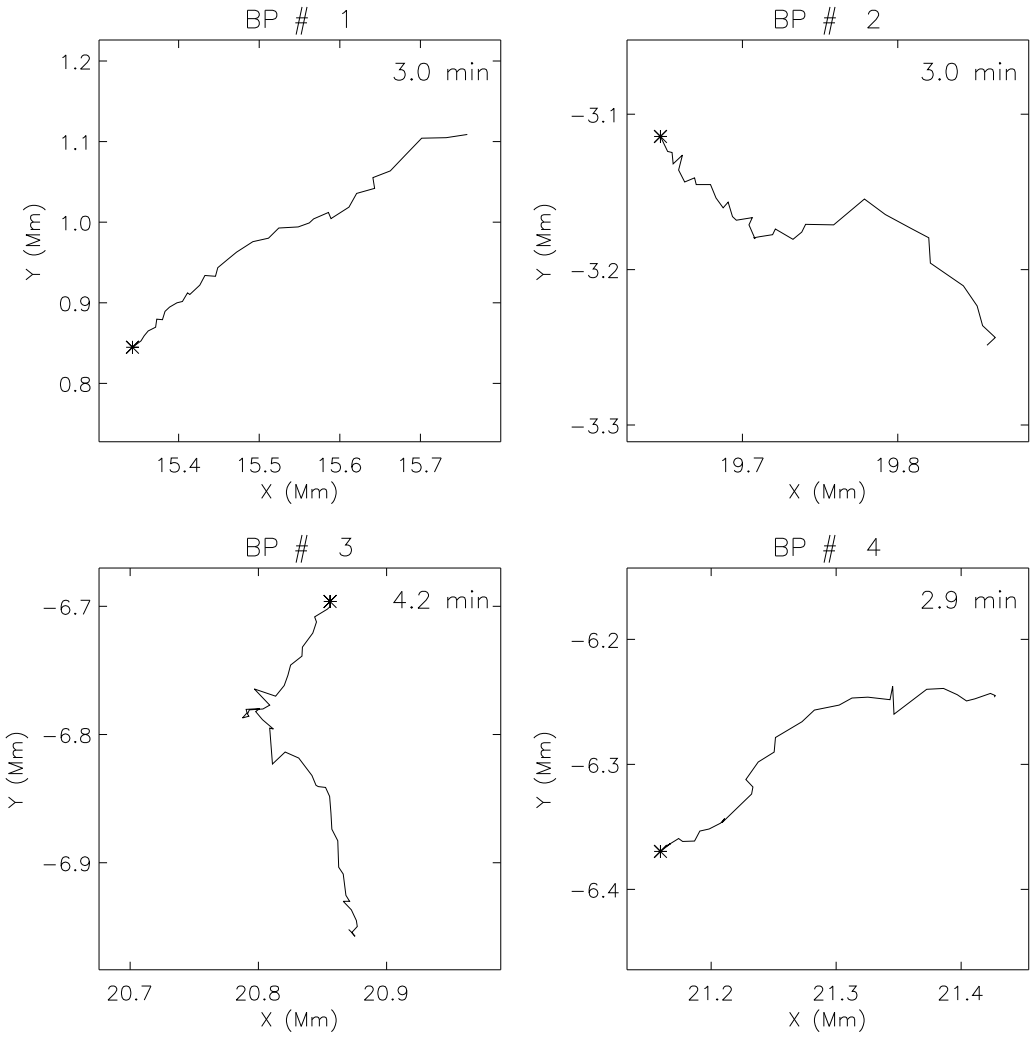

Figure 3.3: Examples of the paths of four BPs taken from the SST data. The initial position of each BP is marked with a star. Time shown at the top right corner in each panel is the duration for which respective BP is followed.

3.4 RESULTS

In this section, we present various results in detail giving more emphasis on the SST results. We have selected 97 SST BPs with ∼3800 individual velocity measurements. [4] Figure 3.3 shows the paths of four individual SST BPs. Some of the BPs move in a relatively smoother path while some exhibit very random motions to the shortest time steps available. BPs drift about a few hundred km in a few minutes. The instantaneous

[3]Note that the transformations in Equation (3.4) are only to modify the *SST* BP positions and in the rest of this work, we use (x, y) for the remapped (x', y') of *SST* and (x, y) of *Hinode*.

[4]Similarly, we have identified 212 *Hinode* BPs with 1950 individual velocity measurements.

velocity $(v_x, v_y)_{i+1}^j$ of a BP is given by $(x_{BPC}, y_{BPC})_{i+1}^j - (x_{BPC}, y_{BPC})_i^j$, multiplied by a factor to convert the units of measured velocity to km s^{-1} (9.4 in the case of SST which is the image scale of SST in kilometers divided by the time cadence in seconds). Figure 3.4 shows the plot of such velocities as a function of time for BP#3 (path of BP#3 is shown in the lower left panel of Figure 3.3). Usually, the changes in the velocity are gradual in time but, sometimes, we do see sudden and large changes in the magnitude and direction of the velocity (for example, at 1 minute in v_x and at 2 minutes in v_y in Figure 3.4). Note that a large change of velocity of one sign is followed immediately by a change of the opposite sign, so the net change in position is not very large. This suggest that these changes are due to errors in the positional measurements. A position error at one time will affect the velocities in the intervals immediately before and after that time. In the following we will assume that such changes in velocity are due to measurement errors. However, we cannot rule out that some of these changes are due to real motions on the Sun on timescales less than 5 s.

Table 3.1: Properties of the Velocity Distributions in Figure 3.5

	v_x (km s^{-1})		v_y (km s^{-1})	
	$\langle v_x \rangle$	$\sigma(v_x)$	$\langle v_y \rangle$	$\sigma(v_y)$
Histogram	0.18	1.58	0.19	1.54
Gaussian Fit ($\sigma_{v,r}$)	0.01	1.32	0.01	1.22
Corrected Distribution ($\sigma_{v,c}$)	0.01	1.00	0.01	0.86

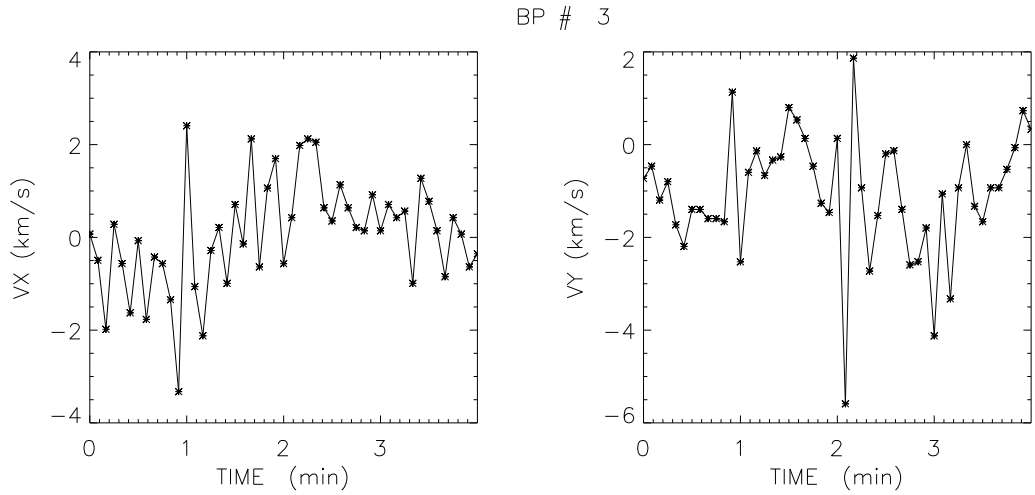

Figure 3.4: Velocities v_x and v_y as a function of time for a typical BP (shown here for BP# 3; see Figure 3.3 for the track of BP# 3).

The means and standard deviations of v_x and v_y are listed in Table 3.1 (first line). Histograms of the distribution of velocities v_x, v_y and $v = \sqrt{v_x^2 + v_y^2}$ are shown in

Figure 3.5 (panels (a), (b), and (c), respectively). Solid lines in panels (a) and (b) are Gaussian fits to the histograms with raw standard deviations ($\sigma_{v,r}$) of 1.32 and 1.22 km s^{-1}. A scatter plot of v_x against v_y is shown in panel (d), which is symmetric in the v-space. However, a small non-zero and positive mean velocity of about 0.2 km s^{-1} is noticed, suggesting that there is a net BP velocity with respect to the 5 arcsec boxes that we used as reference frames. Values of the mean and rms velocities as determined from the fits are also listed in Table 3.1 (second line). These distributions are a mix of both true velocities and measurement errors.

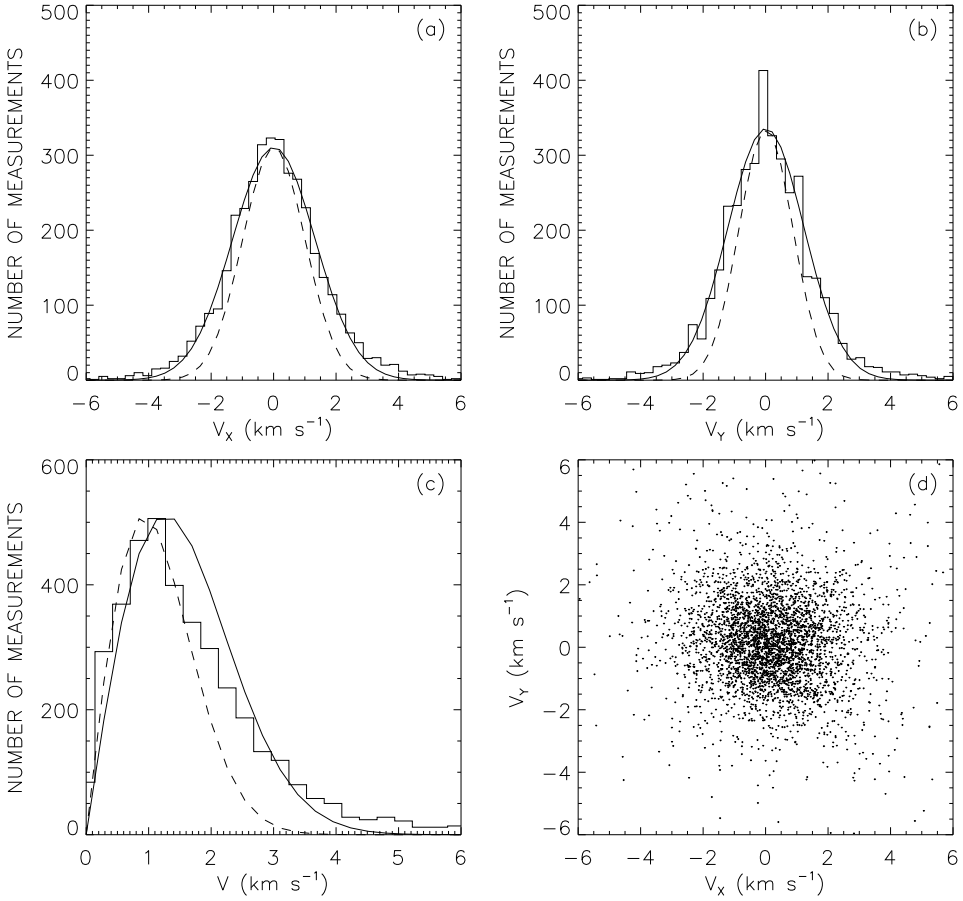

Figure 3.5: Histograms of measured BP velocities: (a) v_x, (b) v_y, (c) $v = \sqrt{v_x^2 + v_y^2}$. Solid Gaussians in the top panels are fits to the histograms. Dashed Gaussians in panels (a) and (b), and dashed Rayleigh profile in panel (c), are the new distributions of velocities after correcting for the measurement errors (see the text for details); panel (d) shows v_x plotted against v_y.

We can gain more insight into the dynamical aspects of the BP motions by studying their observed velocity correlation function $c(t)$, defined as

$$c_{xx,n} = \langle v^j_{x,i} v^j_{x,i+n} \rangle, \quad c_{yy,n} = \langle v^j_{y,i} v^j_{y,i+n} \rangle \tag{3.5}$$

$$c_{xy,n} = \langle v^j_{x,i} v^j_{y,i+n} \rangle, \tag{3.6}$$

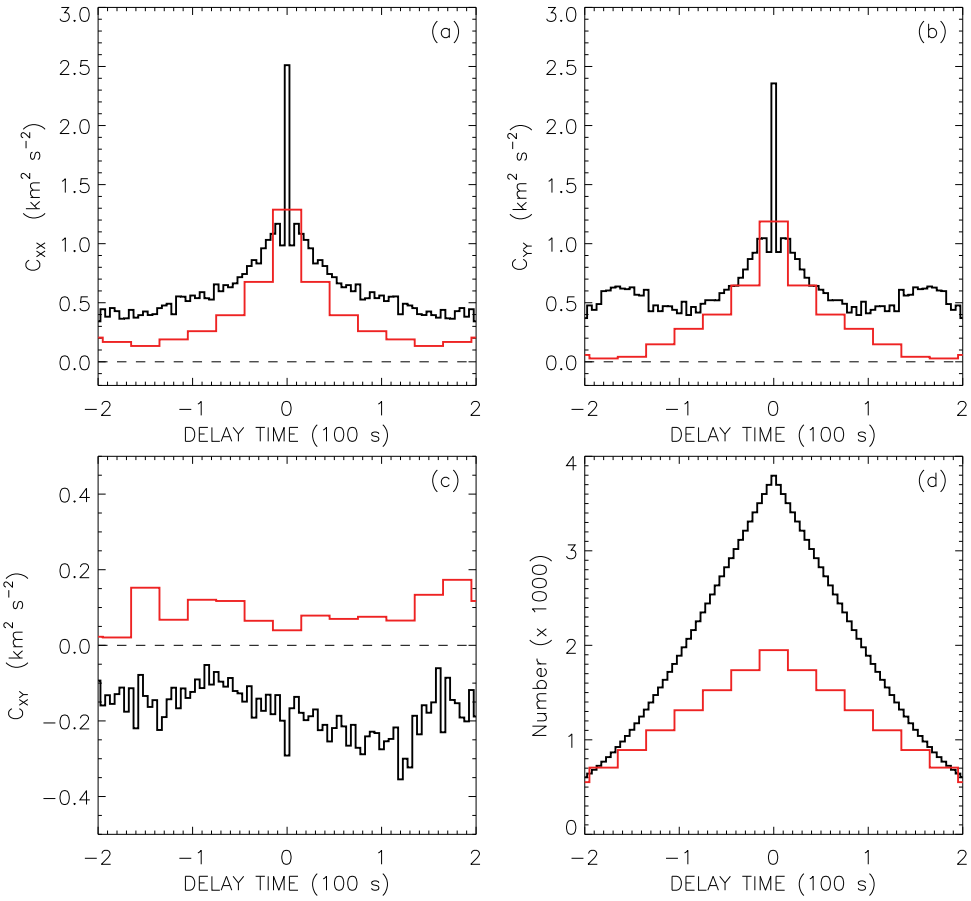

Figure 3.6: Correlation functions of BP velocities v_x and v_y . (a) Observed autocorrelation $c_{xx,n}$ as a function of delay time t (black: SST; red: *Hinode*). (b) Similar for the observed autocorrelation $c_{yy,n}$. (c) Cross-correlation $c_{xy,n}$ as function of delay time. (d) Number of measurements per bin used in panels (a), (b), and (c).

where $c_{xx,n}$, $c_{yy,n}$ are the autocorrelations, and $c_{xy,n}$ is the cross-correlation of v_x and v_y, and n is the index of the delay time. $\langle \cdots \rangle$ denotes the average over all values of the time index i and BP index j but for a fixed value of n. These results are shown in Figure 3.6. Top left and right panels are the plots of c_{xx} and c_{yy}, respectively. Black curves are for the SST, whereas the red curves show the *Hinode* results for comparison. Both the SST and *Hinode* results are consistent for delay times < 1 minute. However, the *Hinode* autocorrelations quickly fall to lower values. This is mainly a statistical error, since we do not have a large number of measurements in the case of *Hinode*. Focusing on periods < 1 minute, it is clear from Figure 3.6 that the core of the autocorrelation plots for the *Hinode* data within ± 30 s delay time, which is sampled with three data points, is now well resolved with the aid of the SST data due to the increased time cadence. Also, at shorter times, c takes a cusp-like profile. Extrapolating this to delay times of the order of 1 s, we expect to see a steep increase in the rms velocities[5] of the

[5]The correlation at zero-time lag is the variance of the velocity distribution.

BP motions. The bottom left panel shows the cross-correlation as a function of delay time. The SST data show a small but a consistent and overall negative c_{xy} while the *Hinode* data show a small positive correlation. We suggest that the real cross-correlation $c_{xy} \approx 0$ and the measured values are due to a small number of measurements with high velocities (largely exceeding the rms values). The lower right panel of Figure 3.6 shows the number of measurements N_n used in the correlation analysis for both the SST and *Hinode* data. To obtain good statistics we collected enough BP measurements to ensure that $N_n \gtrsim 500$ for all bins.

In the rest of the section, we describe the method of estimating the errors in the velocity measurements due to positional uncertainties by analyzing $c(t)$. Following Nisenson et al. (2003), we assume that the errors in the positions are uncorrelated from frame to frame and randomly distributed with a standard deviation of σ_p. Since the velocities are computed by taking simple differences between position measurements (see above), the measurement errors increase the observed velocity correlation at $n = 0$ by Δ (error), and reduce the correlations at $n = \pm 1$ by $-\Delta/2$ where $\Delta = 2(\sigma_p/\delta t)^2$ and δt is the cadence (see Equation (3) in their paper). We define

$$\Delta_n = \begin{cases} \Delta & \text{when } n = 0 \\ -\frac{1}{2}\Delta & \text{when } n = \pm 1 \\ 0 & \text{otherwise,} \end{cases} \tag{3.7}$$

which is valid only with our two-point formula for the velocity. Once Δ is determined, the rms values ($\sigma_{v,c}$) of the true solar velocities can be measured as $\sigma^2_{v,c} = \sigma^2_{v,r} - \Delta$.

A previous study using data from the Swedish Vacuum Solar Telescope (van Ballegooijen et al., 1998) assumed $c(t)$ to be a Lorentzian. Here, we clearly see that $c(t)$ differs from a Lorentzian, and it can be fitted with a function $\mathfrak{C}$, which is a sum of the true correlation of solar origin ($\mathfrak{C}'$) and Δ, given by

$$\mathfrak{C}_n(\Delta, \tau, \kappa) = \mathfrak{C}'_n(\tau, \kappa) + \Delta_n, \tag{3.8}$$

where

$$\mathfrak{C}'_n(\tau, \kappa) = a + \frac{b}{1 + \left(\frac{|t_n|}{\tau}\right)^{\kappa}} \tag{3.9}$$

is a generalized Lorentzian. Δ, τ (correlation time), and κ (exponent) are the free parameters of the fit; a and b are the functions of (Δ, τ, κ), which are determined analytically by least-squares minimization (see Appendix A). We also bring to the notice of the reader that our formula for $\mathfrak{C}$ is a monotonically decreasing function of t_n. However, there is an unexplained increase in the observed c_{yy} beyond ± 100 s (panel (b) in Figure 3.6). To eliminate any spurious results due to this anomaly, we use a maximum

delay time of ± 105 s to fit c with $\mathfrak{C}$ by minimizing the sum of the squares of their difference, as defined in Equation A.1.

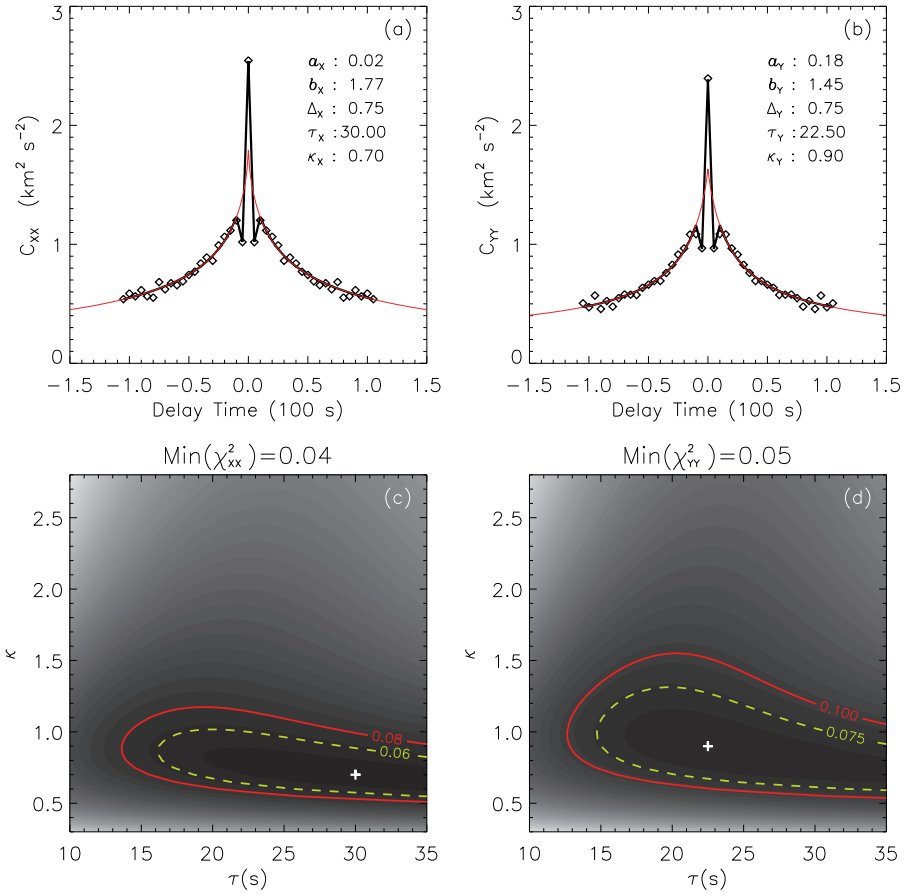

Figure 3.7: Top: $\mathfrak{C}$ (black curve) plotted as a function of delay time with the best-fit values of a, b, Δ, τ, and κ obtained by minimizing the χ^2 (see Appendix A) of the observed c (shown as symbols, c_{xx}: left; and c_{yy}: right, also shown as black curves in the top panels of Figure 3.6), and the modeled correlation function $\mathfrak{C}$, for a delay time of ± 105 s in steps of 5 s. Thin red curve is the profile of $\mathfrak{C}'$. Bottom: Contour plots of χ^2 as a function of κ and τ, for a value of Δ ($\Delta_x = \Delta_y = 0.75$ km^2 s^{-2}), where χ^2 attains the global minimum. Plus symbol is the global minimum of χ^2; dashed and solid lines are the contours of $1.5 \times \min(\chi^2)$ and $2 \times \min(\chi^2)$, respectively.

The top panel in Figure 3.7 shows the results listing the best-fit values of the free parameters (Δ, τ, κ), a, and b for a maximum t_n of ± 105 s. $\mathfrak{C}$ (black) and $\mathfrak{C}'$ (thin red) are plotted as functions of the delay time over $c_{xx,n}$ (left, symbols), and $c_{yy,n}$ (right, symbols). The value of Δ where χ^2 has its global minimum is found to be 0.75 km^2 s^{-2}, for both c_{xx} and c_{yy}. The bottom panel shows the contours of χ^2 as a function of τ and κ at $\Delta = 0.75$ km^2 s^{-2}, and the $\min(\chi^2)$ is denoted by plus symbols. Dashed and solid lines are the regions of 1.5 and 2 $times$ the $\min(\chi^2)$ respectively. χ^2 is a well bounded function for $\kappa < 2$, confirming a cusp-like profile. The correlation time is 22–30 s, which is about 4–6 *times* the time cadence.

Taking into account the variance in errors (i.e., $\Delta = 0.75$ km^2 s^{-2}), we get $\sigma_p = 3$ km, and the corrected rms velocities ($\sigma_{v,c}$) of v_x and v_y are now 1.00 and 0.86 km s^{-1}. These results are plotted as dashed curves in panels (a) and (b) of Figure 3.5, and the values are tabulated in the last row of Table 3.1. The corrected distribution of v is shown as a dashed Rayleigh distribution in panel (c). With higher cadence observations, these results can be refined and modified, as (Δ, τ, κ) depend on the shape of the core of c. By comparing the *SST* and *Hinode* results, we expect that the observed c probably increases rapidly below 5 s and thus changing the set of parameters to some extent.

3.5 SUMMARY AND DISCUSSION

We studied the proper motions of the BPs using wideband Hα observations from the SST and the *G*-band data from Hinode. BPs were manually selected and tracked using 5$''\times$ 5$''$ areas surrounding them as reference frames. The quality of the SST observations allowed us to measure the BP positions to a subpixel accuracy with an uncertainty of only 3 km, which is at least seven times better than the value reported by Nisenson et al. (2003), and comparable to the rms value of 2.7 km due to image jittering reported by Abramenko et al. (2011). They adopted this rms value of 2.7 km as a typical error of calculations of the BP position. We found that the horizontal motions of the BPs in x and y are Gaussian distributions with *raw* (including the true signal and measurement errors) rms velocities of 1.32 and 1.22 km s^{-1}, symmetric in v-space, observed at 5 s cadence. The above estimate of the measurement uncertainty is obtained from a detailed analysis of the velocity autocorrelation functions. For this, we fitted the observed $c(t)$ with $\mathfrak{C}$, a function of the form shown in Equation (3.8), and estimated an rms error of about 0.87 km s^{-1} in v_x and v_y. The removal of this error makes the v$_x$ and v_y Gaussians narrower with new standard deviations 1.00 and 0.86 km s^{-1} (a fractional change of 30%). The total rms velocity (v_x and v_y combined) is 1.32 km s^{-1}. The correlation time is found to be in the range of 22–30 s.

Following is a brief note and discussion on the additional results we derive from our work. BPs are advected by the photospheric flows. Thus, taking these features as tracers, we can derive the diffusion parameters of the plasma. As BPs usually have lifetimes of the order of minutes, the motion of these features can be used to study the nature of photospheric diffusion at short timescales. The mean-squared displacement of BPs $\langle(\Delta r)^2\rangle$ as a function of time is a measure of diffusion. It is suggested in the literature that $\langle(\Delta r)^2\rangle$ can be approximated as a power law with index γ (i.e., $\langle(\Delta r)^2\rangle \sim t^\gamma$, see for example Cadavid et al., 1999; Abramenko et al., 2011). In Figure 3.8, we plot the observed $\langle(\Delta r)^2\rangle$ (symbols) for the 200 s interval on a log–log scale. Solid line is the least-squares fit with a slope of 1.59, which is consistent with the value $\gamma = 1.53$ found by Abramenko et al. (2011) for quiet Sun. Despite the differences in the obser-

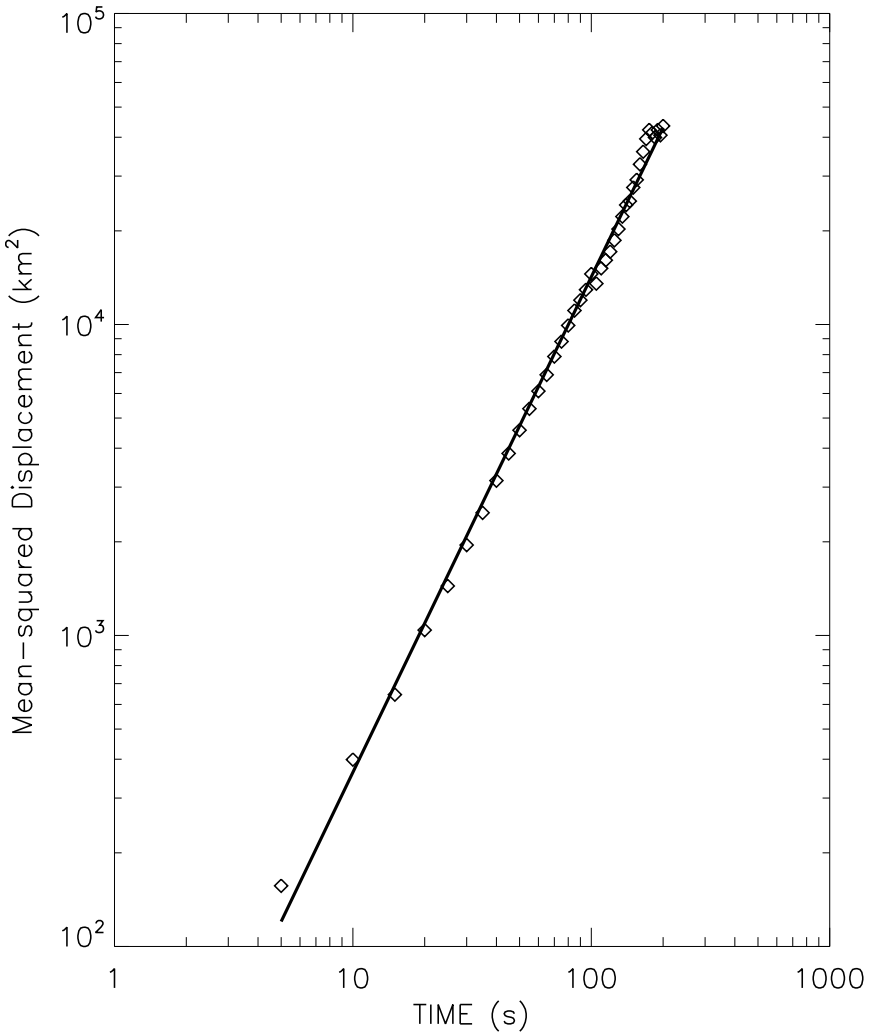

Figure 3.8: Mean-squared displacement $\langle(\Delta r)^2\rangle$ as a function of time t on a log-log scale. Solid line is the least-square fit of the observations (symbols), with a slope of 1.59.

vations (instruments and observed wavelengths), and analysis methods (identification and tracking of BPs), a close agreement in the independently estimated γ suggests that this is a real solar signal.Both these results assert the presence of superdiffusion (i.e., $\gamma > 1$) for time intervals less than 300 s. Since most of the BPs in this study are tracked for only 3–4 minutes, we cannot comment on the diffusion at longer times.

Note that there is a general relationship between the mean-squared displacement $\langle(\Delta r)^2\rangle$ and the velocity autocorrelation function $\mathfrak{C}'$,

$$\langle(\Delta r)^2\rangle \;=\; \left\langle \left(\int_0^t v_x(t')dt' \right)^2 \right\rangle + \left\langle \left(\int_0^t v_y(t')dt' \right)^2 \right\rangle \qquad (3.10)$$

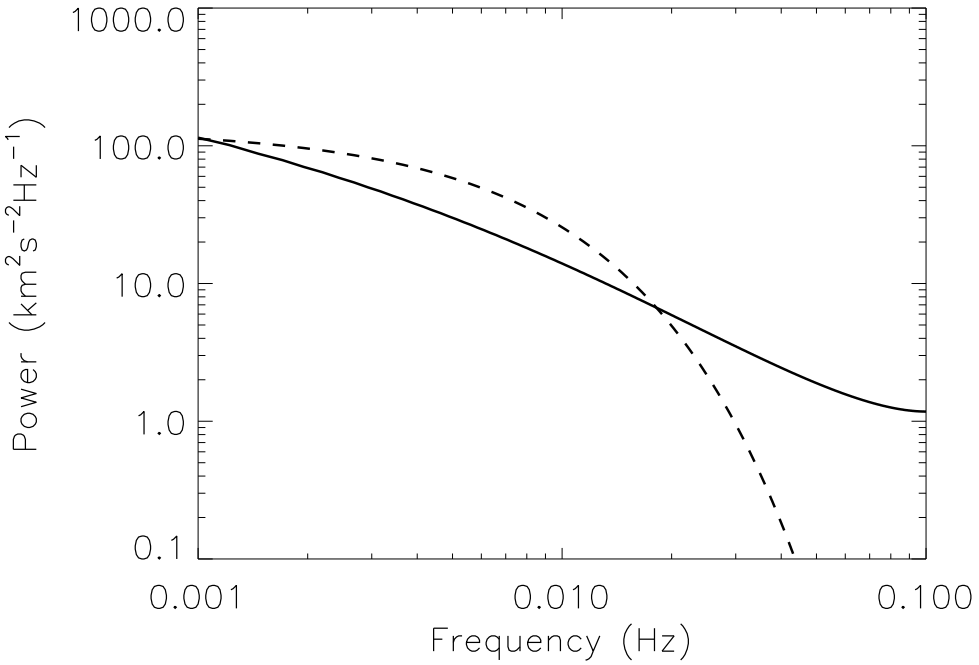

Figure 3.9: Power spectrum of the horizontal motions (due to v_x) of BPs as a function of frequency derived from autocorrelation function for two cases. Solid line: case (a)—from this study. Dashed line: case (b)—from a Lorentz profile with same a, b, and τ as in case (a) but with $\kappa = 2$ (see text for details).

$$= \quad 2 \int_0^t \int_0^t \mathfrak{C}'(t'' - t') dt' dt'', \tag{3.11}$$

where we assume isotropy of the BP motions ($\mathfrak{C}'_{xx} = \mathfrak{C}'_{yy} = \mathfrak{C}'$). For a known auto-correlation or mean-squared displacement, the other quantity can be derived using the above relation.

We already saw that the horizontal motions of the BPs yield several important properties of the lower solar atmosphere. One more such important property is the possibility of the generation of Alfvén waves due to these motions. Here we qualitatively estimate and compare the power spectrum of horizontal motions as a function of frequency for two forms of the velocity correlation function[6]: (a) the form $\mathfrak{C}'$ (Equation (3.9)), obtained in this study, and (b) a Lorentzian function. For case (a) we use $a = 0$, and also assume that $\mathfrak{C}'_{xx,n} = \mathfrak{C}'_{yy,n}$, with the parameters b, τ, and κ taking the mean values of x and y. For case (b) we use a modified form of $\mathfrak{C}'$ with $\kappa = 2$. The other parameters (a, b, and τ) are the same as in case (a). Figure 3.9 shows the power spectra for the two described cases: (a) solid line and (b) dashed line.We observe that for frequencies exceeding 0.02 Hz (< 50 s), the horizontal motions generally have more power in case (a)

[6]Fourier transform of the velocity auto-correlation is the power spectrum.

as compared to case (b). This highlights the fact that the dynamics of the BPs at short timescales are very important. Therefore, it is highly desirable to do these observations and calculations at very high cadence.

The measurements presented in this work provide important constraints of models for Alfvén and kink wave generation in solar magnetic flux tubes. As discussed in Section 3.1, such waves may play an important role in chromospheric and coronal heating. In the Alfvén wave turbulence model (van Ballegooijen et al., 2011; Asgari-Targhi & van Ballegooijen, 2012), it was assumed that the photospheric footpoints of the magnetic field lines are moved about with rms velocity of 1.5 km s^{-1}, similar to the rms velocity of 1.32 km s^{-1} found here. However, the models include only the internal motions of a flux tube, whereas the observations refer to the displacements of the flux tube as a whole. Clearly, to make more direct comparisons between models and observations will require imaging with high spatial resolution (< 0.1 arcsec). This may be possible in the future with the Advanced Technology Solar Telescope.

In this work we presented the results of the BP motions, some of their implications, and use in the context of photospheric diffusion and coronal wave heating mechanisms. We interpret the location of the intensity maximum of a BP as its position at any given time. This is certainly plausible for time periods when we begin to see the physical motion of a BP as a *rigid body* due to the action of the convection on the flux tubes. But at timescales shorter than one minute, other interpretations are also plausible: the motions marked by the intensity maxima could be intensity fluctuations in an otherwise static BP. Nevertheless, these fluctuations are manifestations of some disturbances inside the BP, which are equally important and interesting to explore further.

PART–II

Photosphere to Corona

Chapter 4

OBSERVATIONS AND MODELING OF THE EMERGING EXTREME-ULTRAVIOLET LOOPS IN THE QUIET SUN*

4.1 INTRODUCTION

A part of the magnetic field originating in the photospheric sub-surface layers reaches higher up in the solar atmosphere and forms loop-like structures, the building blocks of solar corona. These loops harbor plasma, which is heated up to a few million Kelvin, much higher than the photospheric temperature. Finding the source and nature of the energy required to heat the corona along with the process of heating is one of the most sought-after questions in the field of astrophysics (for reviews on coronal heating, see, for example, Zirker, 1993; Narain & Ulmschneider, 1996; Klimchuk, 2006; Reale, 2010). Studying the dynamics of the plasma-filled loops is important to understand the heating mechanisms responsible for these high temperatures. Observational, theoretical, and numerical advances have been made over several decades to understand the physics involved in these processes. Some of the early works on this subject include the ideas of damping of magnetohydrodynamic waves in the lower corona to heat the solar atmosphere (Alfvén, 1947, for a recent review on waves in solar corona, see Nakariakov & Verwichte 2005).

From the early X-ray observations (Vaiana et al., 1973), it became evident that the solar corona is confined in the form of loops outlined by the underlying photospheric magnetic field. Later, Rosner et al. (1978) gave an analytical model for the quiescent coronal loops, assuming that these structures are in hydrostatic equilibrium. They sug-

*The contents of this chapter are published in Chitta et al. (2013)

gested that the observations are indicative of a steady-state heating process. Parker (1988), Cargill (1994), and Cargill & Klimchuk (1997) put forward the idea of intermittent and impulsive (nanoflare) heating as a viable mechanism. It is now generally believed, and widely accepted, that the magnetic field plays an important role in generating and transporting the energy required to maintain the temperatures of the corona. It remains unclear and difficult to identify the dominant process responsible for heating of the solar atmosphere.

As the diagnostics of tenuous coronal plasma improved with the advent of high spatial and temporal resolution space-based instruments, an alternate but relevant debate emerged within the community, namely, the frequency of required heating events. The plasma filled in the loops responds to the impulse of heating, and this depends on whether the plasma is reheated before it is completely cooled down (high-frequency model—steady heating), or not (low frequency model—nanoflares). Should either of these models operate, they predict certain physical properties of the loops, which can be compared with the observations (see Reale, 2010, for a broad review on coronal loop observations and modeling).

With a wide range of field strengths and sizes of magnetic elements, coronal loops also have wide temperature and length distributions. Usually, the loops are classified as "hot" ($T > 2$–3 MK), and "warm" ($T \approx 1$–2 MK) depending on their temperature regime. Both steady and impulsive heating models have been extensively used to explain the observed temperatures, loop intensity structure, etc. Studies indicate that the hot plasma is consistent with both steady heating models (Warren et al., 2010; Winebarger et al., 2011) and impulsive heating models (Tripathi et al., 2010; Viall & Klimchuk, 2012). The warm loops are found to be continuously evolving and not in equilibrium (see, for example, Ugarte-Urra et al., 2009), and their properties are well explained by impulsive heating models (Spadaro et al., 2003). It is also suggested that the age of an active region might play an important role in determining the dominance of one process over the other (Schmelz & Pathak, 2012; Ugarte-Urra & Warren, 2012).

The active regions are well studied both in terms of observations and modeling. However, the situation is not so clear in the case of small loops in the quiet Sun. The classification of "hot" and "warm" loops may not be relevant in these features, owing to their compact magnetic structure and narrow temperature range compared to the active regions. These short loops are connected to magnetic bipoles in the photosphere. Their origin can be traced to either flux emergence, or convergence of opposite polarities with reconnection. The magnetic fluxes associated with these regions are typically in the range of 10^{19}–10^{20} Mx. The electron number density in such loops measured using density sensitive lines is in the order of 10^9 cm^{-3} (Ugarte-Urra et al., 2005; Pérez-Suárez et al., 2008; Doschek et al., 2010).

In this study, we are primarily interested in understanding the nature of the heating

that produces the observed 1–2 MK temperature in these small bipoles, in particular the frequency of heating events. Also, to better understand the relation between photospheric magnetic field and the coronal loop temperatures, we chose to study emerging flux events. In these events it is easy to identify the loops, and their footpoints in the photosphere. We follow their formation and evolution over many hours. In the following section, we present the observational results. Section 4.3 describes the loop modeling and the simple heating models we tested in this work. Finally, we summarize the results and discuss some relevant aspects that require further investigation.

4.2 OBSERVATIONAL RESULTS

In this section, we give a brief note on the data sets used and present the results derived, namely, the photospheric magnetic flux, and coronal temperatures. The line-of-sight magnetograms observed with the Helioseismic and Magnetic Imager (HMI; Scherrer et al., 2012; Schou et al., 2012) and the intensity images from the EUV channels of the Atmospheric Imaging Assembly (AIA; Lemen et al., 2012) are used. HMI and AIA are two of the three instruments on board *Solar Dynamics Observatory* (*SDO*; Pesnell et al., 2012). Data are taken from 2011 February 10, and 2012 March 17 observations, spanning for about 12 hr each. *SDO* observes the full disk of the Sun continuously in different filters with a high cadence of 12 s. We selected a region near disk center with the criteria that, we see emerging magnetic field and coronal loops close to the beginning of the selected time sequence. A few cases of evolved bipoles are also considered.

AIA data contain time sequences from 94 Å, 131 Å, 171 Å, 193 Å, 211 Å, and 335 Å EUV channels. Data are processed with standard procedures available in the *solarsoft* library. Alignment between the data from all these channels is crucial. Using 171 Å images as reference, and cross-correlation technique, we aligned all data to within a pixel. The emerging bipoles are identified both in HMI and AIA. The tracked data cubes of such bipoles are extracted for further analysis. To enhance the signal-to-noise ratio, we prepare the 12 s cadence AIA data to 1 minute cadence by averaging five exposures in each channel. Next, to derive the physical properties of the plasma, we adopt the differential emission measure (DEM), which is related to the electron number density (n_e), and the line-of-sight plasma temperature gradient, and is defined as

$$\varphi(T) = n_e^2 \frac{dh}{dT}. \tag{4.1}$$

We use data from six AIA EUV channels, along with the respective filter responses[2]

[2]The filter responses of 94 and 131 Å channels are empirically modified to include contributions from Fe IX and Fe XII for 94 Å, and from Fe VIII and Fe XI for 131 Å. The revised response functions can be obtained using `aia_get_response` with a keyword `chiantifix` available in *solarsoft*.

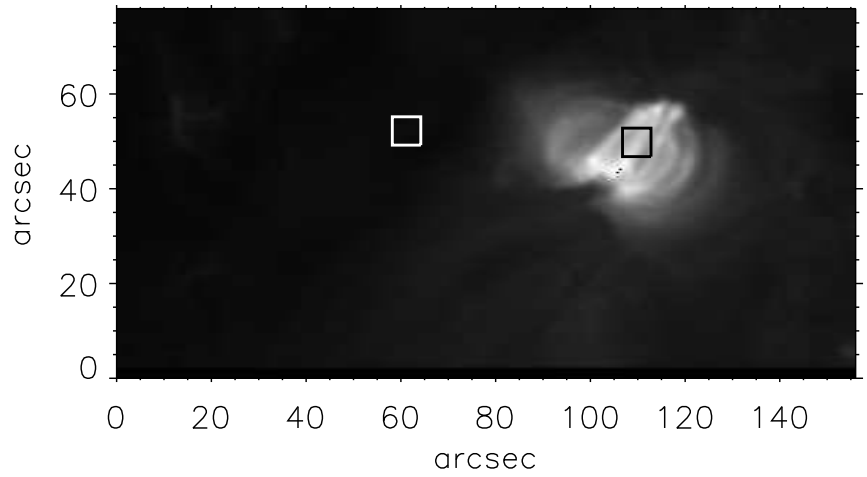

Figure 4.1: Context image showing one of the analyzed bipoles as seen in the AIA 193 Å channel. The regions marked with black (near loop top), and white (background region) boxes are used for further analysis to produce DEMs (see Figure 4.2(a)).

as input to construct DEM(T) (cm^{-5} K^{-1}), using xrt_dem_iterative2.pro (Golub et al., 2004; Weber et al., 2004, distributed in *solarsoft*), at each pixel. In this program, initial DEM is guessed and folded through the filter responses to generate model observations for each pixel, which are iteratively used to reduce the χ^2 between the original and modeled observations. This program uses a much tested IDL routine `mpfit.pro` (Markwardt, 2009) that performs a Levenberg–Marquardt technique to solve the least-squares problem.

We show results from four emerging bipoles in this work. In Figure 4.1, we plot the region of interest for one of the bipoles analyzed, as seen in AIA 193 Å. The image saturates at 750 DN s^{-1}. For these bipoles, a series of DEMs are constructed near the loop top (for example, from a region within the black box shown in Figure 4.1) at each pixel in a $6'' \times 6''$ region, over several hours of observations. The predicted intensities from forward modeling of the derived DEMs match the observed intensities within the limits of errors of photon noise. Since we restrict the DEMs within a limited range of temperature, the predicted intensities will be lower limits of the observed values[3]. In Figure 4.2, we plot the average emission from this area as a function of temperature (log T) for all times. Each panel corresponds to a bipole. Each dot in this plot is for a different time providing the time dependence. At any given temperature, to show the emission distribution in time, we gave a small offset to DEMs in temperature (and that is the reason we see a small spread of DEMs along log T). Additionally, the temporal

[3]This is because the intensity (I) in a given channel (i) is related to the DEM as $I_i \propto \int \varphi(T) R_i dT$, where R_i is the temperature response function of channel i.

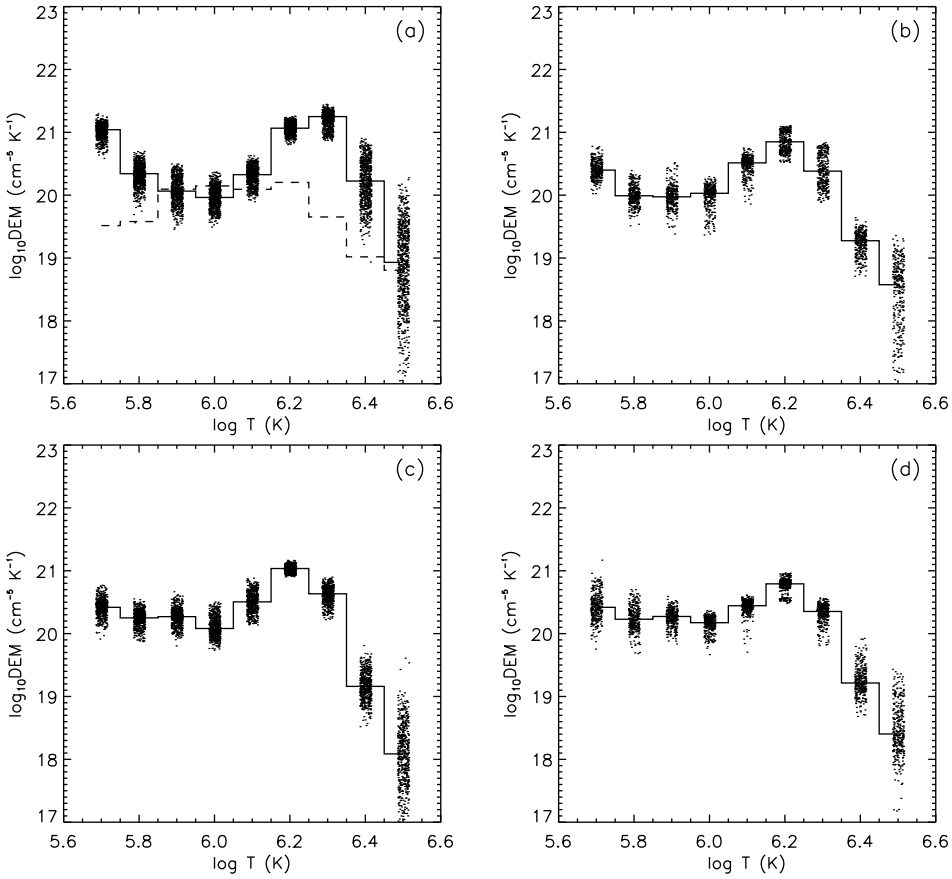

Figure 4.2: DEMs of four bipoles obtained from the observations plotted as a function of temperature for all times (dots). A small offset in temperature is given to the DEMs to show the temporal distribution. Solid line is the temporal median of DEMs obtained for the respective cases. Observed DEMs have a peak around log T of 6.2–6.3. The dashed histogram in panel (a) is the temporal median of five DEMs, at random times, obtained from a *background* region close to the corresponding bipole.

distributions also give a sense for the errors in the DEMs. The solid lines are respective temporal medians for all DEMs. They have a peak close to log T (K) of 6.2–6.3. At higher T, they show a rapid decline and also the DEMs are not well constrained as bulk of the plasma in these structures has $T < 2$ MK. On the other hand, at lower T, the emission stays comparable to the peak emission. Similar results were obtained using *Hinode*/EIS observations, but for a coronal hole bright point (cf. Figure 12, Doschek et al., 2010).

We also note that there is no background subtraction to the data for the DEM analysis. The small loop structures we analyzed have their loop apex and footpoints in the same plane along the line-of-sight (i.e., the loops are not inclined with respect to the line-of-sight), much of the emission contribution may be primarily dominated by the loop apex with a part of it originating from the footpoints. To compare the background contribution to the resulting DEMs, for example panel (a) in Figure 4.2, we considered

a 10×10 pixel *background* region adjacent to that bipole (marked with a white box in Figure 4.1). The DEMs are constructed for this region at five random times, and the temporal median is plotted as a dashed histogram in Figure 4.2(a). This shows that the observed DEM lies well above the background, not only for $\log T$ in the range 6.2–6.4, but also at low temperatures ($\log T \leq 5.8$). The small scatter in the DEM at low T suggests that this emission is real and is not an artifact of the DEM inversion. The DEMs are now used to derive an emission-weighted temperature ($T_{\rm DEM}$) using the relation

$$T_{\rm DEM} = \frac{\Sigma\left\{{\rm DEM}(T_i)T_i\Delta T_i\right\}}{\Sigma\left\{{\rm DEM}(T_i)\Delta T_i\right\}}, \tag{4.2}$$

where $\Delta T_i = 0.1$ in log (T) is the width of the temperature bin around T_i. The time variations of $T_{\rm DEM}$ will be used later for comparison with loop models.

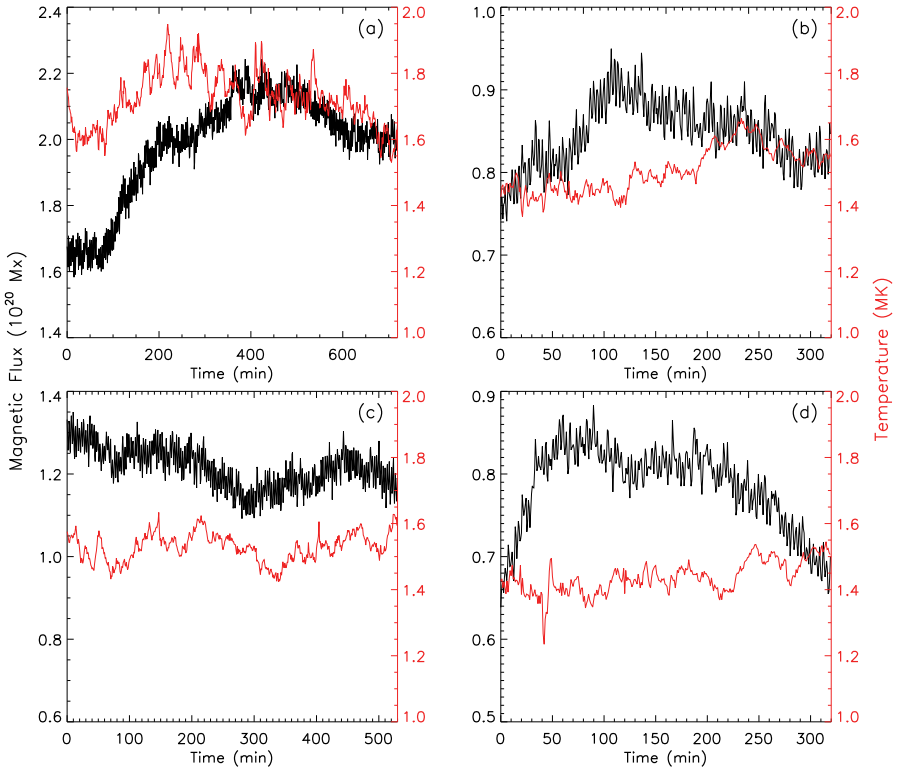

Figure 4.3: Magnetic flux and loop temperatures for a sample of four bipoles. The black curves (left axes) correspond to the integrated photospheric flux of the bipoles. The red curves (right axes) are the emission-weighted, and averaged coronal temperature profiles for the respective bipoles. Panels (a), (b), and (d) are for emerging bipoles, and panel (c) is for an evolved bipole.

Integrated unsigned magnetic flux of both polarities associated with these examples, as a function of time, are also calculated from HMI.[4] Such profiles of temperature and

[4]The two polarities are separated by a distance of approximately 10–15 Mm in the photosphere.

magnetic field for a sample of four bipoles are plotted in Figure 4.3. Three cases of newly emerging bipoles (panels (a), (b), and (d)), and a case of an emerged bipole (panel (c)) are shown. The black curves are time profiles of magnetic flux (10^{19}–10^{20} Mx), and red curves are temperatures in the range of 1–2 MK.

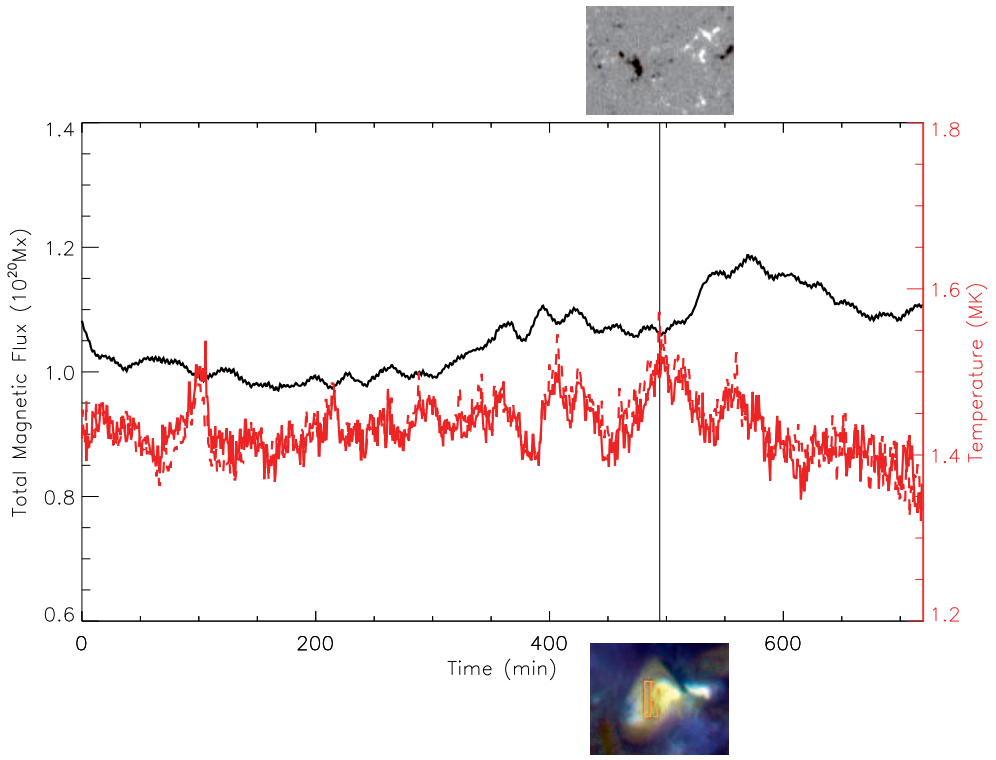

Figure 4.4: Same as in Figure 4.3. Integrated magnetic flux (black curve), and the temperatures (red solid and dashed curves) of an evolved bipole are plotted. A snapshot of the photospheric field configuration (top image, from HMI, $53'' \times 39''$), and the corresponding coronal loop structure (bottom composite image, from AIA 171 Å, 193 Å, 211 Å channels, $60'' \times 48''$) are shown for a particular time as demarcated by the thin vertical line. The solid and dashed red curves are the emission-weighted temperatures derived from 4×25 pixel ($2''.4 \times 15''$) rectangular boxes, from the regions marked in the bottom image respectively. A complete observed evolution of this example is presented as an animation, accompanying this figure.

Though they all fall in a category of emerging/emerged loops, there is no clear relation between the magnetic flux at photosphere and the coronal loop temperature. In other words, it is not trivial to directly relate the field changes in the photosphere to the temperature fluctuations in the corona. For example in Figure 4.3(a), there is a strong correlation between the two physical quantities in the long-term trend, but in panel (b) the temperature seems to increase while the flux decreases. In panels (c) and (d), it is more complicated. We suggest that every emerging bipole may behave differently owing to its surrounding structures both in corona and photosphere. However, a common

signature is that the temperature fluctuates/rises at some stage in the emergence process.

To further illustrate this behavior, we consider another example of an emerged bipole. In Figure 4.4, we plot the magnetic flux (black curve) and temperatures (red curves) of this bipole. A sample image of this example from a particular time is also shown above (magnetic structure), and below (coronal loop) the plot. The thin vertical line demarcates the time of snapshot. The solid and dashed red curves are average temperatures derived from two adjacent regions (marked with solid and dashed lines in the image below the plot), of $2''.4 \times 15''$ size each. In the accompanying animation, it is observed that the drop in temperature after 500 minutes is due to the reconnection (in the corona) of the parent bipole with the adjacent opposite polarity regions, changing the topology of the field, and completely disrupting the main loop. Hence, the observed temperature of the loops originating from small ephemeral regions possibly depends on various factors.

4.3 LOOP MODELING

Temperature profile of the loop is a good diagnostic for the loop dynamics but to get a better picture, we also need to estimate the heating rate required to produce the observed temperatures. To this end, we use enthalpy-based thermal evolution of loops (EBTEL; Klimchuk et al., 2008; Cargill et al., 2012). EBTEL is a time-dependent zero-dimensional (0D), hydrodynamic coronal loop model. For a given loop half-length and volumetric heating rate, the code returns the loop properties in terms of average temperature, density, and pressure of the loop and also the values of these quantities at the loop apex (see Appendix B).

We use EBTEL to model and derive the properties similar to the observed loops (we consider the example shown in Figure 4.3(a) for this purpose). The properties include the DEM as a function of temperature, and the emission-weighted temperature. We compare three different heating scenarios and discuss the results. For the models presented in the next three subsections, we make the following assumptions: (1) a loop is comprised of hundred individual strands, each with a constant length[5] of about 18 Mm, and a uniform radius of about 0.1 Mm. In Figure 4.5, we plot the length and radius of a single strand as a function of time (thick solid and dashed lines, respectively). (2) Each strand is randomly heated with a certain heating profile over a period of 500 minutes. (3) The average values of various physical quantities over all the strands represent the properties of the whole loop. Along with these assumptions, the heating events are chosen such that the modeled emission weighted temperatures closely match the observed temperatures.

[5]This is only a rough estimate of the length based on the footpoint separation in the photosphere.

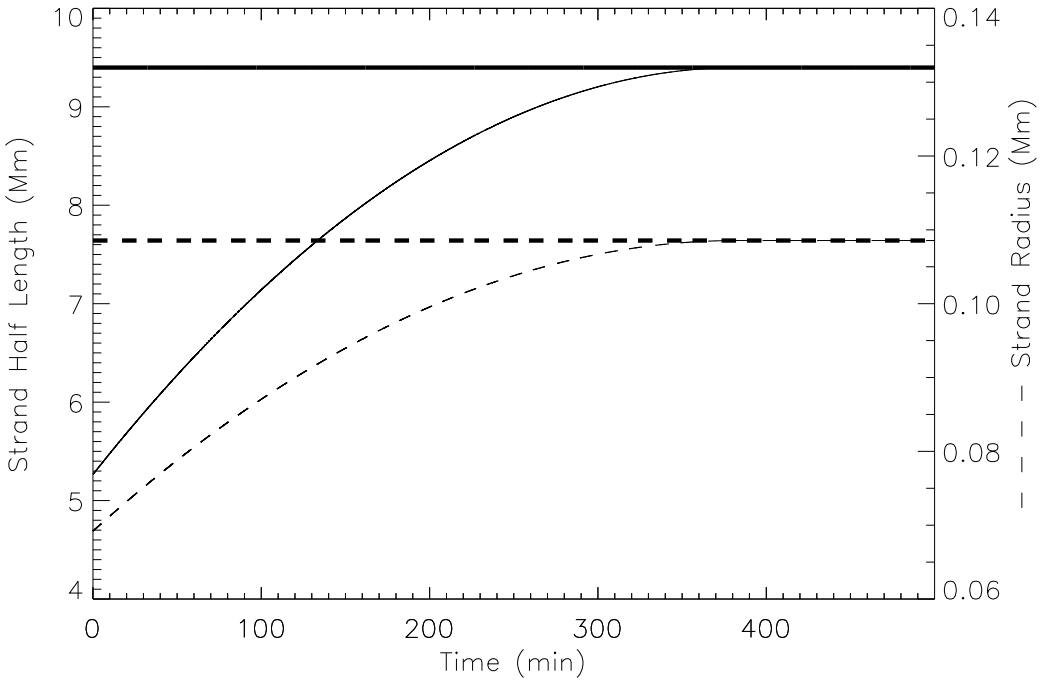

Figure 4.5: Physical dimensions of the strands used in this study. Thick solid and dashed lines, respectively, are the half-length and radius of a constant strand. Thin solid and dashed curves, respectively, are the half-length and radius of an expanding strand.

In Section 4.3.1, we describe the medium-frequency heating model. Section 4.3.2 deals with the low-frequency heating model. A medium-frequency hybrid heating model is discussed in Sections 4.3.3, and 4.3.4. In Section 4.3.5, we present an alternate explanation for the observed DEMs by considering a non-uniform cross-section of the loop.

4.3.1 Medium-frequency Heating Model

In the medium frequency heating model (case 1), individual strands are randomly heated with heating rates having 50–100 s temporal fluctuations. These rates are generated by a sequence of random numbers, and further filtering the signal within the desired band of periods. The base or minimum heating rate is 10^{-6} erg cm^{-3} s^{-1}, and the amplitude of the fluctuations varies by up to four orders of magnitude. The average heating rate for a single strand, over the entire duration of 500 minutes is about 4×10^{-3} erg cm^{-3} s^{-1}.

A representative heating rate for one of the strands is plotted in Figure 4.6(a). The plasma is reheated continuously before it is cooled to the equilibrium temperature due to base heating. In panel (b), we plot the resulting temperature of the strand apex (black, left axis) along with the resulting strand density (red, right axis). The temperature vari-

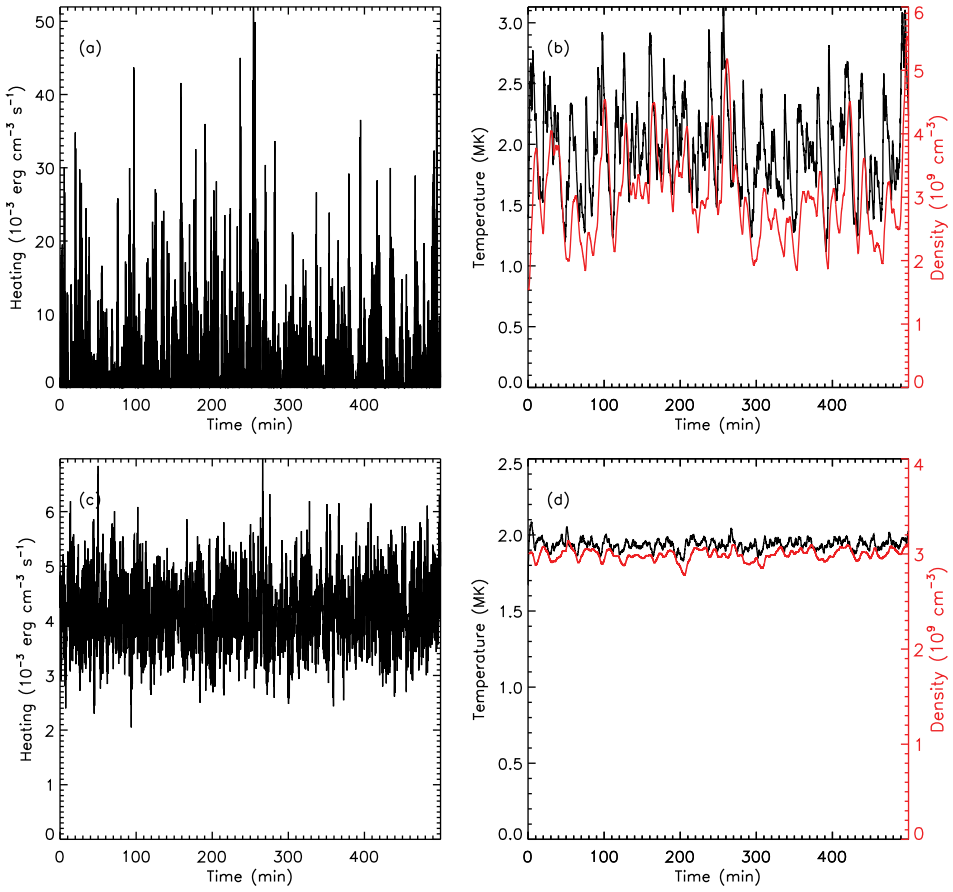

Figure 4.6: Results from a medium-frequency heating model (case 1). All the hundred strands are heated with an approximately same average heating rate. (a) A representative input heating given to a single strand with temporal fluctuations of 50–100 s. The base heating rate is 10^{-6} erg cm^{-3} s^{-1} for all the strands. The amplitudes of the heating rate fluctuate up to four orders of magnitude. (b) The resulting temperature of the strand apex (black, left axis), and loop density (red, right axis) for the heating profile shown in panel (a). (c) The average heating rate of hundred random realizations. (d) The average loop apex temperature (black, left axis), and the average loop density (red, right axis) averaged over hundred strands, representing an observed loop.

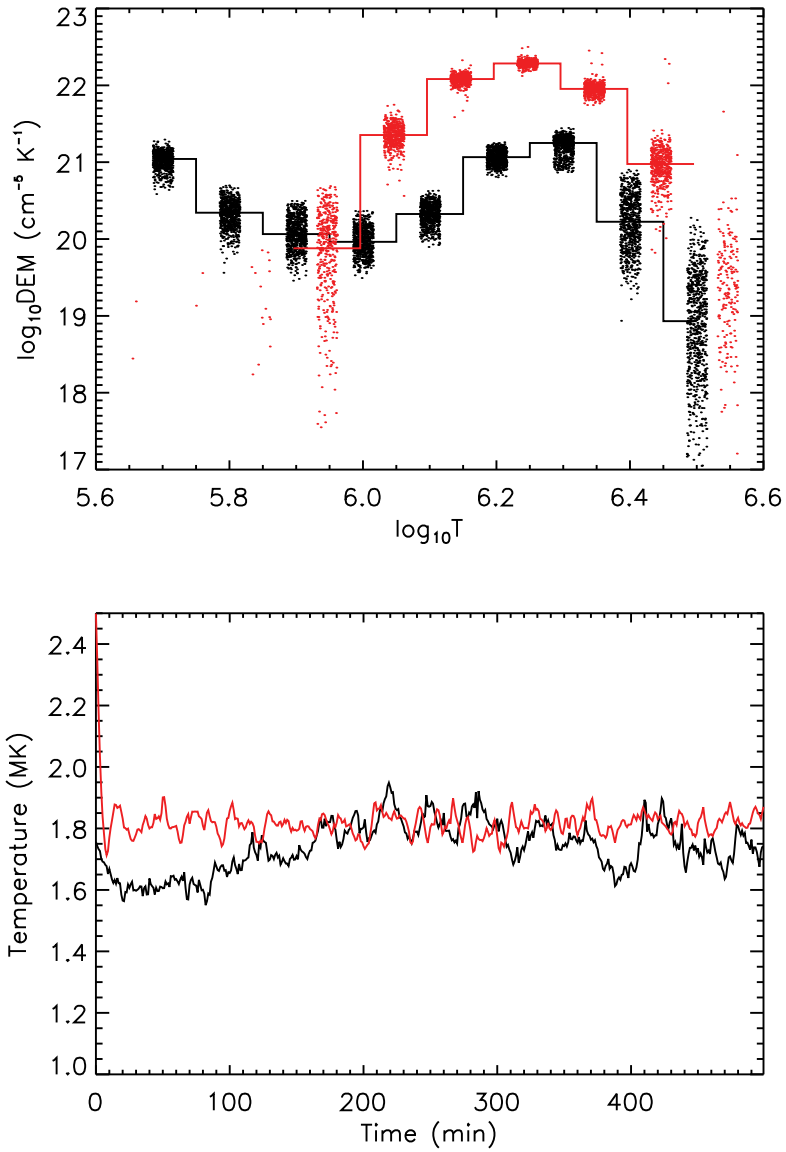

Figure 4.7: Comparison of DEM results obtained for case 1 with the observations. Top panel: DEMs from observations (black dots), and the modeled DEMs (red dots) are shown. All DEMs are given small temperature offsets for a better visualization of the distributions. The black and red solid lines are the temporal medians of the observed and modeled DEMs respectively. Bottom panel: emission-weighted temperature derived from observations (black) and modeling (red).

ations are 1–3 MK for a single strand. Panel (c) is the average heating rate of all strands as a function of time. It should be noted that the frequency of this average quantity is not a relevant factor in distinguishing between various heating cases. Similarly, in panel (d) we plot the average loop apex temperature (black, left axis), and the average loop density (red, right axis). Since the observed temperatures are derived from weighing the emission distribution, temperature of the loop apex in panel (d) cannot be directly compared with its observed counterpart.

In the top panel of Figure 4.7, we plot the observed DEMs (black dots). The observed DEMs have a broad distribution in temperature with a peak at log T of 6.3 and another peak at log T of 5.7 (same as Figure 4.2(a)). The modeled DEMs, which have a narrow distribution, are plotted as red dots with a similar temperature offset. Since there are heating events occurring almost continuously compared to the cooling time of the strands, the loop has no time to cool down completely and the temperature stays steady, with small fluctuations. Because of this reason, all the emission comes from a narrow distribution of temperatures, which is reflected in the modeled results.

The bottom panel is the resulting emission-weighted temperatures from observations (black) and modeling (red). Note that the range, and level of fluctuations in the temperature match very well, but modeled DEM has a peak at log T of 6.25, and the predicted emission about this temperature is at least an order of magnitude greater than the observed values. Further, the model predicts a weak or no emission at lower T. By increasing the magnitude of heating rate to match the temperature at which the peak emission occurs, it will inherently increase the emission, and also the weighted temperature well beyond the observed T.

4.3.2 Low-frequency Heating Model

In the low-frequency heating model (case 2), each strand is impulsively heated five times with an average of 100 minute interval between each impulse. Each triangular pulse has a width of 500 s and a peak input of 10^{-2} erg cm^{-3} s^{-1}. Further, the base heating remains the same as in case 1. In Figure 4.8(a), we plot a sample profile of heat input given to one of the strands. Panel (b) is resulting temperature and density. Note that once the temperature reaches a maximum value, it takes about 70 minutes for the strand to completely cool down. This cooling time depends on the parameters fixed for this case.

The average heating rate in panel (c) is less by a factor of ten compared to that of case 1. It can be seen that the temperature (panel (b)) in this model has a broad distribution, which is reflected in a very broad DEM distribution shown in Figure 4.9 (top panel, red). At log T of 6.5 the model produces a well-constrained DEM that is higher than the observed DEM, although the observations are less constrained at those

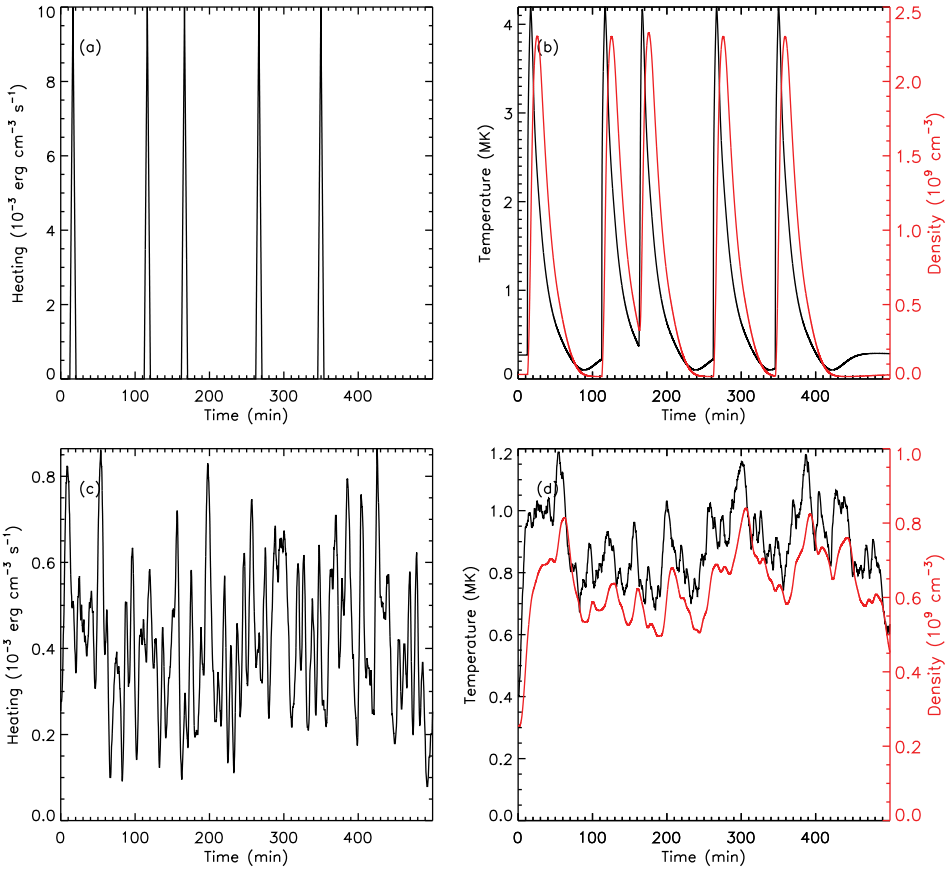

Figure 4.8: Same as Figure 4.6. Results from a low-frequency (impulsive) heating model (case 2). On average, each strand is heated every 6000 s once, with a triangular heating pulse having a maximum of 10^{-2} erg cm^{-3} s^{-1}, and a width of 500 s.

temperatures. Also, the model predicts an overall higher emission at log $(T) \approx 6.0$

The predicted emission-weighted temperature (bottom panel, red) is comparable with observed temperature (bottom panel, black). The level of fluctuations and the short term trend in the red curve are higher than that is seen in the observations. Furthermore, if the number of heating events is fewer than that is considered here (five), but with stronger impulses, the fluctuations now become noticeably large, and the observations should reveal these features.

4.3.3 Medium-frequency Hybrid Heating Model

For cases 1 and 2 we adjusted the model parameters such that the DEM-weighted temperature ($T_{\rm DEM}$) roughly matches the observed temperature for region 1. However, we find that the overall structure and features of the predicted DEM(T) do not match the DEM(T) derived from AIA observations. Therefore, neither of these models are fruitful in describing the 1–2 MK emerging loops in the quiet Sun. We suggest that the heating events may have a broad range, and/or a population of different heating amplitudes,

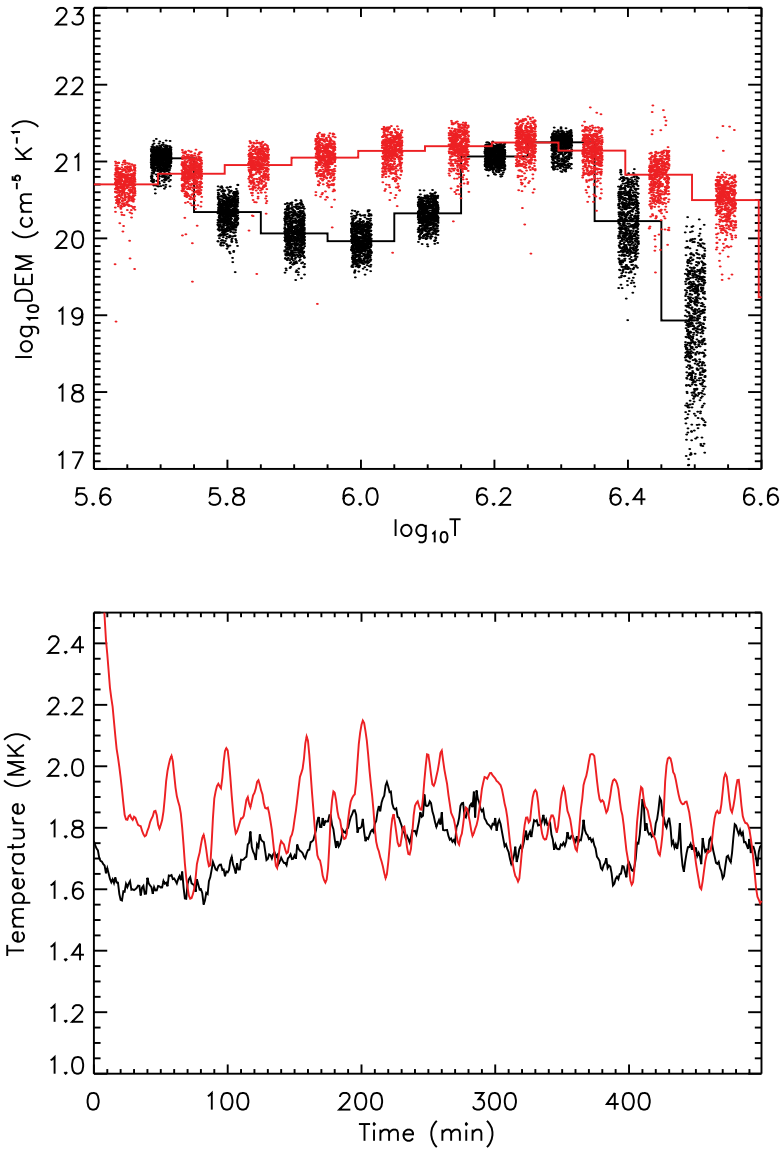

Figure 4.9: Same as Figure 4.7, but obtained for case 2.

influencing different strands.

From the observational point of view, each strand in the loop is dynamically evolving and the lifetime of this unit is not clearly known. New strands emerge with the photospheric flux and replace the older ones in the loop. To investigate this problem further, a hybrid heating model (case 3) has been considered. In this model, we start with a simple assumption that 20% of the strands are rapidly heated with an excess amount of the average heating rate of 50 times greater than the remaining 80% of the loops. All loops receive a base heating similar to that of cases 1 and 2.

In Figure 4.10, we plot the heating rates, temperature, and densities and also the respective average quantities. The profile in panel (a) is a low-amplitude heating for a strand in the 80% population. The profiles shown in panel (b) are similar to those of Figure 4.6(b), except for the overall lower values. Panels (c) and (d) show results

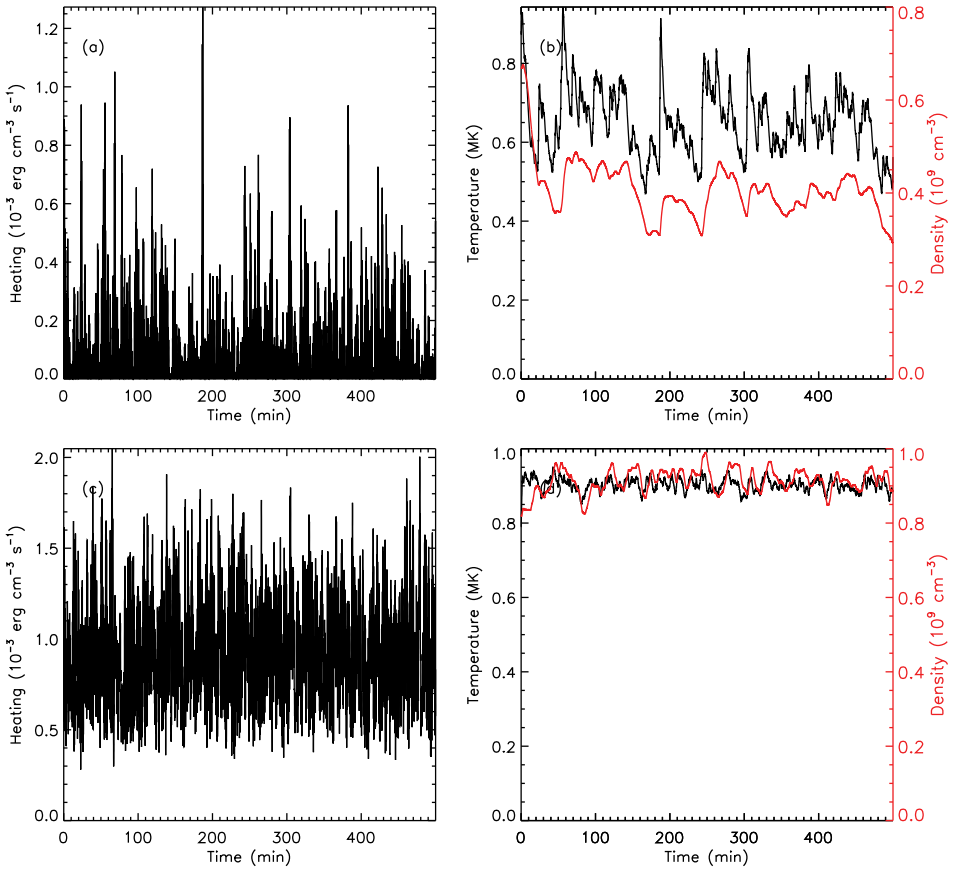

Figure 4.10: Same as Figure 4.6. Results from a medium-frequency hybrid heating model (case 3). Twenty percent of the strands are subjected to higher average heating inputs, but with same temporal fluctuations as in case 1 (see the text for details). Shown in panel (a) is an example of lower heating rate case.

averaged over all the strands, including the 20% that receive a higher level of heating. In Figure 4.11, we show the DEM results for this case. The top panel is for the observed (black) and predicted (red) DEMs. We see that the predicted DEMs now have two distributions, clearly originating from the two populations of heating events. It is interesting to note how closely the observed and predicted DEMs match. The emission weighted temperature is shown in the bottom panel of Figure 4.11. The fairly well-reproduced quantities from this model suggest that a coronal loop, which has a bundle of many strands, can be heated by considering different amplitudes of medium-frequency heating events. This is certainly a plausible assumption, because these emerging bipoles evolve continuously, and various reasons can contribute to different heating episodes.

Alternatively, we can also assume that each strand spends 20% of its time being heated to higher values (similar to the 20% strands case described previously), and the remaining time to lower values. Both the scenarios produce similar results. In Figure 4.12, we plot the results from this alternative case. Panel (a) is a sample heating profile showing both low and high heating events. In panel (b) the loop apex temperature

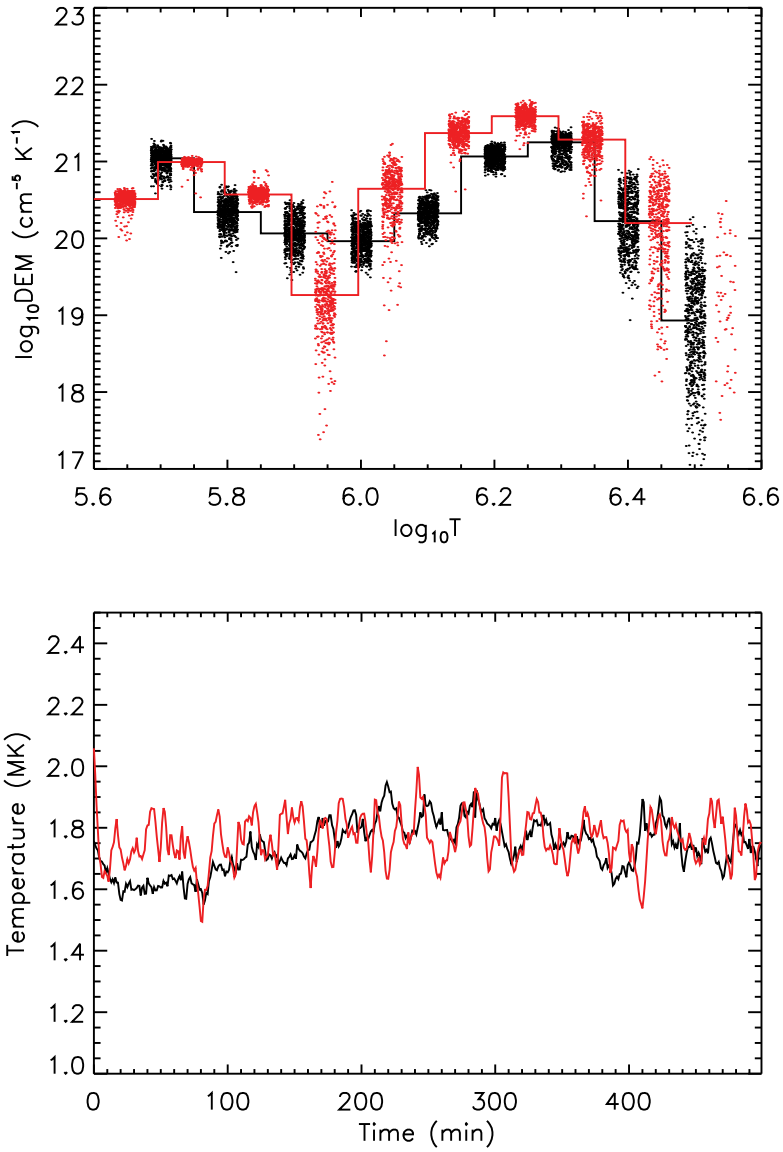

Figure 4.11: Same as Figure 4.7, but obtained for hybrid heating model (case 3).

and density are shown. In panel (c), the observed (black), and predicted (red) DEMs are plotted along with their respective temporal medians.

4.3.4 A Case of Expanding Loop

In general, the coronal loop length increases with time as it emerges through the solar atmosphere. Also, the area as a whole, as the strength of the magnetic field drops with height, the area of strand increases with time. Due to this expansion, filled-in plasma may experience additional adiabatic cooling effects, as the loop pressure and density are modified by the volume change (see Appendix B). We tested heating model described in case 3 on a slowly expanding loop, comprised of hundred strands as explained in the previous sections.

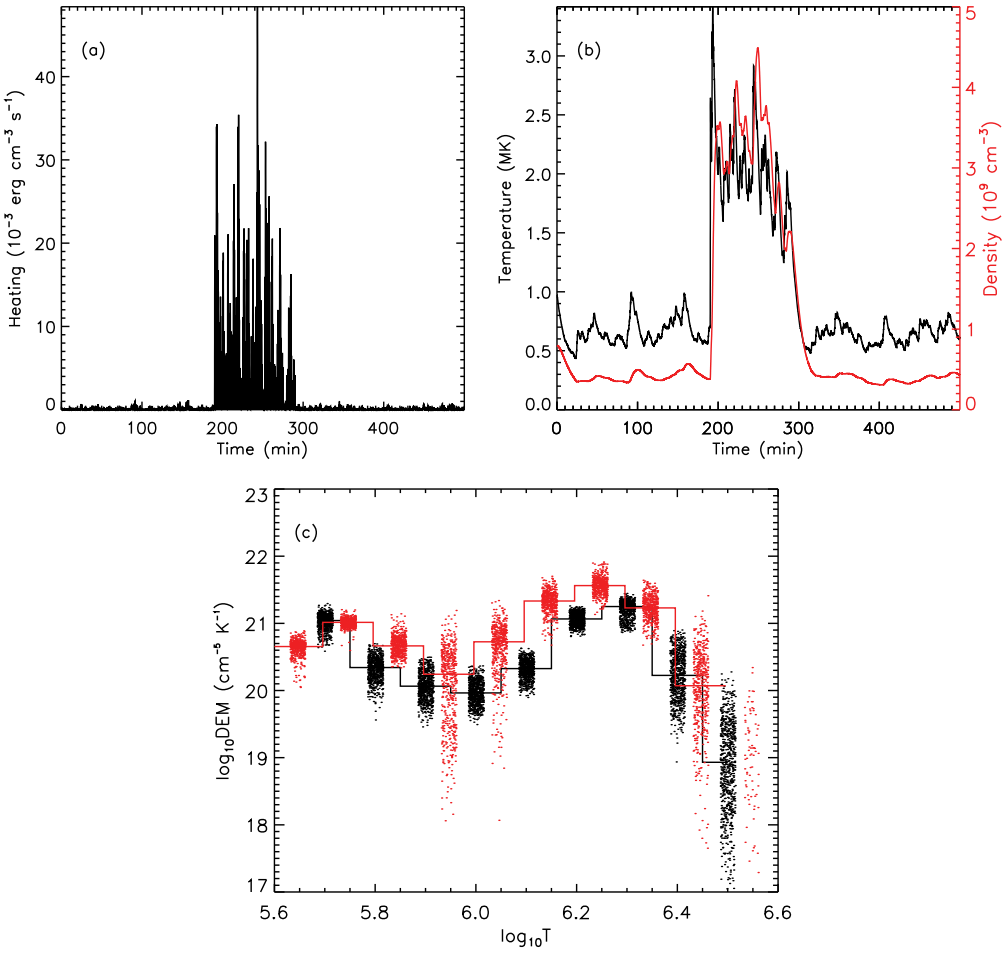

Figure 4.12: Alternative version of case 3 in which, each strand receives high heating events 20% of its time, and low heating events the remaining time. (a) A sample heating profile is plotted. (b) Strand apex temperature (black, left axis) and strand density (red, right). (c) Same as the top panel of Figure 4.11.

The half-length and radius of a single strand are shown as thin solid, and dashed curves in Figure 4.5. The DEMs and T are plotted in Figure 4.13. The way we consider the volume expansion is that, each strand slowly expands for about 350 minutes and then the expansion saturates to a constant value. This constant value matches with the length, and radius of the strand chosen in all the cases. It is observed that for a slowly expanding loop, the adiabatic cooling effect can be negligible. There are two competing effects here. Under equilibrium conditions, the temperature of the loop increases with the length. In our slowly expanding loop, the cooling is compensated for with the length increase. But in reality, the rate of volume expansion can be entirely different, and more rapid than that we considered here. These effects become important when changes in the loop pressure and density due to expansion alone, and heating are comparable.

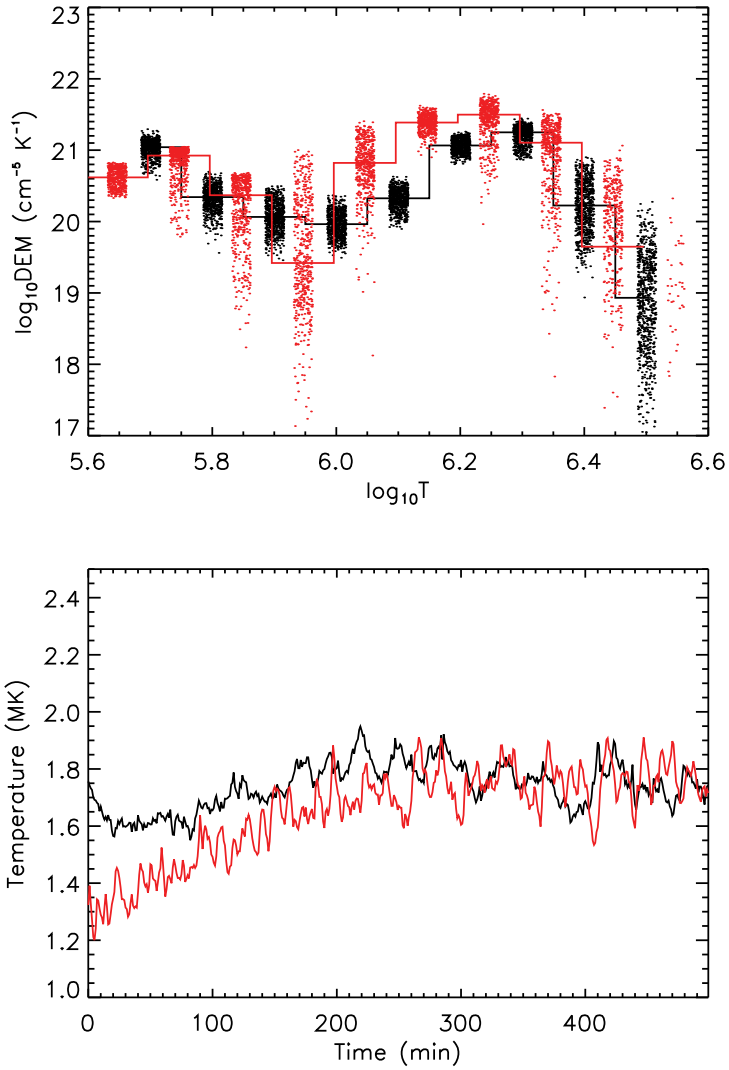

Figure 4.13: Hybrid heating model with expanding length and radius as shown in Figure 4.5 (thin solid and dashed curves, respectively). Both the length and radius of the loop vary slowly with time. In this case the temperature (red, lower panel) increases as the length of the loop increases.

4.3.5 Effects of Non-uniform Cross-section of the Loop

In the above EBTEL-based models, the emission is assumed to come from the coronal portion of the loop. EBTEL also predicts the emission from the transition region (TR) to model the lower temperatures. However, the predicted TR emission is strong and rather flat relative to the corona. Inclusion of up to 5%–10% of the TR emission will not affect the results, but adding more contribution from the TR requires stronger heating to match the observed emission-weighted temperature. This results in a strong emission from the higher temperature, which is not observed.

One possible reason for the strong TR DEMs produced by EBTEL is that the model assumes a constant cross-section over the length of the loop, whereas the loops on the

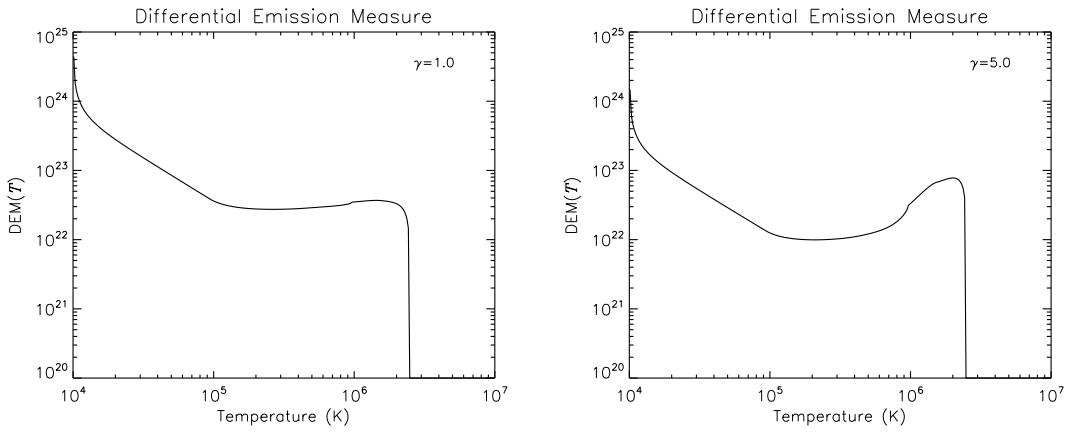

Figure 4.14: Results from a simple loop model assuming steady heating. Left panel: DEM of a loop with expansion factor (γ) = 1. Note the flat DEM in the range of $10^5 < T$(K)$< 10^6$. Right panel: Same as the left panel, but with $\gamma = 5$. The DEM now shows a clear peak at $T \approx 2$ MK.

Sun have significant expansion factors (γ) between the loop footpoints in the TR and the loop top in the corona. Potential field modeling of active regions (e.g., Asgari-Targhi & van Ballegooijen, 2012) indicates $\gamma = 3$–30, depending on height, and similar expansion factors may occur on the quiet Sun. When the cross-sectional area A of a loop increases with height, the volume of plasma at coronal temperatures is increased relative to that at TR temperatures, so the slope of the DEM(T) curve becomes steeper and more consistent with observations.

To demonstrate this effect, we developed a simple loop model for the case that the cross-section A varies along the loop. The heating is assumed to be steady in time. The model is described in Appendix C. It allows us to compute the DEM(T) for a single loop with a given expansion factor γ, half-length L, and peak temperature $T_{\rm max}$ (we use $L = 9$ Mm). We repeat the calculation for different peak temperatures ($6.0 < \log_{10} T_{\rm max} < 6.4$) and compute the average DEM(T). In Figure 4.14, we plot the DEM results for $\gamma = 1$ (left panel) and $\gamma = 5$ (right panel). Note that for a loop with uniform cross-section ($\gamma = 1$), DEM(T) is flat for $T > 10^5$ K, similar to the DEMs predicted with the EBTEL code (see Klimchuk et al., 2008). In contrast, for $\gamma = 5$ the peak value of the DEM in the corona is about eight times its value in the TR, similar to the observed DEMs (see Figure 4.2). These results suggest that the overall shape of the observed DEM can be very well reproduced with a collection of hot loops ($T_{\rm max} > 1$ MK) that have significant expansion factors ($\gamma \sim 5$–10). However, the peak value of the DEM as predicted by the model is larger than the observed value by a factor of about 100. Therefore, the loops must fill only a small fraction of the coronal volume (filling factor ~ 1 %).

4.4 SUMMARY AND DISCUSSION

Using the high temporal cadence observations from the HMI and AIA instruments on board *SDO*, we studied the cases of emerging bipolar regions in the quiet Sun. High-cadence data from AIA including six EUV channels are re-sampled to 1 minute data to improve the signal-to-noise ratio as well as to have a good temporal resolution. Further, `xrt_dem_iterative2.pro` is used to construct DEMs near the loop top in a $6'' \times 6''$ pixel region (Section 4.2, Figure 4.2). From these DEMs, we get the temporal evolution of emission-weighted temperature with Equation (4.2).

Integrated unsigned magnetic flux derived from the HMI observations[6] is compared with the temperature of the loop for a sample of four bipoles (Figure 4.3). There is no clear relation between the two quantities, suggesting that for these small emerging bipoles, the surrounding regions in photosphere and higher atmosphere play an important role in the loop evolution.

To estimate the energetics involved in the formation of these loops, we use a hydrodynamic loop model (EBTEL) to simulate the DEMs and emission-weighted temperatures. We assume that a loop is a bundle of 100 strands, each having a length of about 18 Mm, and a uniform radius of 0.1 Mm. Furthermore, each strand is randomly heated and the average effect describes the properties of the observed loop. To this end, we tested three simple heating events with varied heating frequencies as described in Sections 4.3.1–4.3.4. The average heat flux in our study ($\approx 10^6$ erg cm^{-2} s^{-1}) is in close agreement with the approximate energy losses observed in the quiet Sun. The 3σ values of the fluctuations in $T_{\rm DEM}$ (MK) are about 0.25, 0.16, 0.55, and 0.24 for the observations, cases 1, 2, and 3(a), respectively.

In case 3, we tested the following sub-cases: (a) 20% of the strands are heated to high heating values all the time, and the remaining strands are heated to low heating values (Section 4.3.3); (b) all strands are heated to high heating values 20% of their time (Section 4.3.3); and (c) same as case 3(a), but for expanding strands to account for the adiabatic cooling effects (Section 4.3.4). It is shown that cases 3(a) and (b) are equivalent and match the observations fairly well. This suggests that there may be a range of heating events operating in the loops at a given time. In cases 2 and 3(b), though there are only a few large heating events, the essential difference between the two cases is that, unlike in case 2, the duration of a single high heating phase in case 3(b) itself is longer compared to typical plasma cooling time (making case 3(b) statistically a steady heating model). This allows case 3(b) to find a DEM peak at higher temperatures. The model described in case 3 is the best model we could obtain with the scope of the present work. Mixing low and medium frequency heating at various proportions with different average heating rates shows discrepancy, and does not fit observations

[6] which is in the range of $10^{19} - 10^{20}$ Mx

completely. These results are based on the assumption that the emitting plasma has coronal origin.

Alternatively, we also argued that to include TR emission in the model, it is important to consider an expansion of the loop from TR to corona. In this scenario, a steady heating model for loops with loop apex temperature $> 10^6$ K can well reproduce the observed DEMs, assuming $\sim$1% plasma filling factor.

Reliability of AIA DEMs is a matter of debate. O'Dwyer et al. (2010) studied the contribution of spectral lines and continuum emission to the AIA EUV channels using CHIANTI atomic database. They emphasize that the contribution of particular spectral lines and continuum emission can affect the interpretation of the observed features, when AIA channels are used to observe regions other than those for which the channels were designed[7]. Del Zanna et al. (2011) compared AIA DEMs with the *Hinode*/EIS observations of active regions. They found discrepancies between the derived DEMs. This is mainly due to the multi-thermal nature of AIA response curves, which have contributions from cooler components. The cooler emission below 6.0 (in log T), seen in our observations could be due to the double-peaked nature of AIA responses as suggested by Del Zanna et al. (2011). Empirically modified filter response curves for AIA are derived to address some of these issues; however, the role of this possible contamination in a already cool loop (like the one originating from a small bipole in the quiet Sun), as compared to the warm loops in the hotter active region, has to be further examined.

The models presented in this work assume that the strands are heated uniformly over their entire length. Alternatively, the strand can be heated in a non-uniform manner with localized and concentrated heat sources. If the heating is concentrated at the loop footpoints, this may lead to the loss of equilibrium in the energy balancing terms, as the radiative losses in the coronal section dominate the downward conductive flux. This will trigger the runaway cooling due to strong radiative losses and a condensation is formed in the coronal loops (for example, Hood & Priest, 1980; Müller et al., 2004). This is a well-studied phenomenon in the formation of solar prominences (Antiochos & Klimchuk, 1991; Antiochos et al., 1999). Recently, based upon the observed properties of the hot, and warm loops in active regions, Klimchuk et al. (2010) have argued that the high concentration of heating low in the corona, and the steady or quasi-steady heating models (leading to thermal nonequilibrium) can be ruled out. However, Peter et al. (2012) claim that a steady supply of energy is required even in the events of condensation in the corona to keep the coronal pressure. They also suggested that thermal non-equilibrium can be a valuable tool in investigating the plasma dynamics and heat input in the regions where condensation forms.

The studies on the role and importance of the thermal non-equilibrium in the formation of condensation in the short quiet-Sun loops are not extensive. Müller et al. (2003,

[7] `http://aia.lmsal.com/public/CSR.htm`

2004) discussed in detail the numerical simulations of condensation and catastrophic cooling of short TR 10 Mm loops, and longer 100 Mm coronal loops, respectively. They considered heating that has exponential height dependence along the loop, and further suggested that the catastrophic cooling is initiated by the loss of equilibrium at the loop apex due to concentration of heating at the footpoints, but not due to a drastic decrease of the total loop heating.

Note that the strands in a loop may interact in a very complex manner, and their response to the condensation is the key objective to be addressed. Further work is necessary to get a better picture of the nature and location of the heating, observational signatures of condensation, and finally the role of magnetic field in this whole process. A complete set of answers for these questions is still elusive and we need more observational constraints to narrow down the possibilities.

Chapter 5

ROLE OF THE MAGNETIC CARPET IN THE HEATING OF QUIET SOLAR CORONA*

5.1 INTRODUCTION

The dynamical evolution of magnetic field in the solar photosphere holds the key to solving the problem of coronal heating. High resolution observations show that a mixed polarity field, termed as the magnetic carpet (Schrijver et al., 1997), is spread throughout the solar surface. The loops connecting these elements pierce through the atmosphere before closing down at the photosphere. The random motions of these small elements caused by relentless convective motions in the photosphere, are a favorite candidate to explain the energy balance in the solar atmosphere (for example, Schrijver et al., 1998; Gudiksen & Nordlund, 2002; Priest et al., 2002). In three-dimensional (3D) magnetohydrodynamic (MHD) models, small-scale footpoint motions drive dissipative Alfvén wave turbulence in coronal loops (van Ballegooijen et al., 2011). Also, the convective motions promote magnetic reconnection and flux cancellation—viable mechanisms to heat the corona[2] (for example, Longcope & Kankelborg, 1999; Galsgaard & Parnell, 2005).

The magnetic carpet typically contains magnetic features with magnetic flux ranging from $10^{16} - 10^{19}$ Mx, a part of which are kilo Gauss flux tubes, also present in the internetwork (Lagg et al., 2010). The carpet is continually recycled with newly emerging flux replacing the pre-existing flux. Magnetic elements split, merge, and cancel due to granular action (Iida et al., 2012; Yang et al., 2012; Lamb et al., 2013). Additionally, recent observations show small-scale swirl events in the chromosphere, possibly

*The contents of this chapter are published in Chitta et al. (2014)

[2]The evolution of the magnetic carpet is also studied in the context of acceleration of slow and fast solar wind (Cranmer & van Ballegooijen, 2010; Cranmer et al., 2013).

due to the rotation of photospheric elements (Wedemeyer-Böhm & Rouppe van der Voort, 2009). Also, the magnetic elements display significant horizontal motions that can reach supersonic speeds (e.g. Jafarzadeh et al., 2013). All these dynamical aspects of the magnetic carpet make the overlying field non-potential—a source of magnetic energy (for a review on small-scale magnetic fields see de Wijn et al., 2009). There is indirect observational evidence for the existence of non-potential structures in the quiet Sun (Chesny et al., 2013).

The vector magnetic field ($\mathbf{B}$) or its line-of-sight component (B_z) at the photosphere is used to infer coronal fields, due to the unavailability of their direct measurements in corona. Earlier studies of the co-evolution of magnetic carpet and coronal field were mainly through the potential field (current-free) extrapolations of the photospheric magnetic field (for example, Close et al., 2004; Schrijver & van Ballegooijen, 2005). Recently, Meyer et al. (2013) have used nonlinear force-free field extrapolations of the observed B_z to study the magnetic energy storage and dissipation in the quiet Sun corona. They concluded that the magnetic free energy stored in the coronal field is sufficient to explain structures like X-ray bright points (XBP) and other impulsive events at small-scales (for reviews on the force-free magnetic fields see Schrijver et al., 2006; Metcalf et al., 2008; Wiegelmann & Sakurai, 2012). Wiegelmann et al. (2013) have used a 22 minute time sequence of very high resolution vector magnetograms to extrapolate the field into the upper atmosphere under the potential field assumption, and argued that the energy release through magnetic-reconnection is not likely to be the primary contributor to the heating of solar chromosphere and corona in the quiet Sun. To test the basis of magnetic-reconnection between open and closed flux tubes as a plasma injection mechanism into the solar wind, Cranmer & van Ballegooijen (2010) used Monte Carlo simulations of the magnetic carpet. They also concluded that the slow or fast solar wind is unlikely to be driven by loop-opening processes through reconnections. The works of Cranmer & van Ballegooijen (2010) (using models to study solar wind acceleration), and Wiegelmann et al. (2013) (using observations to study solar atmospheric heating) arrive at similar conclusions, disfavoring a significant role of the evolution of the magnetic carpet in supplying energy to the corona and solar wind, in contrast to Meyer et al. (2013).

A possible explanation for the above conflicting results is that the potential field studies simplify the magnetic topology and do not include dynamic aspects like currents, and other nonlinear effects. Also, as the methods of analysis are not the same, it may not be so straightforward to compare the results from those studies. With an ever increasing quality of the observations showing more intermittent flux filling the solar surface, it is valid to inquire its contribution to the dynamics of the upper solar atmosphere and advance our knowledge towards a holistic picture of the magnetic connection from photosphere to corona, particularly in the quiet Sun.

To rigorously address these issues, a continuous monitoring of the Sun's magnetic field is desired. This valuable facility is provided by the Helioseismic and Magnetic Imager (HMI; Scherrer et al., 2012) on board the *Solar Dynamics Observatory* (*SDO*; Pesnell et al., 2012). *SDO*/HMI obtains full-disk magnetograms of the Sun at $0''.5$ pixel^{-1} with 45 s cadence. To probe the magnetic field at an even higher spatial resolution, the Imaging Magnetograph eXperiment (IMaX; Martínez Pillet et al., 2011) instrument on the *Sunrise* balloon-borne observatory (Solanki et al., 2010; Barthol et al., 2011) recorded 33 s cadence observations at $0''.055$ pixel^{-1}. To better understand the role of the magnetic carpet, we use the *SDO*/HMI and the *Sunrise*/IMaX line-of-sight (LOS) magnetic field observations as lower boundary conditions in a time-dependent nonlinear force-free modeling of the coronal field, and report our comparative findings. The rest of the chapter is structured as follows. In Section 5.2, we describe the datasets and model set-up. In Section 5.3, the main results of the work are presented. We conclude in Section 5.4 with a summary, and implications of the results are discussed.

5.2 OBSERVATIONS AND MODEL SET-UP

In this work, we used a one day long time sequence of the *SDO*/HMI LOS magnetic field observations at the disk center and compared the results with the higher resolution observations at the disk center obtained from the *Sunrise*/IMaX instrument. In Section 5.2.1, we briefly describe the datasets, and Section 5.2.2 deals with the set-up of the simulation for the magnetic field extrapolations.

5.2.1 Dataset

HMI Data (Set 1): This set consists of a tracked, one day long, time sequence of the LOS magnetograms observed at the disk center on 2011 January 08, starting at 00:00 UT. With a field-of-view (FOV) of 187×187 Mm^2, and a time cadence of 45 s, these observations cover several magnetic network patches in the quiet Sun. In Figure 5.1(a) we show a snapshot from the HMI observations. The magnetic flux density is saturated at 50 G. The observations are found to be closely in flux balance over the entire duration. To retain the weaker field at the lower boundary, no smoothing is applied to the data. The larger region considered here allows us to compare various results between subregions with varied magnetic configurations. The details are given in Section 5.3.

IMaX Data (Set 2): These level 2 data correspond to imaging spectropolarimetric observations of Fe I at 5250.2 Å. The observations were recorded at the disk center on 2009 June 09, starting at 01:30 UT. The spatial resolution of these observations is ten times better than the HMI sequence. On the downside, IMaX observations span over time period of only ≈ 30 minutes. From the original frames, the degraded edges

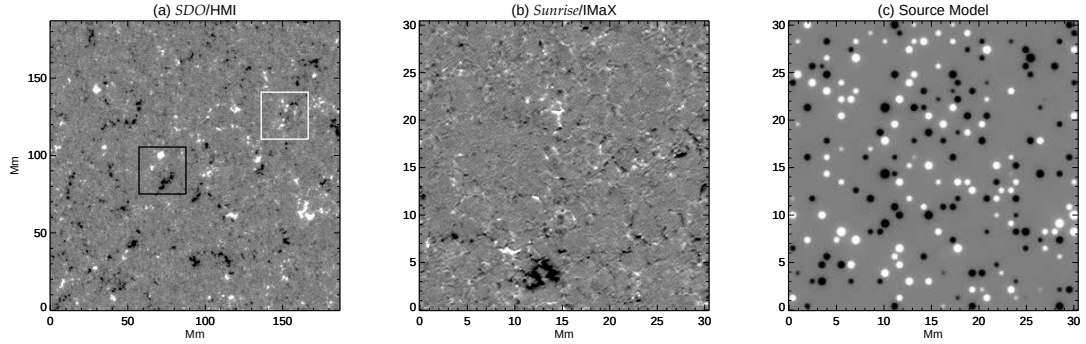

Figure 5.1: Contextual figure showing the photospheric line-of-sight (LOS) magnetograms taken from the respective time sequences. (a) *SDO*/HMI. (b) *Sunrise*/IMaX. (c) Model magnetogram from the magnetic sources (see text for details). Note the larger field of view (FOV) of *SDO*/HMI compared to the *Sunrise*/IMaX, and Source Model. A white box shown in panel (a) is approximately the size of FOVs in panels (b), and (c). A black box shown in panel (a) marks an ephemeral region. To facilitate displaying, all the magnetograms are saturated at ± 50 G.

because of the apodization (required by the phase diversity restoration technique) during the reduction process, have been discarded. We extracted a 30×30 Mm^2 region for further analysis. The LOS magnetograms are derived by taking the ratio of Stokes V and I with a calibration constant (c.f. eq. 17 in Martínez Pillet et al., 2011). The data are binned to a pixel scale of 119.2 km (Figure 5.1(b)). This effectively reduces the noise in the data by up to a factor of three (but it also reduces signal due to small-scale mixed polarity fields). Similar to the HMI data, IMaX data are also found to be closely in flux balance. Due to the limitations of the time duration of the dataset, the evolution of the coronal magnetic field cannot be studied for a longer period. For this purpose, we have constructed a series of artificial LOS magnetograms, named, Source Model. The details of the Source Model are given below.

Source Model (Set 3): The Source Model is made to complement the IMaX observations, but for a longer duration of time (see Appendix D for details). The model is initiated with 50 magnetic sources placed randomly on a mesh of hexagonal grids (which has the dimensions of IMaX FOV considered above). The mesh is periodic in x-, and y-directions. The sources include both positive and negative polarity elements such that the net flux is zero. The sources are allowed to move along the edges of each hexagonal grid which has a length unit of ≈ 1 Mm. All the sources move with a uniform random velocity of 1.5 km s^{-1}, which is in the range of typical observed velocities of the small scale magnetic elements due to the interactions with granules (for e.g. Chitta et al., 2012b, and references therein).

During the time evolution, the flux emergence, cancellation, along with splitting

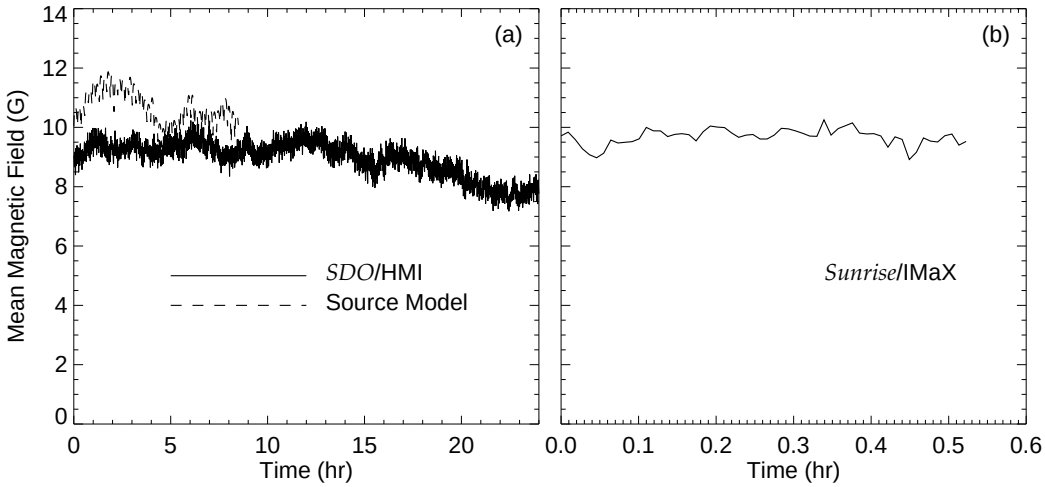

Figure 5.2: Mean magnetic field as a function of time for the three magnetogram types. (a) *SDO*/HMI (solid line, the mean magnetic field is derived from a region marked with the white box in Figure 5.1(a)), Source Model (dashed line). (b) *Sunrise*/IMaX. The y-axis scaling for both panels is the same.

and merging of the elements are the possible ways of interactions among the magnetic elements at the corners of each grid. The LOS magnetic field reached a quasi-statistical equilibrium almost 15 hours after the initiation. During this time, the total magnetic flux increased from 10^{19} Mx to 10^{20} Mx. Out of the total 48 hours of time evolution, which includes both the rise time and equilibrium period, a portion of 8.5 hours time sequence is used for further analysis. In Figure 5.1(c) we show a snapshot of the LOS magnetogram from the Source Model.

To ensure $\nabla \cdot \mathbf{B} = 0$, fractional flux imbalance in the observed data (HMI and IMaX) is corrected by dividing the positive flux with an absolute ratio of integrated positive flux to the negative flux in the FOV. This method is justified only if the ratio is close to unity to begin with, in other words, the observations must be closely in flux balance. This is the case in both the observations we used in this study. In Figure 5.2 we plot the mean magnetic field ($\langle |B_z| \rangle$) as a function of time for all the datasets. In the left panel the solid line is for the HMI set and dashed line is for the Source Model. Right panel shows the IMaX mean magnetic field. We emphasize that the IMaX LOS magnetic field is derived from a simple ratio method, which underestimates the flux density in stronger elements (Martínez Pillet et al., 2011).

5.2.2 Simulation Set-up

In this section, we describe the simulation set-up and the equations we solve to derive the 3D magnetic field above the photosphere.

For Set 1, the computational box is a $512 \times 512 \times 250$ cell volume covering $187 \times 187 \times 91.4$ Mm^3 in physical space. For Sets 2 and 3, the computational domain is much smaller covering only $30.5 \times 30.5 \times 18$ Mm^3 with $256 \times 256 \times 150$ cells. The simulation box is periodic in x- and y-directions and closed at the top. LOS magnetograms of Sets 1, 2, and 3 are the respective boundary conditions in the xy-plane at $z = 0$. Initially, at time $t = 0$, a potential field is assumed to fill the box, which is then evolved in time into nonlinear force-free states with the evolving boundary conditions.

The rate of change of vector potential $\mathbf{A}$ is related to the magnetic field $\mathbf{B}$ through the induction equation

$$\frac{\partial \mathbf{A}}{\partial t} = \mathbf{v} \times \mathbf{B} + \epsilon, \tag{5.1}$$

where ϵ is the hyperdiffusion, defined as

$$\epsilon = \frac{\mathbf{B}}{B^2} \nabla \cdot (\eta_4 B^2 \nabla \alpha). \tag{5.2}$$

$\alpha = \mathbf{j} \cdot \mathbf{B}/B^2$ is the force-free parameter, and η_4 is the hyperdiffusivity. van Ballegooijen & Cranmer (2008) presented a theory of coronal heating which draws energy with hyperdiffusion from the dissipation of nonpotential magnetic field. It conserves the mean magnetic helicity and smooths the gradients in α (Boozer, 1986; Bhattacharjee & Hameiri, 1986). It has been proposed that tearing modes can promote turbulence in 3D sheared magnetic field, which causes hyperdiffusion (Strauss, 1988).

Table 5.1: Values of η_4 and ν^{-1} used in the magnetic modeling

	η_4 (km^4 s^{-1})	ν^{-1} (km^2 s^{-1})
HMI	1.05×10^7	1×10^3
IMaX	6.48×10^6	0.6×10^3
Source Model	1.57×10^6	0.1×10^3

Equation 5.1 is evolved using a magneto-frictional relaxation technique (Yang et al., 1986), which assumes that the plasma velocity ($\mathbf{v}$, in this case, the magneto-frictional velocity) is proportional to the Lorentz force ($\mathbf{j} \times \mathbf{B}$), given by

$$\mathbf{v} = \frac{1}{\nu} \frac{\mathbf{j} \times \mathbf{B}}{B^2}, \tag{5.3}$$

where ν is the frictional coefficient. The numerical values of η_4 and ν^{-1} (tabulated in Table 5.1) are determined in part by the requirement of numerical stability of the code, and by the length and time units of the simulations. The results presented in Section 5.3 are quantitatively stable about the chosen values of η_4 and ν^{-1}. Mackay et al. (2011) and Cheung & DeRosa (2012) used magneto-frictional relaxation technique to study the time evolution of active regions on much larger scales.

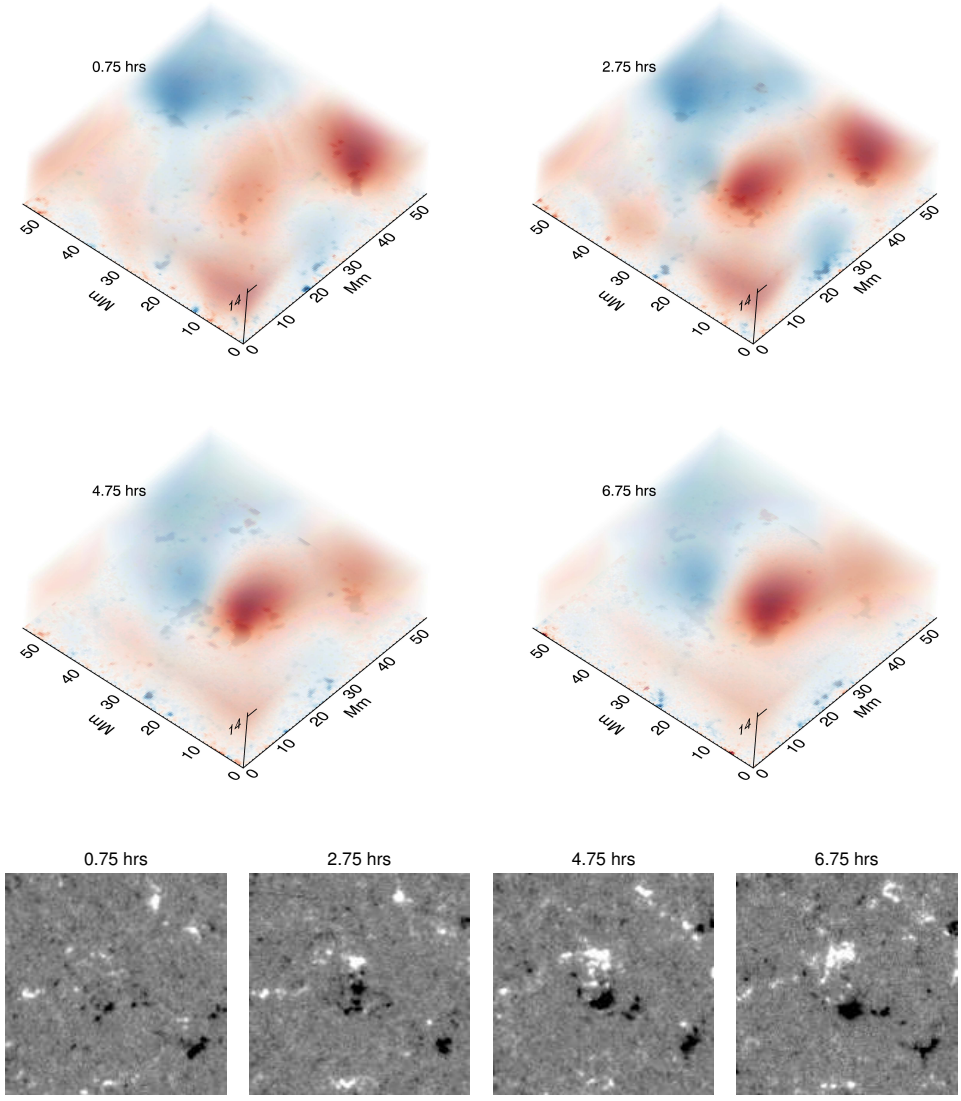

Figure 5.3: Top: volume rendering of the extrapolated B_z using *SDO*/HMI observations as lower boundary conditions. Shown here is the time evolution of B_z of an ephemeral region, with consecutive frames lying two hours apart, in a box of $\approx 55 \times 55 \times 14$ Mm^3 volume, with its bottom surface centered at (70 Mm, 90 Mm) of Figure 5.1(a). The red (blue) colored areas are the regions of negative (positive) polarity. Bottom: the distribution of B_z (saturated at ± 50 G) in the photosphere corresponding to the respective panels in the top segment is shown.

It is known that the magnetic field in the photosphere is non-force-free due to the high plasma β. Metcalf et al. (1995) calculated the Lorentz force of an active region as a function of height. They concluded that the field becomes force-free higher in the atmosphere, above approximately 400 km. The mixed polarity fields in the magnetic carpet are weaker and may be dominated by gas pressure even in the chromosphere as suggested by the simulations of Abbett (2007), which, however, do not include a realistic treatment of radiative transfer for the photospheric and chromospheric layers. To mimic these additional forces on the magnetic field in the chromosphere, we add a constant vertical flow (v_1) at the lower boundary up to a height of 0.7 Mm (c.f. Eq (1), Metcalf et al., 2008). $\mathbf{v}$ is modified accordingly, and is given by

$$\mathbf{v} = (\frac{1}{\nu}\mathbf{j} - v_1\hat{z} \times \mathbf{B}) \times \mathbf{B}/B^2. \tag{5.4}$$

This new force marginally prevents the field from splaying out at the lower boundary. In the present work we use $v_1 = 1.5$ km s^{-1} for IMaX/Source Model, and $v_1 = 3.4$ km s^{-1} for HMI dataset. This has only a minor effect on the flux concentrations in our model. Similar to η_4 and ν^{-1}, the choice of v_1 is defined by the length and times units of the respective models.

5.3 RESULTS

In the top segment of Figure 5.3, we present volume rendering of B_z in a sub-volume from HMI simulations at four instances, separated by two hours each. At the lower boundary of this sub-volume, an emerging bipole is seen, with stronger negative polarity (centered on the black square, Figure 5.1(a)). The red (blue) coloration covers regions of negative (positive) polarity. As the bipole emerges into the atmosphere, pre-existing coronal field responds to it, and eventually becomes bipolar in time. Note that this is a 3D rendering. To *see through* the cube, we used increasing transparency of layers with height (so that we can see till the bottom through the layers above). Also, to account for the decrease in field strength with height, we scaled each layer (at a given height) in respective panels separately. In the bottom segment, we show B_z at photospheric level corresponding to the respective panels in the top segment. The purpose of this figure is to show how the coronal field responds to an emerging bipole in the photosphere.

The magnetic free energy ($E_{\rm free}$), which is an excess of non-potential magnetic energy (in this case, the nonlinear force-free energy) over the potential magnetic energy is calculated. Our aim is to emphasize the height dependence of the quantities relevant to the energy budget of the solar corona. To this end, we calculate $E_{\rm free}$ as a function of

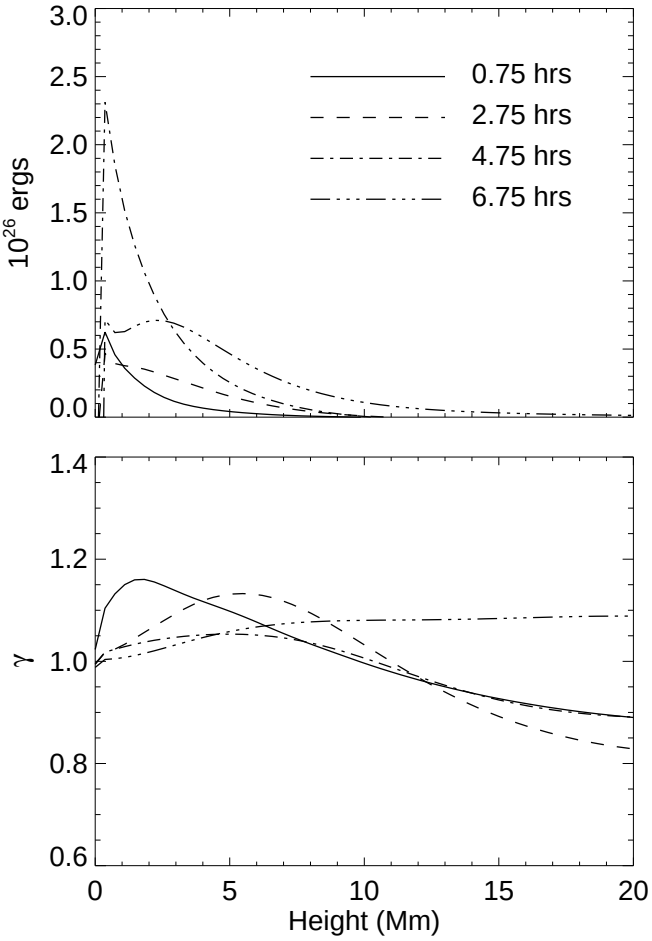

Figure 5.4: Top panel: Free energy of an emerging bipole located within the black square in Figure 5.1(a). Each of the four curves plotted in a different line style is for a different point in time, corresponding to the times of the snapshots plotted in Figure 5.3. The curves are labelled in the upper panel. At all times $E_{\rm free}(z)$ falls rapidly with z, peaking below 5 Mm. Bottom panel: The ratio of non-potential magnetic energy to the potential magnetic energy (γ) is plotted as a function of height (for the same time steps as shown in the top panel). The peaks of $\gamma(z)$ shift towards higher z with time, indicating the interaction of newly emerging field with the pre-existing coronal field.

height, given by

$$E_{\text{free}}(z) = \frac{1}{8\pi}\Delta z \int\int [B^2_{\text{np}}(x,y,z) - B^2_{\text{p}}(x,y,z)]dxdy, \tag{5.5}$$

where Δz is the pixel length. $B^2_{\text{np}}/8\pi$ and $B^2_{\text{p}}/8\pi$ are the non-potential, and potential magnetic energy densities, respectively. In the top panel of Figure 5.4 we plot the HMI $E_{\text{free}}(z)$ ($\Delta z = 0.36$ Mm). Integration is over the surface enclosed by the black square in Figure 5.1(a). The curves represent the evolution of an emerging bipole at four different epochs (shown in Figure 5.3). It is observed that most of $E_{\text{free}}(z)$ (5–10$\times 10^{25}$ ergs), is available at heights below 5 Mm. These results are consistent with the free energy values reported in Meyer et al. (2013).

To estimate the non-potentiality of the magnetic energy, we calculate a ratio $\gamma(z)$, defined as

$$\gamma(z) = \frac{\int\int B^2_{\text{np}}(x,y,z)dxdy}{\int\int B^2_{\text{p}}(x,y,z)dxdy}. \tag{5.6}$$

It is observed that the magnetic energy is close to energy of the potential magnetic field, with an excess $< 20\%$. In the bottom panel of Figure 5.4 we plot $\gamma(z)$ for the same epochs as shown in the top panel. There is an apparent rise in the non-potentiality with time, indicating the interaction of a newly emerging flux with the pre-existing coronal field. However, by combining the values of $\gamma(z)$ and $E_{\text{free}}(z)$, it can be seen that the coronal field over the HMI FOV is potential. We note that in the bottom panel, $\gamma(z) < 1$ for some points in time above a height of 10 Mm, which means a *negative* free energy. This is due to the fact that the surface integration is performed only over a sub-region within the full FOV. The total volume integrated E_{free}, however, remains positive.

Magnetic free energy is necessary but not sufficient to completely quantify the energy supply to solar corona. It is important to calculate the energy dissipation, and energy flux, which can then be directly compared with the observed radiative and conductive losses. Earlier studies by Withbroe & Noyes (1977), Withbroe (1988), Habbal & Grace (1991) placed observational constraints on the energy flux through the coronal base, 10^5–10^6 erg cm^{-2} s^{-1} for a quiet Sun region. With magneto-frictional relaxation including hyperdiffusion, the energy dissipation per unit volume (Q) is calculated as

$$Q = \frac{B^2}{4\pi}(\nu|\mathbf{v}|^2 + \eta_4|\nabla\alpha|^2), \tag{5.7}$$

(see, Yang et al., 1986; van Ballegooijen & Cranmer, 2008). The first and second parts on the right hand side of the Equation 5.7 are due to magneto-friction, and hyperdiffusion, respectively. To understand the evolution of Q with respect to height, at the time scale of minutes, we consider snapshots of Q from HMI simulations, separated by 15 minutes. The results are shown in Figure 5.5. The top row shows B_z (lower boundary,

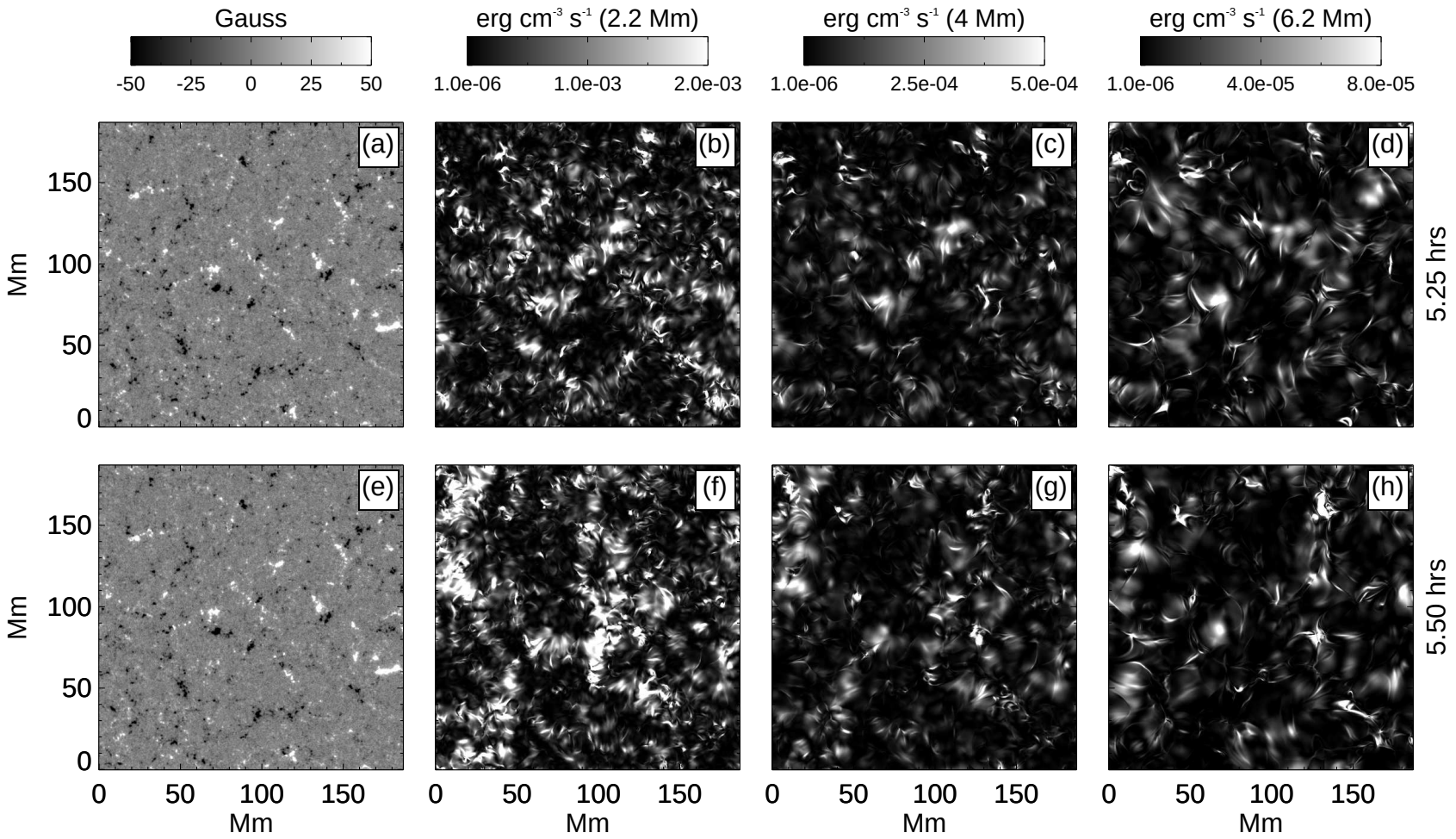

Figure 5.5: HMI Magnetic field configuration at the lower boundary ((a) and (e) saturated at ± 50 G), and the energy dissipation (Q) at three layers ((b) and (f) 2.2 Mm; (c) and (g) 4 Mm; (d) and (h) 6.2 Mm) are shown. Note the change of grey scale ranges in the energy dissipation maps. The top and the bottom maps are separated by 15 minutes in time and are rendered according to the same greyscales (for a given height). Though the magnetic field configuration has little apparent change, the locations of the energy dissipation have changed significantly, suggesting a highly *non-localized* and intermittent nature of the time evolution of magneto-frictional relaxation method.

(a)), and Q at three heights ((b): 2.2 Mm, (c): 4 Mm, and (d): 6.2 Mm) at 5.25 hrs into the simulation. Bottom row is same as the top row, but 15 minutes after panels (a)-(d). With very little change in the B_z over the duration, apparently, there is a drastic morphological change in Q (panels (b) and (f)). This is very interesting to note, suggesting that the energy dissipation process due to magneto-friction and hyperdiffusion is *non-localized* in time (i.e., the locations of energy dissipation rapidly change with time). This in turn means that the time evolution of spatially averaged Q at any two locations separated by some distance (having a different underlying magnetic morphology) would be similar. In other words, the average dissipation of magnetic energy is very uniform in our simulations. However, the magnitude of Q has a strong height dependence (as seen in the greyscales of the right three panels). This was also indicated by Meyer et al. (2013). These large-scale changes in the atmosphere are caused by small-scale random footpoint motions of magnetic elements at the photosphere.

To further quantify the above statements, Figure 5.6 plots the horizontally averaged dissipation rate as a function of height and time. The top left panel is Q plotted as a function of height from the HMI simulations. The two shaded bands are for two sub-regions of the HMI FOV (red: Figure 5.1(a) black square; blue Figure 5.1(a) white square). The black square covers an ephemeral region (ER), and the white square covers a *less active* quiet region (QR). At a given height, the width of each shaded band represent the range of minimum to maximum energy dissipated at that height. A vertical shaded rectangle is drawn to indicate the base of the transition region and corona. Q monotonically decreases with height in a similar way for regions with completely different underlying B_z. In the top right panel, results from the Source Model (red), and IMaX (blue) are shown for comparison with those of HMI. It is noted that the fall of $Q_{\text{Source Model/IMaX}}$ is steeper than Q_{HMI}.

Further, we plot the averaged Q in two height ranges (0–2; 2–4 Mm) and study its time evolution. In Figure 5.6(c) we plot these results for the HMI simulations (red: ER; blue: QR; solid: 0–2 Mm; dashed: 2–4 Mm). These plots show that on average, the energy dissipation is uniform over the entire FOV and also fairly constant throughout the time evolution. Another fact to notice is that Q reaches its statistically mean value very early in the simulations. Recalling that the initial condition of the simulation is a potential field, the build-up of magnetic shear of coronal field and in turn the energy dissipation through hyperdiffusion, is contributing only a fraction of total Q. Magneto-friction acts as a dominant energy source in our simulations. Figure 5.6(d) shows the evolution of $Q_{\text{Source Model}}$.

As a next step, we calculate the energy flux (F) through a given horizontal surface. In a quasi-stationary state, the energy flux $F(z)$ through height z is equal to the integral

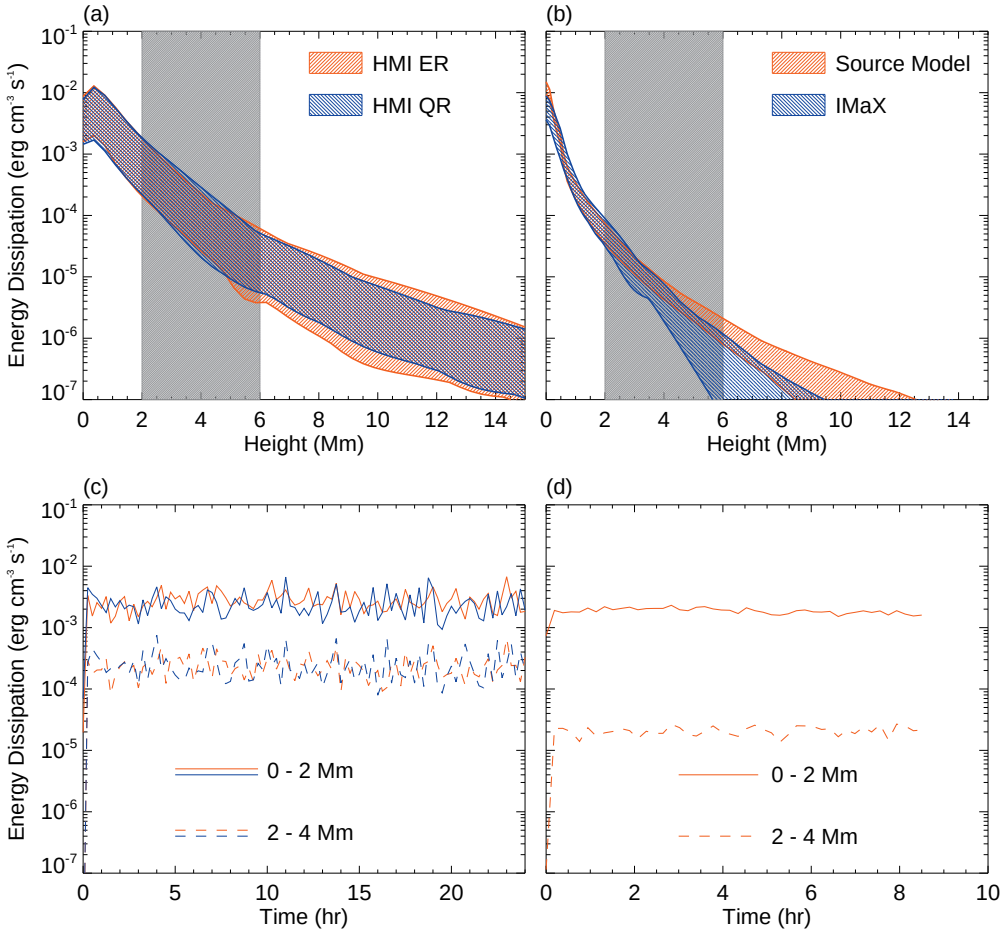

Figure 5.6: Horizontal mean of energy dissipation plotted as a function of height (top panels), and time (bottom panels). (a) Mean energy dissipation over an ER (red), and a QR (blue) observed by HMI. (b) Energy dissipation in the IMaX dataset (blue) and Source Model (red) averaged over the entire FOV. As an illustration, a grey striped box is drawn at 2–6 Mm range to compare the energy dissipations between panels (a), and (b) at those heights. (c) Mean energy dissipation plotted vs. time, averaged over the height ranges 0–2 Mm (solid) and 2–4 Mm (dashed), respectively. (d) Same as (c), but for Source Model.

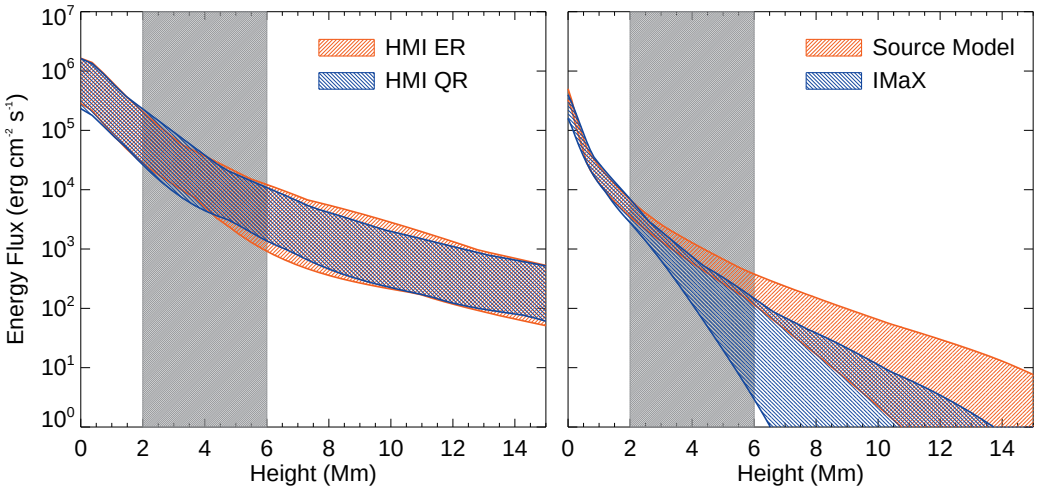

Figure 5.7: Horizontal mean of the energy flux plotted as function of height. The color schemes and legends in the left and right panels are the same as in Figures 5.6(a) and (b), respectively.

of $Q(z)$ over all heights above z, given by

$$F(z) = \int_{z}^{z_{max}} Q(z)dz, \tag{5.8}$$

where z_{max} is the top of the simulation domain. The horizontal average of the calculated $F(z)$ is plotted in Figure 5.7. Similar to Figure 5.6(a), in the left panel we show $\langle F(z)\rangle$ for two sub-regions within HMI FOV. $\langle F(z)\rangle$ of IMaX/Source Model are plotted in the right panel. All sets have a flux of $\approx 10^6$ erg cm^{-2} s^{-1} at the photosphere. Almost all of this flux is dissipated at heights below 2 Mm, i.e. in the chromosphere (for which, however, our model may not be valid, since the field below 1000–1500 km is not force-free). Over a quiet Sun, the coronal base is typically above 3 Mm (c.f. Figure 3, Withbroe & Noyes, 1977). At this layer, $\langle F(z)_{\rm HMI}\rangle \approx 5 \times 10^4$ erg cm^{-2} s^{-1}, and $\langle F(z)_{\rm IMaX}\rangle \approx 2 \times 10^3$ erg cm^{-2} s^{-1}. These values are lower than the required flux in the quiet Sun corona.

To summarize Figures 5.6 and 5.7, all the three sets of magnetograms used in this work show a similar trends. Close to the lower boundary both $Q(z)$, and $F(z)$, respectively, are similar for all the cases. $F(z)$ is $> 10^5$ erg cm^{-2} s^{-1}, and appears to be comparable with the coronal energy budget of the quiet Sun. This condition is no more satisfied for $z >$2–3 Mm. On average, there is an order of magnitude or more deficit in the required energy flux to support the observed coronal energy losses. The deficit in $F(z)$ is very noticeable in the higher resolution but smaller FOV IMaX/Source Model cases.

5.4 SUMMARY AND DISCUSSION

With an aim to understand the role of the magnetic carpet in the heating of the solar corona, we simulated the coronal magnetic field using the disk center observations of quiet Sun LOS magnetic field obtained from the *SDO*/HMI and *Sunrise*/IMaX. To overcome the limitations of short duration IMaX data, we created a time sequence of synthetic magnetograms that roughly match the IMaX set in terms of the absolute flux (Figures 5.1–5.2). A time series of the 3D nonlinear force-free magnetic field is constructed with the magnetograms as lower boundary conditions, and potential fields as initial conditions. The coronal field is evolved using Equation 5.1, with a magneto-frictional relaxation technique (Equation 5.4), including hyperdiffusion (Equation 5.2). We incorporated the non-force-free nature of the lower solar atmosphere (≤ 0.7 Mm) by adding vertical flows (constant and uniform) that prevent the field from splaying out at the lower boundary (Equation 5.4). These gentle flows weakly increased the field strength of the magnetic elements.

Next, we calculated $E_{\text{free}}(z)$, $Q(z)$, and $F(z)$ to quantitatively estimate the magnetic free energy, its dissipation, and energy flux injected at the base of corona. It is found that the energy dissipation in simulations with moderate resolution (HMI), and much higher resolution (IMaX/Source Model), is very similar close to the lower boundary. This suggests that mainly the low-lying loops originate from the mixed-polarity magnetic carpet. Also, the average length of these loops must be only a small fraction of the linear dimension of our computational domain. Further, these loops are highly intermittent, facilitating uniform energy dissipation over the entire surface. These loops can be formed by interactions of near-by elements (e.g. Wiegelmann et al., 2010), and also from the newly emerging flux in the internetwork (Centeno et al., 2007).

Despite their intrinsic differences, IMaX and Source Model simulations are strikingly similar. Moving away from the lower boundary, we see that $F_{\text{Source Model/IMaX}}$ decreases by more than two orders of magnitude at $z = 2$ Mm. This leaves only a few percent of F at the coronal base. Using a similar IMaX data, Wiegelmann et al. (2013) created a set of potential field models. They concluded that the magnetic energy release associated with reconnections is not likely to supply the required energy to heat the chromosphere and corona. Our energy estimates in this work are far lower than their estimated upper limit of the energy flux density due to magnetic-reconnections.

However, the deficit in F is smaller in the HMI set as compared to those of other models. Assuming that this discrepancy is mainly due to the larger HMI volume[3], it means that there is a contribution from the long range magnetic connections, often reaching coronal heights, that was not possible with the IMaX set. This was also cited

[3] $6.6\times$ more grid cells covering $192.4\times$ larger volume in physical space as compared to IMaX/Source Model volumes.

by Wiegelmann et al. (2013) as a reason for their too low upper limit. Future high spatial resolution observations simultaneously with large FOVs are required to check and justify the contribution from long range magnetic interactions. Also, IMaX and HMI observed mainly different kinds of features, with very different lifetimes. In the case of HMI it is predominantly network magnetic features (including ephemeral regions) and some internetwork fields, for IMaX it is dominated by internetwork fields. The latter are more likely to be horizontal and do not reach high into the atmosphere. Additionally, IMaX observations were carried out in 2009, at the depth of the last minimum in a very quiet part of the Sun, while the HMI data were obtained in 2011, i.e. when the Sun was well on its way into the new cycle.

A relatively large $F(z)_{\rm HMI}$ can be considered as a *basal* flux to heat a diffused coronal region. Compact features like XBPs have a mean lifetime of eight hours (Golub et al., 1974), and an average emission height of 8–12 Mm above the photosphere (Brajša et al., 2004; Tian et al., 2007). Also, XBPs show high temperature fluctuations (~ 2 MK) and intensity variability (Kariyappa et al., 2011, further, based on the intensity oscillations of XBPs and the resulting power spectra, Kariyappa & Varghese (2008) grouped XBPs into three classes depending on their emission levels). Our model predicts a flux too small to account for the energy losses at those height ranges. Turbulent wave heating may be necessary to heat the loops of XBPs.

Another important issue to scrutinize here is the lower boundary condition itself. Reliability of the extrapolations using the photospheric magnetic field has to be further reviewed. Abbett (2007) demonstrated that the quiet Sun model chromosphere is a non-force-free layer, and the extrapolations from the upper chromosphere may accurately yield the quiet Sun field. Further, our simulations do not capture the actual response of plasma to the dissipation, which is the determining factor when comparing the models with the emission maps of corona. A detailed MHD description is necessary to evaluate the role of the magnetic carpet in the heating of solar atmosphere. To conclude, our results show that the energy flux associated with quasi-static processes (here modeled using magneto-friction and hyperdiffusion) are not sufficient to heat the quiet solar corona. Although this suggests that the evolution of the magnetic carpet (through magnetic splitting, merging, cancellation, and emergence) without invoking any wave phenomena, does not play a dominant role in the coronal energy supply, a final judgment can be passed only with better observational constraints of magnetic field, in particular, at the force-free upper chromospheric layer. Observations from the next generation instruments such as the Advanced Technology Solar Telescope (ATST), and the Solar-C, which can offer multi-wavelength coverage with excellent spectro-polarimetric sensitivity, and large FOVs, will shed light on these issues.

Chapter 6

CONCLUSIONS AND FUTURE WORK

With an aim to understand the nature of magnetized solar atmosphere from the photosphere to corona, I studied various topics on the magnetic-field–plasma interactions at high spatial resolution. In this observationally motivated thesis, I used state-of-the-art observations from *Hinode*/SOT (BFI, and SP), *SDO*/HMI and AIA, *SoHO*/MDI, SST, and *Sunrise*/IMaX. I focused on the magnetic fields of arcsec and subarcsec scales, particularly in the quiet Sun. These magnetic elements manifest themselves as dark pores and bright points in the intensity images (for e.g. in G-band observations). The magnetic flux in these elements is typically in the range of 10^{16}–10^{20} Mx (a part of which has magnetic field strength in excess of a kilo Gauss). The quiet Sun magnetic field is also rich in the temporal scales. Intermittent internetwork magnetic field has a lifetime of a few minutes, while the ephemeral regions and network fields tend to evolve over several hours. Magnetic flux emergence in the quiet Sun is three orders of magnitude more than the emergence in active regions (Stein, 2012). These properties make the quiet Sun magnetic field very interesting to study. Also, the advancements in the observations made a detailed investigation possible.

Solar magnetic field is rooted in the photosphere and extends into the atmosphere giving rise to myriad of well known chromospheric and coronal structures (for e.g. bright chromospheric network, bright points, coronal loops, etc). Magnetic flux tubes are buffeted by the evolving granules. This results in a complicated and intricate coupling of the solar atmosphere. To better understand this coupling, it is important to dissect the layers of the atmosphere. For example, in the photosphere, convective motions and magnetic elements are influenced by each other. In the higher layers, plasma responds to the evolution of magnetic elements. For an extensive understanding of the nature and role of the quiet Sun magnetic field in the solar atmosphere, the above two aspects have been explored in four separate works, grouped in two parts.

In Section 6.1, I summarize the main results of this thesis work. In Section 6.2, I briefly describe the problems to be pursued in the future to conceive a holistic picture of the solar magnetic field and its broader impacts in the heliosphere.

6.1 SUMMARY

Dynamics in the Photosphere

- The effect of the magnetic field on photospheric intensity and velocity oscillations at the sites of SMFs in a quiet Sun near the solar disk center is studied. Observations made by the G-band filter in the *Hinode*/SOT for intensity oscillations; Doppler velocity, magnetic field, and continuum intensity are derived from an Ni I photospheric absorption line at 6767.8 Å using the *SoHO*/MDI are used. The analysis shows that both the high-resolution intensity observed in the G-band and velocity oscillations are influenced by the presence of a magnetic field. While intensity oscillations are suppressed at all frequencies in strong magnetic field regions compared to the regions of weak magnetic field, velocity oscillations show an enhancement of power in the frequency band 5.5–7 mHz. It is found that there is a drop of 20%–30% in the p-mode power of velocity oscillations within the SMFs when compared to the regions surrounding them. Our findings indicate that the nature of the interaction of acoustic waves with the quiet Sun SMFs is similar to that of large-scale magnetic fields in active regions. The first results of the center-to-limb variation of such effects using the observations of the quiet Sun from the *SDO*/HMI are reported. The independent verification of these interactions using SDO/HMI suggests that the velocity power drop of 20%–30% in p-modes is fairly constant across the solar disk.

- The sub-arcsec BPs associated with the small-scale magnetic fields in the lower solar atmosphere are advected by the evolution of the photospheric granules. Various quantities related to the horizontal motions of the BPs observed in two wavelengths, including the velocity auto-correlation function are measured in this study. A 1 hr time sequence of wideband Hα observations conducted at the SST, and a 4 hr *Hinode*/SOT *G*-band time sequence are used in this work. 97 *SST* and 212 *Hinode* BPs are followed with 3800 and 1950 individual velocity measurements respectively. For its high cadence of 5 s as compared to 30 s for *Hinode* data, the emphasize is more on the results from *SST* data. The BP positional uncertainty achieved by *SST* is as low as 3 km. The position errors contribute 0.75 km^2 s^{-2} to the variance of the observed velocities. The *raw* and *corrected* velocity measurements in both directions, i.e., (v_x, v_y), have Gaussian distributions

with standard deviations of $(1.32, 1.22)$ and $(1.00, 0.86)$ km s^{-1} respectively. The BP motions have correlation times of about 22–30 s. The power spectrum of the horizontal motions as a function of frequency, a quantity that is useful and relevant to the studies of generation of Alfvén waves is constructed. Additionally, photospheric turbulent diffusion at time scales less than 200 s is found to satisfy a power law with an index of 1.59.

Photosphere to Corona

- Data from the *SDO*/HMI and AIA are obtained to study coronal loops at small scales, emerging in the quiet Sun. With HMI LOS magnetograms, the integrated and unsigned photospheric magnetic flux at the loop footpoints in the photosphere are derived. These loops are bright in the EUV channels of AIA. Using the six AIA EUV filters, the differential emission measure (DEM) in the temperature range 5.7–6.5 in log T (K) for several hours of observations are constructed. The observed DEMs have a peak distribution around $\log T \approx 6.3$, falling rapidly at higher temperatures. For $\log T < 6.3$, DEMs are comparable to their peak values within an order of magnitude. The emission-weighted temperature is calculated, and its time variations are compared with those of magnetic flux. Two possibilities for explaining the observed DEMs and temperatures variations are presented. (1) Assuming that the observed loops are composed of a hundred thin strands with certain radius and length, three time-dependent heating models and compared the resulting DEMs and temperatures with the observed quantities are tested. This modeling used enthalpy-based thermal evolution of loops (EBTEL), a 0D hydrodynamic code. The comparisons suggest that a medium-frequency heating model with a population of different heating amplitudes can roughly reproduce the observations. (2) A loop model with steady heating and non-uniform cross-section of the loop along its length is also considered, and it is found that this model can also reproduce the observed DEMs, provided the loop expansion factor $\gamma \sim 5$–10. It is concluded that more observational constraints are required to better understand the nature of coronal heating in the short emerging loops on the quiet Sun.

- In the quiet solar photosphere, the mixed polarity fields form a magnetic carpet, which continuously evolves due to dynamical interaction between the convective motions and magnetic field. This interplay is a viable source to heat the solar atmosphere. In this work, the LOS magnetograms obtained from the *SDO*/HMI, and the *Sunrise*/IMaX are taken as time dependent lower boundary conditions, to study the evolution of the coronal magnetic field. A magneto-frictional relaxation method, including hyperdiffusion is used to produce time series of 3D

nonlinear force-free fields from a sequence of photospheric LOS magnetograms. Vertical flows are added up to a height of 0.7 Mm in the modeling to simulate the non-force-freeness at the photosphere-chromosphere layers. Among the derived quantities, the spatial and temporal variations of the energy dissipation rate, and energy flux are studied. The results show that the energy deposited in the solar atmosphere is concentrated within 2 Mm of the photosphere and there is not sufficient energy flux at the base of the corona to cover radiative and conductive losses. Possible reasons and implications are discussed. It is emphasized that better observational constraints of the magnetic field in the chromosphere are crucial to understand the role of the magnetic carpet in coronal heating.

This thesis work has provided further basis and warranted a need for the study of the quiet Sun magnetic field in detail, in particular the aspects of time evolution. The results imply that the rich, spatial and temporal dynamics of the small-scale magnetic field are important and they provide new and valuable insights into the physics of the solar atmosphere. Crucial constraints of the models for Alfvén and kink wave generation in solar magnetic flux tubes and quasi-static coronal heating processes are presented in this thesis. It has been shown that by combining observations and modeling we can realize the role played by fine-scale flux tubes in sustaining the solar atmosphere. Furthermore, the body of work brought into light some important issues that require attention, possibly with future observational developments. In the next Section, I outline some open questions in the field within the scope of this thesis work, and also some general questions to be solved to frame a bigger picture in the context of Sun-Earth connection.

6.2 FUTURE WORK

Since the launch of *Hinode* in the late 2006, there have been great advances in the field of small-scale magnetic fields on the Sun. The spacecraft allowed us to take a fresh look at the subarcsec kilo gauss fields and their dynamics. A confluence of superior space observatories and world-class ground based facilities are working together towards a common goal—a comprehensive view of the magnetic coupling of the solar atmosphere. Below are a few open questions that hold missing links to the puzzle i.e. the *solar atmospheric heating* that continued to remain as a mystery for several decades now.

- *The generation of small-scale field*. The origin of the intermittent and turbulent field on the Sun is not yet fully understood. Contradicting schools of thought prevail in the community. Some argue that the large-scale dynamo which is responsible for the structures such as the sunspots fuels the small-scale turbulent

field as well. Others claim that a surface dynamo operating locally generate the intermittent component of the field at subarcsec scales. Related to this problem is another issue viz. the geometry of the field. Is there a substantial horizontal field at the photosphere which is inaccessible to the current observational resolution and sensitivity? What is source of its origin and how it is connected to the well known radial kilo gauss field? To answer these questions, it is necessary to have extremely high spatial resolution spectropolarimetric observations with unprecedented signal-to-noise ratio. Future facilities such as the ATST and Solar-C can shed more light on these issues.

- *Chromospheric magnetic field*. The next important and fundamental question in the solar magnetism is related to the chromospheric magnetic field. As concluded in Chapter 5 the extrapolations of the photospheric field into the solar corona may not be accurate as we are missing the information from the non-force-free photosphere-chromosphere layers. Obtaining a vector field in these layers is non-trivial. Realistic 3D MHD models are required to be compared with the observations to get an estimation of the field above photosphere. Solving this problem is important as it further aids in modeling the coronal field (coronal loop expansion, local field strengths, etc).

- *Signatures in the solar wind*. "Canopy" like structures connecting network fields open into the extended corona and interact with the heliosphere. The solar wind (a nascent space weather driver) is believed to originate and accelerate close to the solar surface in the open field lines. As discussed in the Introduction of this thesis, space weather affects the Earth's magnetosphere. A frequent monitoring of the solar activity (at all spatial scales on the Sun) is needed to model the space weather and to identify instantaneous impacts on the Earth. Accurate boundary conditions in terms of the field strength, density, and temperature of the plasma are needed for a successful modeling of the Sun-Earth connection. It will be interesting to have an idea on the small-scale field as it can be a perturbation to the initial and boundary conditions. The imprints and signatures of the small-scale field in the space weather are yet to be discovered.

Appendices

Appendix A

DETERMINATION OF a AND b

In this section, we briefly describe a method of determining a and b for a set of parameters (Δ, τ, κ). We define the χ^2 of the autocorrelation functions of v_x and v_y as

$$\begin{aligned} \chi^2_{xx}(\Delta,\tau,\kappa) &= \sum_{n=-N}^{N} \left[c_{xx,n} - \mathfrak{C}_n(\Delta,\tau,\kappa)\right]^2, \text{and} \\ \chi^2_{yy}(\Delta,\tau,\kappa) &= \sum_{n=-N}^{N} \left[c_{yy,n} - \mathfrak{C}_n(\Delta,\tau,\kappa)\right]^2, \end{aligned} \tag{A.1}$$

where $c_{xx,n}$ and $c_{yy,n}$ are the observed autocorrelation values of velocities v_x and v_y, and $\mathfrak{C}$ is a model of the correlation function given by Equation (3.8). By minimizing the χ^2 with respect to a and b (i.e., $\frac{\partial \chi^2}{\partial a} = 0$ and $\frac{\partial \chi^2}{\partial b} = 0$, separately for x and y), and solving the resulting system of linear equations, we have

$$a = \frac{1}{\alpha\beta' - \alpha'\beta}\left(\beta' A - \beta B\right) \tag{A.2}$$

$$b = \frac{1}{\alpha\beta' - \alpha'\beta}\left(\alpha B - \alpha' A\right), \tag{A.3}$$

where

$$\begin{aligned} \alpha &= 2n+1 \\ \beta &= \sum_{n=-N}^{N} \frac{1}{1+\left(\frac{|t_n|}{\tau}\right)^{\kappa}} \\ \alpha' &= \beta \\ \beta' &= \sum_{n=-N}^{N} \frac{1}{\left[1+\left(\frac{|t_n|}{\tau}\right)^{\kappa}\right]^2} \\ A &= \sum_{n=-N}^{N} c_n \end{aligned}$$

$$B = \sum_{n=-N}^{N} \left(\frac{c_n - \Delta_n}{1 + \left(\frac{|t_n|}{\tau} \right)^{\kappa}} \right).$$

Appendix B

EBTEL AND LOOPS THAT EXPAND WITH TIME

The standard version of EBTEL assumes a symmetric loop with constant loop length and uniform cross-section. The model is based on the 1D time-dependent energy conservation equation:

$$\frac{\partial E}{\partial t} = -\frac{\partial}{\partial s} v(E+P) - \frac{\partial F_c}{\partial s} + Q - n^2 \Lambda(T), \tag{B.1}$$

where s is a spatial coordinate along the magnetic field; $E = \frac{3}{2}P + \frac{1}{2}\rho v^2$ is the total energy density; $n, T, P,$ and v are the electron number density, temperature, total pressure, and plasma bulk velocity, respectively; F_c is the heat flux; Q is volumetric heating rate; and $\Lambda(T)$ is the radiative loss function for optically thin plasma. It is assumed that both the velocity and heat flux vanish at the loop apex due to symmetry. Also, the flow velocity is subsonic, and gravity is neglected in the energy equation. Integrating the above equation over the coronal (L), and TR (l) lengths with the above assumption, we obtain

$$\frac{3}{2} L \frac{\partial \bar{P}}{\partial t} \approx \frac{5}{2} P_0 v_0 + F_0 + L\bar{Q} - \mathcal{R}_c, \tag{B.2}$$

$$\frac{3}{2} l \frac{\partial \bar{P}_{tr}}{\partial t} \approx -\frac{5}{2} P_0 v_0 - F_0 + l\bar{Q}_{tr} - \mathcal{R}_{tr}, \tag{B.3}$$

where overbar denotes the spatial averages of the quantities over respective sections of the loop, and subscript 0 denotes the values at the base of the corona; $\mathcal{R}_c,$ and $\mathcal{R}_{tr}$ are the coronal, and the TR radiative loss rates, respectively. Neglecting the terms involving

l (for a thin TR), and together with ideal gas law,[1] $\bar{P}$ and $\bar{n}$ can be approximated[2] with

$$\frac{d\bar{P}}{dt} \approx \frac{2}{3}\left[\bar{Q} - \frac{1}{L}(\mathcal{R}_c + \mathcal{R}_{tr})\right], \tag{B.4}$$

$$\frac{d\bar{n}}{dt} \approx -\frac{1}{5kLT_0}\left(F_0 + \mathcal{R}_{tr}\right). \tag{B.5}$$

For a given heating rate $\bar{Q}(t)$, the EBTEL model returns $\bar{P}, \bar{n}$, and $\bar{T}$ with other useful quantities.

For a uniformly expanding strand of length $L(t)$ and radius $R(t)$ adiabatically, the above equations are modified by adding a term $-\gamma\bar{P}\xi(t)$ on the right-hand side of Equation (B.4), and $-\bar{n}\xi(t)$ in Equation (B.5), where $\gamma = 5/3$ is the ratio of specific heats, and

$$\xi(t) = \frac{1}{L}\frac{dL}{dt} + \frac{2}{R}\frac{dR}{dt}. \tag{B.6}$$

The strand pressure, density, and temperature are modeled accordingly. The time-varying length and radius of a single strand are shown as thin solid and dashed curves, respectively, in Figure 4.5. Note that $R(t)$ explicitly enters the scheme only through Equation (B.6), and everywhere else, it is absorbed due to volumetric averaging.

[1] $P = 2nkT$ where k is the Boltzmann's constant.

[2] Simple volumetric averaging yields similar results.

Appendix C

MODEL FOR LOOPS THAT EXPAND WITH HEIGHT

In this section we describe a loop model for the case that the cross-sectional area A varies along the loop. For simplicity, the area $A(T)$ is considered to be a function of temperature:

$$A(T) = \exp\left\{\ln\gamma\left[\frac{z(T)}{z(T_{\max})} - 1\right]\right\}, \tag{C.1}$$

where $T_{\max}$ is the maximum temperature at loop top, and $z(T)$ is a monotonically increasing function, starting with $z \approx 0$ at the base of the TR. We use $z(T) = y + \sqrt{1+y^2}$ with $y = (x - x_0)/x_1$ and $x = \log_{10} T$. The constants x_0 and x_1 are set to 6.0 and 0.2, respectively, so that most of the area change occurs near a temperature of 1 MK. Similarly, the volumetric heating rate is

$$Q(T) = Q_{\max}\left(\frac{T}{T_{\max}}\right)^m, \tag{C.2}$$

where $Q_{\max}$ is the heating rate at the loop top, and m is an exponent (for the models presented here we set $m = 0$). The loop is assumed to be symmetric, and heating is assumed to be steady in time. We solve the following energy balance equation:

$$\frac{\partial}{\partial s}\left(AF_c\right) = A(T)\left[Q(T) - n^2\Lambda(T)\right], \tag{C.3}$$

where s is a spatial coordinate along the magnetic field, $F_c(s) \equiv -\kappa_0 T^{5/2}\partial T/\partial s$ is the conductive heat flux, $n(s)$ is the electron density, and $\Lambda(T)$ is the radiative loss function, which is taken from Klimchuk et al. (2008). Multiplying Equation (C.3) by AF_c and integrating over position along the loop, we obtain

$$\frac{1}{2}A^2F_c^2 = \kappa_0 Q_{\max}[fE_1(T) - E_2(T)], \tag{C.4}$$

where

$$E_1(T) = \int_{T_{\rm base}}^{T} A^2(T)\Lambda(T)T^{1/2}dT, \tag{C.5}$$

$$E_2(T) = \int_{T_{\rm base}}^{T} A^2(T)(T/T_{\rm max})^m T^{5/2}dT. \tag{C.6}$$

Here, $T_{\rm base}$ is the temperature at the base of the TR ($T_{\rm base} = 10^4$ K), and we assume $F_c = 0$ at the base. The factor f is given by

$$f \equiv \frac{P^2}{4k^2 Q_{\rm max}} = \frac{E_2(T_{\rm max})}{E_1(T_{\rm max})}, \tag{C.7}$$

where $P = 2nkT$ is the plasma pressure (a constant), and the last equality in (C.7) follows from the requirement that $F_c = 0$ at the loop top. Then the loop half-length L is given by

$$L = \int_{s_{\rm base}}^{s_{\rm max}} ds = \left(\frac{\kappa_0}{2Q_{\rm max}}\right)^{1/2} \int_{T_{\rm base}}^{T_{\rm max}} \frac{A(T)T^{5/2}dT}{\sqrt{fE_1(T) - E_2(T)}}. \tag{C.8}$$

For a given peak temperature $T_{\rm max}$ and half-length L, we can compute the heating rate $Q_{\rm max}$, pressure P, heat flux $F_c(T)$, and density $n(T)$. Then the DEM is given by $\varphi(T) = n^2(T)A(T)(\partial T/\partial s)^{-1}$. Since the area factor is normalized such that $A(T_{\rm max}) = 1$, this DEM(T) does not include the effects of a possible filling factor of the coronal loops.

Appendix D

DETAILS OF THE SOURCE MODEL

In this section we consider a model for the evolution of the photospheric magnetic field of the quiet Sun. The field is assumed to consists of a collection of discrete flux elements or "sources". Each source has an associated magnetic flux, which can be positive or negative, but the combined flux of all sources is assumed to vanish. Each source has a Gaussian flux distribution with radius $r_0 = 200$ km. The spatial distribution of the sources continually evolves due to several processes: (1) random motions driven by sub-surface convective flows, (2) splitting and merging of like-polarity sources, (3) mutual cancellation of opposite-polarity sources, and (4) emergence of new bipoles. To simulate these processes, we introduce a hexagonal grid with an edge length $L \approx 1$ Mm. Initially, the sources are centered at randomly selected vertices of the hexagonal grid (where 3 edges come together); subsequently they start moving along the edges of the grid. Each source has an equal probability (0.25) of moving along one of the three edges connecting to its original vertex, or remaining fixed at that vertex. The motion occurs with constant speed, $v = 1.5\ \mathrm{km\ s^{-1}}$, so that at time $t = \Delta t = L/v$ all moving sources again reach a neighboring vertex. Then the process repeats itself, producing a random walk of the sources along the grid edges. Therefore, in the present model all sources periodically return to the vertices (at times $t_n = n\Delta t$ with $n = 1, 2, \cdots$).

The magnetic sources interact with each other only at vertices of the hexagons. For example, when two sources meet at a vertex, they are forced to merge or partially cancel each other, depending on their magnetic polarity. Also, each source has a probability of splitting in two, which only occurs at a vertex so that the two parts may move away from each other along different edges. The emergence of a bipole is modeled by inserting a new pair of flux-balanced sources at a vertex and allowing the two sources to move apart along different edges of the grid. The newly inserted sources have absolute fluxes in the range 0.1–1.5×10^{18} Mx.

Figure D.1 illustrates various interactions between sources: (a) flux emergence, (b) emergence and subsequent partial cancellation, (c) splitting of an element, (d) total flux cancellation. Each panel has two segments. The top segment shows the time sequence

of the respective interaction (the numbers given in the snapshots indicate time, in minutes, elapsed since an arbitrary start time), and the bottom segment shows the magnetic flux vs. time. Flux merging, and self-cancellation of a newly emerged bipole are other possible ways in which the elements interact. We emphasize that the motivation behind the Source Model is not to create a realistic magnetic flux distribution for the quiet Sun, but rather to have a model with an average flux density similar to that obtained in the IMaX observations.

The simulation is initiated with 50 magnetic sources with magnetic fluxes in the range 5–50×10^{16} Mx. The top panel of Figure D.2 shows the integrated flux of the sources (i.e., the sum of absolute values of fluxes) as function of time. The initial phase of the model is dominated by flux emergence. After 15 hours into the evolution, the integrated flux reached a statistical equilibrium of 10^{20} Mx. This is due to the balance between the new flux emergence and partial/complete cancellation of the magnetic elements. The two thin vertical lines mark the period of evolution (8.5 hours) chosen for the main Source Model analysis presented in this work. In total, 2000 bipoles emerged in the complete time evolution of the model (360 during the 8.5 hour period). The average rate of flux emergence is about 150 $\mathrm{Mx\ cm^{-2}\ day^{-1}}$, which is a factor three less than the value reported by Thornton & Parnell (2011). However, their study included a much wider range of flux emergence events (10^{16}–10^{23}Mx). In the bottom panel, we show the mean magnetic field of the Source Model (solid line) as function of time in comparison with that of the IMaX dataset. The same quantities for the initial 0.5 hr period are plotted in the inset.

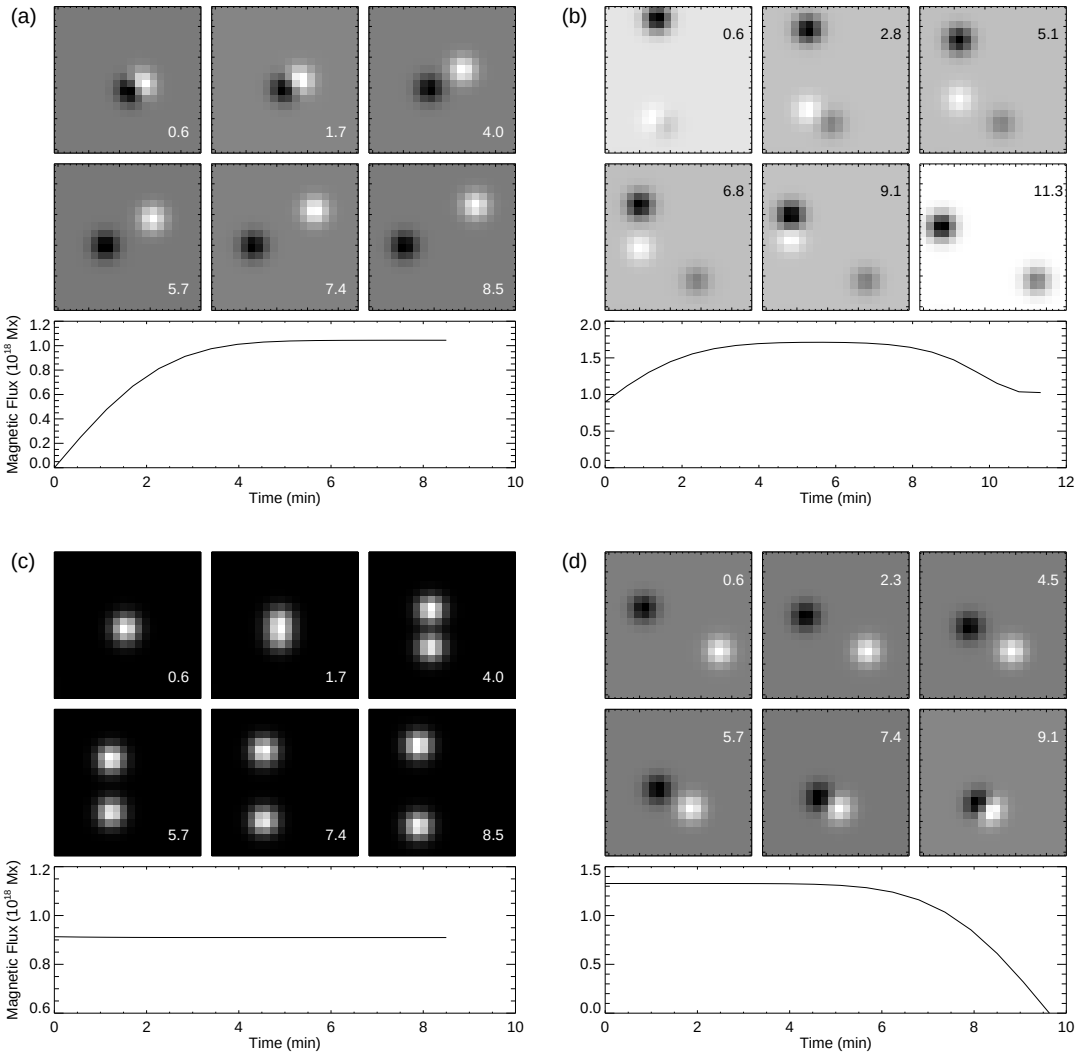

Figure D.1: Various interactions among magnetic elements in the Source Model are illustrated here. (a) Flux emergence. (b) Flux emergence followed by a partial flux cancellation. (c) Flux splitting. (d) Total flux cancellation. Each panel is comprised of two segments. The top segment is a time sequence of magnetic maps describing the interaction. Each map in the respective top segment covers an area of $\approx 2.4 \times 2.4$ Mm^2. The numbers in the maps indicate time, in minutes, elapsed since an arbitrary start time. The bottom segment is a plot of the magnetic flux integrated over the area of the map as a function of time. The scale of y-axis in the bottom segment is set at 10^{18} Mx.

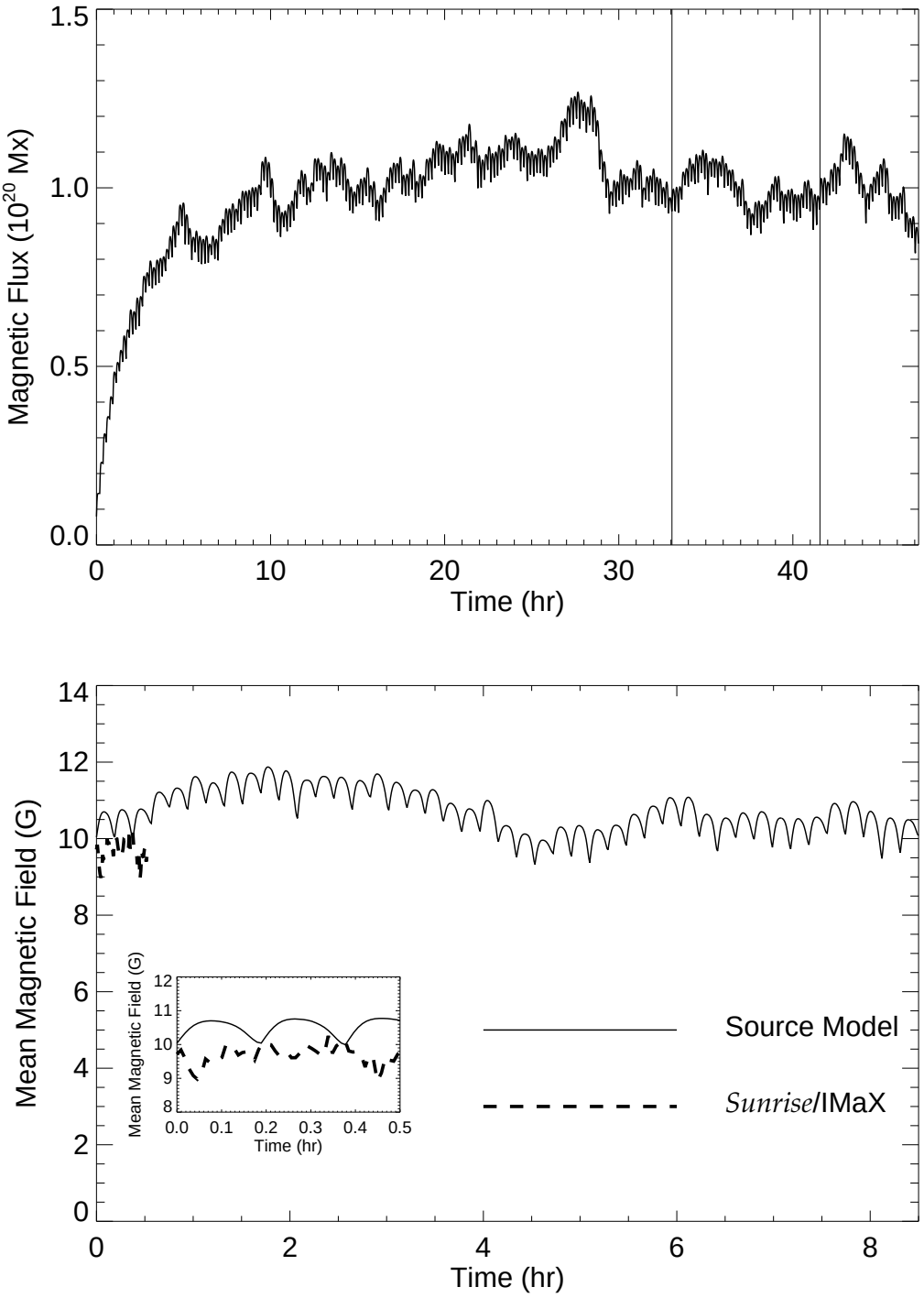

Figure D.2: Top: the complete time evolution of the magnetic flux for the Source Model, integrated over its FOV is shown. The plot includes both the rise and equilibrium phases of the magnetic flux as described in Section 5.2.1. Two thin vertical lines mark the period of 8.5 hours duration from which the time sequence of the Source Model is extracted for further analysis. Bottom: mean magnetic field of the Source Model (solid line; for the 8.5 hr period marked in the top panel) and IMaX (dashed line). The inset shows the same plot, but for the initial 0.5 hr period.

Bibliography

Abbett, W. P. 2007, ApJ, 665, 1469

Abramenko, V. I., Carbone, V., Yurchyshyn, V., Goode, P. R., Stein, R. F., Lepreti, F., Capparelli, V., & Vecchio, A. 2011, ApJ, 743, 133

Alfvén, H. 1947, MNRAS, 107, 211

Antiochos, S. K., & Klimchuk, J. A. 1991, ApJ, 378, 372

Antiochos, S. K., MacNeice, P. J., Spicer, D. S., & Klimchuk, J. A. 1999, ApJ, 512, 985

Asgari-Targhi, M., & van Ballegooijen, A. A. 2012, ApJ, 746, 81

Babcock, H. W. 1953, ApJ, 118, 387

Babcock, H. W., & Babcock, H. D. 1955a, ApJ, 121, 349

—. 1955b, Nature, 175, 296

Barthol, P., et al. 2011, Sol. Phys., 268, 1

Berger, T. E., Loefdahl, M. G., Shine, R. S., & Title, A. M. 1998, ApJ, 495, 973

Berger, T. E., Schrijver, C. J., Shine, R. A., Tarbell, T. D., Title, A. M., & Scharmer, G. 1995, ApJ, 454, 531

Berger, T. E., & Title, A. M. 1996, ApJ, 463, 365

—. 2001, ApJ, 553, 449

Bhattacharjee, A., & Hameiri, E. 1986, Physical Review Letters, 57, 206

Biermann, L. 1948, Z. Astrophys., 25, 161

Billings, D. E. 1966, A guide to the solar corona., New York: Academic Press, 1966. ISBN: 978-1-4832-3100-6

Bogdan, T. J., Hindman, B. W., Cally, P. S., & Charbonneau, P. 1996, ApJ, 465, 406

Boozer, A. H. 1986, Journal of Plasma Physics, 35, 133

Brajša, R., Wöhl, H., Vršnak, B., Ruždjak, V., Clette, F., Hochedez, J.-F., & Roša, D. 2004, A& A, 414, 707

Braun, D. C. 1995, ApJ, 451, 859

Braun, D. C., & Duvall, Jr., T. L. 1990, Sol. Phys., 129, 83

Braun, D. C., Duvall, Jr., T. L., & Labonte, B. J. 1987, ApJ Lett., 319, L27

Braun, D. C., Duvall, Jr., T. L., Labonte, B. J., Jefferies, S. M., Harvey, J. W., & Pomerantz, M. A. 1992a, ApJ Lett., 391, L113

Braun, D. C., Labonte, B. J., & Duvall, Jr., T. L. 1990, ApJ, 354, 372

Braun, D. C., Lindsey, C., Fan, Y., & Jefferies, S. M. 1992b, ApJ, 392, 739

Brown, T. M., Bogdan, T. J., Lites, B. W., & Thomas, J. H. 1992, ApJ Lett., 394, L65

Bumba, V., & Howard, R. 1965, ApJ, 141, 1502

Cadavid, A. C., Lawrence, J. K., & Ruzmaikin, A. A. 1999, ApJ, 521, 844

Cargill, P. J. 1994, ApJ, 422, 381

Cargill, P. J., Bradshaw, S. J., & Klimchuk, J. A. 2012, ApJ, 752, 161

Cargill, P. J., & Klimchuk, J. A. 1997, ApJ, 478, 799

Carrington, R. C. 1859, MNRAS, 20, 13

Centeno, R., et al. 2007, ApJ Lett., 666, L137

Chapman, G. A., & Sheeley, Jr., N. R. 1968, Sol. Phys., 5, 442

Charbonneau, P. 2010, Living Reviews in Solar Physics, 7

Chesny, D. L., Oluseyi, H. M., & Orange, N. B. 2013, ApJ Lett., 778, L17

Cheung, M. C. M., & DeRosa, M. L. 2012, ApJ, 757, 147

Chitta, L. P., Jain, R., Kariyappa, R., & Jefferies, S. M. 2012a, ApJ, 744, 98

Chitta, L. P., Kariyappa, R., van Ballegooijen, A. A., DeLuca, E. E., Hasan, S. S., & Hanslmeier, A. 2013, ApJ, 768, 32

Chitta, L. P., Kariyappa, R., van Ballegooijen, A. A., DeLuca, E. E., & Solanki, S. K. 2014, ApJ, 793, 112

Chitta, L. P., van Ballegooijen, A. A., Rouppe van der Voort, L., DeLuca, E. E., & Kariyappa, R. 2012b, ApJ, 752, 48

Choudhuri, A. R., Auffret, H., & Priest, E. R. 1993, Sol. Phys., 143, 49

Close, R. M., Parnell, C. E., Longcope, D. W., & Priest, E. R. 2004, ApJ Lett., 612, L81

Cowling, T. G. 1945, MNRAS, 105, 166

Cram, L. E., & Dame, L. 1983, ApJ, 272, 355

Cranmer, S. R., & van Ballegooijen, A. A. 2010, ApJ, 720, 824

Cranmer, S. R., van Ballegooijen, A. A., & Woolsey, L. N. 2013, ApJ, 767, 125

De Pontieu, B., Hansteen, V. H., Rouppe van der Voort, L., van Noort, M., & Carlsson, M. 2007a, ApJ, 655, 624

De Pontieu, B., et al. 2007b, Science, 318, 1574

de Wijn, A. G., Stenflo, J. O., Solanki, S. K., & Tsuneta, S. 2009, Space Sci. Rev., 144, 275

Del Zanna, G., O'Dwyer, B., & Mason, H. E. 2011, A& A, 535, A46

Doschek, G. A., Landi, E., Warren, H. P., & Harra, L. K. 2010, ApJ, 710, 1806

Edlén, B. 1942, Z. Astrophys., 22, 30

Elsasser, W. M. 1956, Reviews of Modern Physics, 28, 135

Fan, Y. 2009, Living Reviews in Solar Physics, 6

Frazier, E. N., & Stenflo, J. O. 1972, Sol. Phys., 27, 330

Freeland, S. L., & Handy, B. N. 1998, Sol. Phys., 182, 497

Galsgaard, K., & Parnell, C. E. 2005, A& A, 439, 335

Gizon, L., et al. 2009, Space Sci. Rev., 144, 249

Golub, L., Deluca, E. E., Sette, A., & Weber, M. 2004, in Astronomical Society of the Pacific Conference Series, Vol. 325, The Solar-B Mission and the Forefront of Solar Physics, ed. T. Sakurai & T. Sekii, 217

Golub, L., Krieger, A. S., Silk, J. K., Timothy, A. F., & Vaiana, G. S. 1974, ApJ Lett., 189, L93

Gordovskyy, M., Jain, R., & Hindman, B. W. 2009, ApJ, 694, 1602

Grotian, W. 1939, Naturwiss., 27, 214

Gudiksen, B. V., & Nordlund, Å. 2002, ApJ Lett., 572, L113

Habbal, S. R., & Grace, E. 1991, ApJ, 382, 667

Hale, G. E. 1908, ApJ, 28, 315

—. 1913, ApJ, 38, 27

Hale, G. E., Ellerman, F., Nicholson, S. B., & Joy, A. H. 1919, ApJ, 49, 153

Hale, G. E., & Nicholson, S. B. 1925, ApJ, 62, 270

Hanasoge, S. M. 2009, A& A, 503, 595

Hasan, S. S., & Kalkofen, W. 1999, ApJ, 519, 899

Hasan, S. S., & van Ballegooijen, A. A. 2008, ApJ, 680, 1542

Hasan, S. S., van Ballegooijen, A. A., Kalkofen, W., & Steiner, O. 2005, ApJ, 631, 1270

Hindman, B. W., & Brown, T. M. 1998, ApJ, 504, 1029

Hindman, B. W., & Jain, R. 2008, ApJ, 677, 769

Hood, A. W., & Priest, E. R. 1980, A& A, 87, 126

Iida, Y., Hagenaar, H. J., & Yokoyama, T. 2012, ApJ, 752, 149

Jafarzadeh, S., Solanki, S. K., Feller, A., Lagg, A., Pietarila, A., Danilovic, S., Riethmüller, T. L., & Martínez Pillet, V. 2013, A& A, 549, A116

Jain, R., & Haber, D. 2002, A& A, 387, 1092

Jain, R., Hindman, B. W., Braun, D. C., & Birch, A. C. 2009, ApJ, 695, 325

Jain, R., Hindman, B. W., & Zweibel, E. G. 1996, ApJ, 464, 476

Jess, D. B., Mathioudakis, M., Erdélyi, R., Crockett, P. J., Keenan, F. P., & Christian, D. J. 2009, Science, 323, 1582

Kalkofen, W. 1989, ApJ Lett., 346, L37

Kariyappa, R. 1994, Sol. Phys., 154, 19

Kariyappa, R., Deluca, E. E., Saar, S. H., Golub, L., Damé, L., Pevtsov, A. A., & Varghese, B. A. 2011, A& A, 526, A78

Kariyappa, R., & Pap, J. M. 1996, Sol. Phys., 167, 115

Kariyappa, R., & Sivaraman, K. R. 1994, Sol. Phys., 152, 139

Kariyappa, R., Sivaraman, K. R., & Anadaram, M. N. 1994, Sol. Phys., 151, 243

Kariyappa, R., & Varghese, B. A. 2008, A& A, 485, 289

Khomenko, E., & Collados, M. 2009, A& A, 506, L5

Kitiashvili, I. N., Kosovichev, A. G., Mansour, N. N., & Wray, A. A. 2011, Sol. Phys., 268, 283

Klimchuk, J. A. 2006, Sol. Phys., 234, 41

Klimchuk, J. A., Karpen, J. T., & Antiochos, S. K. 2010, ApJ, 714, 1239

Klimchuk, J. A., Patsourakos, S., & Cargill, P. J. 2008, ApJ, 682, 1351

Kosugi, T., et al. 2007, Sol. Phys., 243, 3

Lagg, A., et al. 2010, ApJ Lett., 723, L164

Lamb, D. A., Howard, T. A., DeForest, C. E., Parnell, C. E., & Welsch, B. T. 2013, ApJ, 774, 127

Leighton, R. B. 1959, ApJ, 130, 366

Leighton, R. B., Noyes, R. W., & Simon, G. W. 1962, ApJ, 135, 474

Lemen, J. R., et al. 2012, Sol. Phys., 275, 17

Lites, B. W., White, O. R., & Packman, D. 1982, ApJ, 253, 386

Longcope, D. W., & Kankelborg, C. C. 1999, ApJ, 524, 483

Mackay, D. H., Green, L. M., & van Ballegooijen, A. 2011, ApJ, 729, 97

Manso Sainz, R., Martínez González, M. J., & Asensio Ramos, A. 2011, A& A, 531, L9

Markwardt, C. B. 2009, in Astronomical Society of the Pacific Conference Series, Vol. 411, Astronomical Data Analysis Software and Systems XVIII, ed. D. A. Bohlender, D. Durand, & P. Dowler, 251

Martínez Pillet, V., et al. 2011, Sol. Phys., 268, 57

Maunder, E. W. 1922, MNRAS, 82, 534

McIntosh, S. W., de Pontieu, B., Carlsson, M., Hansteen, V., Boerner, P., & Goossens, M. 2011, Nature, 475, 477

Metcalf, T. R., Jiao, L., McClymont, A. N., Canfield, R. C., & Uitenbroek, H. 1995, ApJ, 439, 474

Metcalf, T. R., et al. 2008, Sol. Phys., 247, 269

Meyer, K. A., Sabol, J., Mackay, D. H., & van Ballegooijen, A. A. 2013, ApJ Lett., 770, L18

Müller, D. A. N., Hansteen, V. H., & Peter, H. 2003, A& A, 411, 605

Müller, D. A. N., Peter, H., & Hansteen, V. H. 2004, A& A, 424, 289

Muller, R. 1983, Sol. Phys., 85, 113

—. 1985, Sol. Phys., 100, 237

Muller, R., & Keil, S. L. 1983, Sol. Phys., 87, 243

Muller, R., Roudier, T., Vigneau, J., & Auffret, H. 1994, A& A, 283, 232

Nakariakov, V. M., & Verwichte, E. 2005, Living Reviews in Solar Physics, 2, 3

Narain, U., & Ulmschneider, P. 1996, Space Sci. Rev., 75, 453

Nisenson, P., van Ballegooijen, A. A., de Wijn, A. G., & Sütterlin, P. 2003, ApJ, 587, 458

O'Dwyer, B., Del Zanna, G., Mason, H. E., Weber, M. A., & Tripathi, D. 2010, A& A, 521, A21

Orozco Suárez, D., Katsukawa, Y., & Bellot Rubio, L. R. 2012, ApJ Lett., 758, L38

Parker, E. N. 1955a, ApJ, 122, 293

—. 1955b, ApJ, 121, 491

—. 1988, ApJ, 330, 474

Pérez-Suárez, D., Maclean, R. C., Doyle, J. G., & Madjarska, M. S. 2008, A& A, 492, 575

Pesnell, W. D., Thompson, B. J., & Chamberlin, P. C. 2012, Sol. Phys., 275, 3

Peter, H., Bingert, S., & Kamio, S. 2012, A& A, 537, A152

Priest, E. R., Heyvaerts, J. F., & Title, A. M. 2002, ApJ, 576, 533

Reale, F. 2010, Living Reviews in Solar Physics, 7, 5

Reidy, W. P., Vaiana, G. S., Zehnpfennig, T., & Giacconi, R. 1968, ApJ, 151, 333

Rosner, R., Tucker, W. H., & Vaiana, G. S. 1978, ApJ, 220, 643

Scharmer, G. B., Bjelksjo, K., Korhonen, T. K., Lindberg, B., & Petterson, B. 2003a, in Society of Photo-Optical Instrumentation Engineers (SPIE) Conference Series, Vol. 4853, Society of Photo-Optical Instrumentation Engineers (SPIE) Conference Series, ed. S. L. Keil & S. V. Avakyan, 341–350

Scharmer, G. B., Dettori, P. M., Lofdahl, M. G., & Shand, M. 2003b, in Society of Photo-Optical Instrumentation Engineers (SPIE) Conference Series, Vol. 4853, Society of Photo-Optical Instrumentation Engineers (SPIE) Conference Series, ed. S. L. Keil & S. V. Avakyan, 370–380

Scherrer, P. H., et al. 1995, Sol. Phys., 162, 129

—. 2012, Sol. Phys., 275, 207

Schmelz, J. T., & Pathak, S. 2012, ApJ, 756, 126

Schou, J., et al. 2012, Sol. Phys., 275, 229

Schrijver, C. J., Title, A. M., van Ballegooijen, A. A., Hagenaar, H. J., & Shine, R. A. 1997, ApJ, 487, 424

Schrijver, C. J., & van Ballegooijen, A. A. 2005, ApJ, 630, 552

Schrijver, C. J., et al. 1998, Nature, 394, 152

—. 2006, Sol. Phys., 235, 161

Schunker, H., & Braun, D. C. 2011, Sol. Phys., 268, 349

Schwabe, H. 1844, Astron. Nachr., 21, 233

Schwarzschild, M. 1948, ApJ, 107, 1

Sheeley, Jr., N. R. 1966, ApJ, 144, 723

—. 1967, Sol. Phys., 1, 171

Sivaraman, K. R., & Livingston, W. C. 1982, Sol. Phys., 80, 227

Solanki, S. K. 1993, Space Sci. Rev., 63, 1

Solanki, S. K., et al. 2010, ApJ Lett., 723, L127

Spadaro, D., Lanza, A. F., Lanzafame, A. C., Karpen, J. T., Antiochos, S. K., Klimchuk, J. A., & MacNeice, P. J. 2003, ApJ, 582, 486

Spruit, H. C. 1981, A& A, 98, 155

Spruit, H. C. 1984, in Small-Scale Dynamical Processes in Quiet Stellar Atmospheres, ed. S. L. Keil, 249–+

Stein, R. F. 2012, Living Reviews in Solar Physics, 9

Stenflo, J. O. 1973, Sol. Phys., 32, 41

Stenflo, J. O., & Harvey, J. W. 1985, Sol. Phys., 95, 99

Stix, M. 2004, The sun : an introduction, 2nd ed., Astronomy and Astrophysics Library, Berlin: Springer, 2004. ISBN: 3540207414

Strauss, H. R. 1988, ApJ, 326, 412

Suematsu, Y., et al. 2008, Sol. Phys., 249, 197

Thomas, J. H., & Stanchfield, II, D. C. H. 2000, ApJ, 537, 1086

Thornton, L. M., & Parnell, C. E. 2011, Sol. Phys., 269, 13

Tian, H., Tu, C.-Y., He, J.-S., & Marsch, E. 2007, Advances in Space Research, 39, 1853

Title, A. M., & Rosenberg, W. J. 1981, Optical Engineering, 20, 815

Title, A. M., Tarbell, T. D., & Topka, K. P. 1987, ApJ, 317, 892

Tripathi, D., Mason, H. E., & Klimchuk, J. A. 2010, ApJ, 723, 713

Tripathy, S., Jain, K., Hill, F., Gonzalez-Hernandez, I., Armstrong, J. D., Jefferies, S. M., Rhodes, Jr., E. J., & Rose, P. J. 2007, in Bulletin of the American Astronomical Society, Vol. 38, Bulletin of the American Astronomical Society, 130–+

Tsuneta, S., et al. 2008, Sol. Phys., 249, 167

Ugarte-Urra, I., Doyle, J. G., & Del Zanna, G. 2005, A& A, 435, 1169

Ugarte-Urra, I., & Warren, H. P. 2012, ApJ, 761, 21

Ugarte-Urra, I., Warren, H. P., & Brooks, D. H. 2009, ApJ, 695, 642

Utz, D., Hanslmeier, A., Muller, R., Veronig, A., Rybák, J., & Muthsam, H. 2010, A& A, 511, A39

Vaiana, G. S., Krieger, A. S., & Timothy, A. F. 1973, Sol. Phys., 32, 81

van Ballegooijen, A. A. 1986, ApJ, 311, 1001

van Ballegooijen, A. A., Asgari-Targhi, M., Cranmer, S. R., & DeLuca, E. E. 2011, ApJ, 736, 3

van Ballegooijen, A. A., & Cranmer, S. R. 2008, ApJ, 682, 644

van Ballegooijen, A. A., Nisenson, P., Noyes, R. W., Löfdahl, M. G., Stein, R. F., Nordlund, Å., & Krishnakumar, V. 1998, ApJ, 509, 435

van Noort, M., Rouppe van der Voort, L., & Löfdahl, M. G. 2005, Sol. Phys., 228, 191

van Noort, M. J., & Rouppe van der Voort, L. H. M. 2006, ApJ Lett., 648, L67

Viall, N. M., & Klimchuk, J. A. 2012, ApJ, 753, 35

Warren, H. P., Winebarger, A. R., & Brooks, D. H. 2010, ApJ, 711, 228

Weber, M. A., Deluca, E. E., Golub, L., & Sette, A. L. 2004, in IAU Symposium, Vol. 223, Multi-Wavelength Investigations of Solar Activity, ed. A. V. Stepanov, E. E. Benevolenskaya, & A. G. Kosovichev, 321–328

Wedemeyer-Böhm, S., Lagg, A., & Nordlund, Å. 2009, Space Sci. Rev., 144, 317

Wedemeyer-Böhm, S., & Rouppe van der Voort, L. 2009, A& A, 507, L9

Wiegelmann, T., & Sakurai, T. 2012, Living Reviews in Solar Physics, 9, 5

Wiegelmann, T., et al. 2010, ApJ Lett., 723, L185

—. 2013, Sol. Phys., 283, 253

Winebarger, A. R., Schmelz, J. T., Warren, H. P., Saar, S. H., & Kashyap, V. L. 2011, ApJ, 740, 2

Withbroe, G. L. 1988, ApJ, 325, 442

Withbroe, G. L., & Noyes, R. W. 1977, ARA& A, 15, 363

Woods, D. T., & Cram, L. E. 1981, Sol. Phys., 69, 233

Yang, S., Zhang, J., Li, T., & Liu, Y. 2012, ApJ Lett., 752, L24

Yang, W. H., Sturrock, P. A., & Antiochos, S. K. 1986, ApJ, 309, 383

Zirker, J. B. 1993, Sol. Phys., 148, 43